Atmos. Chem. Phys., 18, 10289–10331, 2018
https://doi.org/10.5194/acp-18-10289-2018

Atmospheric Chemistry and Physics
Open Access
EGU

Long-term observations of cloud condensation nuclei over the Amazon rain forest – Part 2: Variability and characteristics of biomass burning, long-range transport, and pristine rain forest aerosols

Mira L. Pöhlker[1], Florian Ditas[1], Jorge Saturno[1,a], Thomas Klimach[1], Isabella Hrabě de Angelis[1], Alessandro C. Araùjo[2], Joel Brito[3,b], Samara Carbone[3,c], Yafang Cheng[1], Xuguang Chi[1,d], Reiner Ditz[1], Sachin S. Gunthe[4], Bruna A. Holanda[1], Konrad Kandler[5], Jürgen Kesselmeier[1], Tobias Könemann[1], Ovid O. Krüger[1], Jošt V. Lavrič[6], Scot T. Martin[7,8], Eugene Mikhailov[9], Daniel Moran-Zuloaga[1], Luciana V. Rizzo[10], Diana Rose[11,e], Hang Su[1], Ryan Thalman[12,f], David Walter[1], Jian Wang[12], Stefan Wolff[1], Henrique M. J. Barbosa[3], Paulo Artaxo[2], Meinrat O. Andreae[1,13], Ulrich Pöschl[1], and Christopher Pöhlker[1]

[1]Multiphase Chemistry and Biogeochemistry Departments, Max Planck Institute for Chemistry, 55020 Mainz, Germany
[2]Empresa Brasileira de Pesquisa Agropecuária (EMBRAPA), Trav. Dr. Enéas Pinheiro, Belém, PA, 66095-100, Brazil
[3]Institute of Physics, University of São Paulo, São Paulo 05508-900, Brazil
[4]EWRE Division, Department of Civil Engineering, Indian Institute of Technology Madras, Chennai 600036, India
[5]Institut für Angewandte Geowissenschaften, Technische Universität Darmstadt, Darmstadt, Germany
[6]Department of Biogeochemical Systems, Max Planck Institute for Biogeochemistry, 07701 Jena, Germany
[7]John A. Paulson School of Engineering and Applied Sciences, Harvard University, Cambridge, MA, USA
[8]Department of Earth and Planetary Sciences, Harvard University, Cambridge, MA, USA
[9]St. Petersburg State University, 7/9 Universitetskaya nab, St. Petersburg, 199034, Russia
[10]Instituto de Ciências Ambientais, Químicas e Farmacêuticas, Universidade Federal de São Paulo (UNIFESP), Diadema, SP, Brazil
[11]Institut für Atmosphäre und Umwelt, Goethe Universität, 60438 Frankfurt, Germany
[12]Biological, Environmental & Climate Sciences Department, Brookhaven National Laboratory, Upton, NY 11973-5000, USA
[13]Scripps Institution of Oceanography, University of California San Diego, La Jolla, CA 92037, USA
[a]now at: Physikalisch-Technische Bundesanstalt, Bundesallee 100, 38116 Braunschweig, Germany
[b]now at: Laboratoire de Météorologie Physique, Université Clermont Auvergne, Aubière, France
[c]now at: Institute of Agrarian Sciences, Federal University of Uberlândia, Uberlândia, Minas Gerais, Brazil
[d]now at: Institute for Climate and Global Change Research & School of Atmospheric Sciences, Nanjing University, Nanjing, 210093, China
[e]now at: Hessian Agency for Nature Conservation, Environment and Geology, Rheingaustr. 186, 65203 Wiesbaden, Germany
[f]now at: Department of Chemistry, Snow College, Richfield, UT, USA

Correspondence: Mira L. Pöhlker (m.pohlker@mpic.de) and Christopher Pöhlker (c.pohlker@mpic.de)

Received: 10 September 2017 – Discussion started: 10 October 2017
Revised: 8 May 2018 – Accepted: 17 May 2018 – Published: 19 July 2018

Published by Copernicus Publications on behalf of the European Geosciences Union.

Abstract. Size-resolved measurements of atmospheric aerosol and cloud condensation nuclei (CCN) concentrations and hygroscopicity were conducted over a full seasonal cycle at the remote Amazon Tall Tower Observatory (ATTO, March 2014–February 2015). In a preceding companion paper, we presented annually and seasonally averaged data and parametrizations (Part 1; Pöhlker et al., 2016a). In the present study (Part 2), we analyze key features and implications of aerosol and CCN properties for the following characteristic atmospheric conditions:

- Empirically pristine rain forest (PR) conditions, where no influence of pollution was detectable, as observed during parts of the wet season from March to May. The PR episodes are characterized by a bimodal aerosol size distribution (strong Aitken mode with $D_{\mathrm{Ait}} \approx 70\,\mathrm{nm}$ and $N_{\mathrm{Ait}} \approx 160\,\mathrm{cm}^{-3}$, weak accumulation mode with $D_{\mathrm{acc}} \approx 160\,\mathrm{nm}$ and $N_{\mathrm{acc}} \approx 90\,\mathrm{cm}^{-3}$), a chemical composition dominated by organic compounds, and relatively low particle hygroscopicity ($\kappa_{\mathrm{Ait}} \approx 0.12$, $\kappa_{\mathrm{acc}} \approx 0.18$).

- Long-range-transport (LRT) events, which frequently bring Saharan dust, African biomass smoke, and sea spray aerosols into the Amazon Basin, mostly during February to April. The LRT episodes are characterized by a dominant accumulation mode ($D_{\mathrm{Ait}} \approx 80\,\mathrm{nm}$, $N_{\mathrm{Ait}} \approx 120\,\mathrm{cm}^{-3}$ vs. $D_{\mathrm{acc}} \approx 180\,\mathrm{nm}$, $N_{\mathrm{acc}} \approx 310\,\mathrm{cm}^{-3}$), an increased abundance of dust and salt, and relatively high hygroscopicity ($\kappa_{\mathrm{Ait}} \approx 0.18$, $\kappa_{\mathrm{acc}} \approx 0.35$). The coarse mode is also significantly enhanced during these events.

- Biomass burning (BB) conditions characteristic for the Amazonian dry season from August to November. The BB episodes show a very strong accumulation mode ($D_{\mathrm{Ait}} \approx 70\,\mathrm{nm}$, $N_{\mathrm{Ait}} \approx 140\,\mathrm{cm}^{-3}$ vs. $D_{\mathrm{acc}} \approx 170\,\mathrm{nm}$, $N_{\mathrm{acc}} \approx 3400\,\mathrm{cm}^{-3}$), very high organic mass fractions ($\sim 90\,\%$), and correspondingly low hygroscopicity ($\kappa_{\mathrm{Ait}} \approx 0.14$, $\kappa_{\mathrm{acc}} \approx 0.17$).

- Mixed-pollution (MPOL) conditions with a superposition of African and Amazonian aerosol emissions during the dry season. During the MPOL episode presented here as a case study, we observed African aerosols with a broad monomodal distribution ($D \approx 130\,\mathrm{nm}$, $N_{\mathrm{CN},10} \approx 1300\,\mathrm{cm}^{-3}$), with high sulfate mass fractions ($\sim 20\,\%$) from volcanic sources and correspondingly high hygroscopicity ($\kappa_{<100\,\mathrm{nm}} \approx 0.14$, $\kappa_{>100\,\mathrm{nm}} \approx 0.22$), which were periodically mixed with fresh smoke from nearby fires ($D \approx 110\,\mathrm{nm}$, $N_{\mathrm{CN},10} \approx 2800\,\mathrm{cm}^{-3}$) with an organic-dominated composition and sharply decreased hygroscopicity ($\kappa_{<150\,\mathrm{nm}} \approx 0.10$, $\kappa_{>150\,\mathrm{nm}} \approx 0.20$).

Insights into the aerosol mixing state are provided by particle hygroscopicity (κ) distribution plots, which indicate largely internal mixing for the PR aerosols (narrow κ distribution) and more external mixing for the BB, LRT, and MPOL aerosols (broad κ distributions).

The CCN spectra (CCN concentration plotted against water vapor supersaturation) obtained for the different case studies indicate distinctly different regimes of cloud formation and microphysics depending on aerosol properties and meteorological conditions. The measurement results suggest that CCN activation and droplet formation in convective clouds are mostly aerosol-limited under PR and LRT conditions and updraft-limited under BB and MPOL conditions. Normalized CCN efficiency spectra (CCN divided by aerosol number concentration plotted against water vapor supersaturation) and corresponding parameterizations (Gaussian error function fits) provide a basis for further analysis and model studies of aerosol–cloud interactions in the Amazon.

1 Introduction

Clouds are a key factor in the Earth's atmosphere and climate system (Bony et al., 2015). Thus, sound scientific knowledge on the life cycle and highly dynamic properties of clouds is of significant importance for our understanding of atmospheric cycling and climate change (Seinfeld et al., 2016). A number of recent overview studies summarize the various facets of aerosol–cloud–precipitation–climate interactions in a detailed and comprehensive way (e.g., Andreae and Rosenfeld, 2008; Tao et al., 2012; Rosenfeld et al., 2014).

The Amazon Basin and its unique rain forest ecosystem are fundamentally shaped by the intense and large-scale (re)circulation of water between biosphere and atmosphere. Accordingly, the life cycle of shallow and deep convective clouds in the Amazon has been subject of numerous previous studies (e.g., Andreae et al., 2004; Freud et al., 2008; Rosenfeld et al., 2016; Wendisch et al., 2016; Braga et al., 2017). In particular, the extent of anthropogenic influence on the cloud life cycle through continuous land use change and combustion-related aerosol emissions has been actively debated (e.g., Roberts et al., 2003; Davidson et al., 2012; Goncalves et al., 2015). It is well established that the properties and dynamics of clouds can be fundamentally altered by changing cloud condensation nuclei (CCN) regimes, which are a fraction of the total (tropospheric) aerosol population (e.g., Rosenfeld et al., 2008; Reutter et al., 2009).

To explore essential biogeochemical processes, such as aerosol–cloud interactions, in the Amazon rain forest, the Amazon Tall Tower Observatory (ATTO) was established in 2010/11 (for details see Andreae et al., 2015). The central Amazon Basin is characterized by a pronounced seasonality in atmospheric composition in response to the north–south oscillation of the Intertropical Convergence Zone (ITCZ). During the wet season, the ATTO site receives comparatively clear air masses of marine origin from the northeast

that travel over mostly untouched rain forest areas, whereas during the dry season strongly polluted air masses are advected from the southeast, originating from numerous fires in the Amazon's arc of deforestation (for details see C. Pöhlker et al., 2018). Detailed information on characteristic differences in the atmospheric state and processes for the contrasting wet- vs. dry-season conditions in the ATTO region can be found in a number of recent studies (e.g., Nölscher et al., 2016; Pöhlker et al., 2016; Moran-Zuloaga et al., 2017; Saturno et al., 2017a; Yañez-Serrano et al., 2018).

In terms of microphysical processes in cloud formation and development, the number concentration of CCN, $N_{CCN}(S)$, and the peak water vapor supersaturation, S, at the cloud base play a key role. Here, S is predominantly determined by the updraft velocity, w_b, of the adiabatically rising air parcel at the cloud base. The relevant peak S levels in the Amazon are assumed to range from ~ 0.1 to $\sim 1.0\,\%$ (e.g., Andreae, 2009; Reutter et al., 2009; Pöschl et al., 2010; Pöhlker et al., 2012; Farmer et al., 2015; Pöhlker et al., 2016). Moreover, a recent study suggests that substantially higher S ($\gg 1\,\%$) can also be reached in deep convective clouds under certain conditions (Fan et al., 2018). However, a systematic and quantitative assessment of relevant peak S distributions in the Amazonian atmosphere is still lacking (see discussion in Sect. 3.9). Depending on $N_{CCN}(S)$ and S, a certain number of cloud droplets at the cloud base, N_{db}, are formed (Rosenfeld et al., 2016). In the Amazon Basin, N_{db} ranges from a few hundred droplets per cubic centimeter for clean conditions to 1000 and 2000 cm^{-3} for polluted conditions (Pöschl et al., 2010; Rosenfeld et al., 2016; Braga et al., 2017). Upon cloud development and rising air masses, the initial droplets grow by condensation of water vapor, which can be observed as changes in the cloud drop size distribution (DSD). Thus, the DSD is a function of thermodynamic parameters (i.e., the updraft velocity, w_b), aerosol conditions (i.e., $N_{CCN}(S)$), and the cloud evolution (i.e., the cloud depth, H). Important bulk DSD properties are, in particular, the droplet number concentration, N_d, and the effective droplet radius, r_e. For $r_e > 11\,\mu m$, the probability of droplet collision and coalescence processes increases to significant levels, and warm rain formation is initiated (Cecchini et al., 2017a).

A detailed analysis of the properties and variability of the Amazonian CCN population is a prerequisite for the understanding of cloud cycling in this region. However, the CCN data from the basin is still sparse. Therefore, we conducted a systematic characterization of the trends and properties of the central Amazonian CCN population at the ATTO site. The first half of this study has been published recently as Part 1 (Pöhlker et al., 2016). The present paper represents Part 2 and focuses on the variability and properties of periods and conditions that are characteristic for the Amazonian atmosphere.

1.1 Brief summary of the Part 1 companion paper

The Part 1 paper (Pöhlker et al., 2016) focuses on the multi-month variability in the Amazonian CCN population by presenting data from a full seasonal cycle. In particular, it presents annual averages of the key CCN parameters, a detailed analysis of the specific seasonal as well as diurnal cycles, and a systematic analysis of different CCN parametrization schemes to represent the Amazonian CCN cycling in modeling studies.

The major findings of Part 1 can be summarized as follows: (i) the CCN population in the central Amazon is predominantly defined by the overall aerosol concentration as well as the shape of the characteristic bimodal aerosol size distribution. Accordingly, a key property that has to be taken into account for the interpretation of the CCN results is the relative proportion of the Aitken and accumulation modes (mode maxima at $D_{Ait} \approx 70$ and $D_{Acc} \approx 150\,nm$). (ii) The hygroscopicity parameters, $\kappa(S, D_a)$ with D_a as the midpoint activation diameter, of the two modes were found to be remarkably stable for most of the observation period ($\kappa_{Ait} = 0.14 \pm 0.03$ vs. $\kappa_{Acc} = 0.22 \pm 0.05$), with only weak seasonal and no diurnal variability. Accordingly, we concluded in Part 1 that the shape of the aerosol size distribution is the predominant factor, whereas $\kappa(S, D_a)$ is only of secondary importance for the variability in the Amazonian CCN population, in agreement with previous studies (see references in Pöhlker et al., 2016). (iii) Furthermore, Part 1 summarizes the CCN key parameters that allow for efficient modeling of the Amazonian CCN population. The prediction of CCN concentrations is particularly reliable when time series of total aerosol concentration and/or the aerosol size distribution are available.

We emphasized CCN efficiency spectra, which can be regarded as CCN signatures for a particular aerosol population, by describing their behavior for the atmospherically relevant S range. Here, a rather simple analytical expression (i.e., single- or double-error-function fits) suffices to represent the essence of the CCN-relevant properties of an aerosol population, which includes the characteristic shape of the aerosol size distribution and the $\kappa(S, D_a)$ size dependence. Furthermore, the CCN efficiency spectra are independent of the total aerosol number concentration (in contrast to CCN spectra) and, thus, can be flexibly scaled to the concentration range of interest to obtain CCN concentrations at a certain S level. Finally, and beyond their potential use in models as CCN parametrization, the shape of the CCN efficiency spectra is very instructive for visualization of the specific behavior of contrasting aerosol population in cloud formation. This aspect will be one focal point of the present study.

1.2 Aims and scope of this study

To complete the analysis started in Part 1, this paper analyzes the CCN variability at the original time resolution ($\sim 4.5\,h$),

which is sufficient to resolve its short-term variability in relation to air mass changes as well as aerosol emission and transformation processes. In the present work, we will zoom into specific periods of the 1-year CCN data set in two steps: first, we discuss the aerosol and CCN variability for two contrasting 2-month periods that characterize the pollution minimum and maximum in relation to complementary trace gas and aerosol parameters. Second, we analyze the following four case studies, which represent characteristic events and conditions in the central Amazon region:

- During certain wet-season episodes, when no tracers of pollution aerosols are detectable anymore, the aerosol population can be regarded as empirically not distinguishable from pristine, i.e., completely unpolluted rain forest conditions. This empirically pristine state of the rain forest (PR) aerosol prevails during 10 to 40 days per year (depending on PR definition; see Sect. 2.7).
- Long-range-transport (LRT) aerosol advection during the wet season brings Saharan dust, African biomass burning smoke, and marine aerosol particles from the transatlantic passage. The LRT case study represents conditions that prevail between 50 and 60 days per year (see Moran-Zuloaga et al., 2017).
- Biomass burning (BB) smoke from man-made forest fires in the various deforestation hot spots in the basin influences the atmospheric state at ATTO almost permanently during the dry season and for extended episodes during the transition periods (> 100 days per year) (Saturno et al., 2017a). The BB case study in this work analyzes large deforestation fires in the southeastern basin, whose smoke reached ATTO after a few days of atmospheric processing. Accordingly, the BB case study characterizes the typical conditions of aged smoke influencing the atmospheric state at ATTO.
- Mixed pollution (MPOL) from African LRT and local/regional fires represents a frequent aerosol scenario at ATTO (Saturno et al., 2017a). The advected African aerosols mainly comprise biomass and fossil fuel combustions emissions, although the exact composition of these dry-season LRT plumes is still poorly analyzed. The MPOL case study focuses on a period when African volcanogenic aerosols were advected to ATTO – an event that has been well documented in Saturno et al. (2017b). We selected this episode since the microphysical properties of the volcanogenic aerosol are characteristic enough to discriminate them from the local/regional smoke emissions. Accordingly, the alternating pattern of LRT vs. local/regional pollution can be clearly resolved for the MPOL period. However, note that volcanogenic plumes are comparatively rare events, whereas African combustion emissions, which are much harder to discriminate from the local/regional emissions, are a more common scenario. Accordingly, the MPOL case study is an example of a complex aerosol mixture due to alternating African vs. local/region influences during the dry season.

In summary, the overall purpose of this study is to link the measured CCN abundance and properties with the characteristic emissions and transformation processes that govern the Amazonian aerosol population. With the CCN parametrization strategies developed in Part 1, we provide a basis for effective CCN prediction under characteristic aerosol and CCN conditions in the Amazon Basin.

2 Experimental section

2.1 Aerosol and trace gas measurements at the ATTO site

The present study is mostly based on in situ measurements at the remote ATTO site, which has been described in detail by Andreae et al. (2015). Further relevant information regarding the site, the measurement period, and the aerosol and trace gas instrumentation can be found in the Part 1 paper by Pöhlker et al. (2016). The time frame of the present analysis, including the four in-depth case studies, overlapped with the two intensive observation periods (IOPs) of the international Green Ocean Amazon 2014/5 (GoAmazon2014/5) campaign (Martin et al., 2016a, b). Specific details on the measurements of equivalent black carbon (BC_e) mass concentrations, M_{BC_e}, with the Multiangle Absorption Photometer (MAAP) can be found in Saturno et al. (2017a, c). Specific details on the measurements of the mole fraction of carbon monoxide (CO), c_{CO}, with a G1302 analyzer (Picarro Inc. Santa Clara, CA, USA) can be found in Winderlich et al. (2010).

Details on the Aerosol Chemical Speciation Monitor (ACSM, Aerodyne Research Inc., Billerica, MA, USA) measurements – which provide online information on the mass concentrations, $M_{species}$, of organics (OA), sulfate (SO_4^{2-}), nitrate (NO_3^-), ammonium (NH_4^+), and chloride (Cl^-) – can be found in Ng et al. (2011). A detailed description of the long-term operation of the ACSM at the ATTO site can be found in Carbone et al. (2017). For the selected case study and seasonal time frames, we calculated the mean values of $M_{species}$ as well as corresponding mass fractions, $f_{species}$, according to

$$f_{species} = \frac{M_{species}}{M_{OA} + M_{SO_4} + M_{NH_4} + M_{NO_3} + M_{Cl} + M_{BC_e}}. \quad (1)$$

Furthermore, predicted hygroscopicity parameters, κ_p, were calculated based on the ACSM and MAAP results according to the following procedure adapted from Gunthe et al. (2009), Rose et al. (2011), and Pöhlker et al. (2016):

$$\kappa_p = f_{OA} \cdot 0.1 + f_{inorg} \cdot 0.71 + f_{BCe} \cdot 0, \quad (2)$$

with f_{inorg} including SO_4^{2-}, NO_3^-, NH_4^+, and Cl^-. Note that M_{NH_4} ranged below its detection limit (i.e., 0.28 µg m^{-3}, for

30 min averaging time) during the clean Amazon wet-season months, making the obtained results unreliable (the questionable periods are marked in Table 3, which is discussed later in this study). For these periods with questionable results, M_{NH_4} was omitted in the calculation of the mass fractions, which has to be kept in mind in the interpretation of the results. M_{Cl} and M_{BC_e} were also below detection limits for certain conditions. Accordingly, κ_p was calculated without M_{NH_4}, $M_{Cl\text{-}}$, and/or M_{BC_e}. The nominal size range of the ACSM spans from 75 to 650 nm, and the measurements are conducted size-integrated. Accordingly, the ACSM results tend to be dominated by larger particles with relatively high masses, which makes the $M_{species}$ results mostly representative for the accumulation mode composition. Accordingly, the calculated κ_p was compared to the hygroscopicity parameter for the lowest measured S level, $\kappa(0.11\,\%)$, corresponding to the largest measured critical diameter ($D_a \approx 170$ nm).

2.2 CCN measurements and data analysis

A detailed description of the operation of the CCN counter (CCNC) and the subsequent data analysis can be found in the companion paper (Pöhlker et al., 2016), which is the basis for the present study. Briefly, size-resolved CCN measurements were conducted using a continuous-flow streamwise thermal-gradient CCN counter (model CCN-100, DMT, Longmont, CO, USA) in combination with a differential mobility analyzer (DMA, model M, Grimm Aerosol Technik, Ainring, Germany) and a condensation particle counter (Grimm Aerosol Technik). The DMA-selected size range spans from 20 to 245 nm. The analyzed supersaturation range spans from 0.11 to 1.10 %. A complete measurement cycle with scanning of all particle diameters and supersaturations took ∼ 4.5 h. For further CCN-relevant information, we refer the reader to Rose et al. (2008) and Krüger et al. (2014).

The CCN efficiency spectra parameterization as introduced in Part 1 plays a key role in the present paper. Note that we slightly revised and improved the fitting procedure from the Part 1 companion paper. The main change implies that the fits are now forced through zero, which is physically more plausible and makes the single-error-function (erf) fit parametrization more applicable for modeling studies. The erf fit (mode = 1) is represented by the following function:

$$\frac{N_{CCN}(S)}{N_{CN,10}} = \frac{a_1}{2} + \frac{a_1}{2} \cdot \mathrm{erf}\left(\frac{\ln \frac{S}{S_1}}{w_1}\right), \quad (3)$$

with a_1 as a prefactor; S_1 as the supersaturation, at which half of the maximum activated fraction (MAF) of the aerosol particles acts as CCN (e.g., 50 % for $a_1 = 1$); and w_1 as the width of the erf fit. To simplify the fitting procedure, $a_1 = 1$ was assumed. For $a_1 = 1$ the erf converges against unity, corresponding to an activation of all particles as CCN at high S, which is adequate in most cases. Analogously, the double-erf fit (mode = 2) is represented by the function

$$\frac{N_{CCN}(S)}{N_{CN,10}} = \frac{a_1}{2} + \frac{a_2}{2} \cdot \mathrm{erf}\left(\frac{\ln \frac{S}{S_1}}{w_1}\right) + \left(\frac{a_1 - a_2}{2}\right) \cdot \mathrm{erf}\left(\frac{\ln \frac{S}{S_2}}{w_2}\right), \quad (4)$$

with index 1 and 2 specifying the variables for both modes. To simplify the fitting procedure, $a_1 = 1$ was assumed.

Note further that in Part 1 we tested different reference aerosol number concentrations, $N_{CN,Dcut}$ (e.g., $N_{CN,10}$ and $N_{CN,50}$), for the CCN efficiency spectra parametrization. In this study, we use only one reference concentration for clarity – namely $N_{CN,10}$. The choice of $N_{CN,10}$ can be explained by the fact that it is experimentally rather easily accessible (e.g., via condensation particle counter, CPC, measurements), whereas reference concentrations such as $N_{CN,50}$ require more elaborated experimental setups (e.g., Scanning Mobility Particle Sizer, SMPS, data).

The κ distributions were calculated according to the procedure reported in Su et al. (2010) for every individual CCN measurement cycle and subsequently averaged for time periods of interest. The corresponding N_{CN} κ distributions were obtained by multiplication of the average κ distributions with the average N_{CN} size distributions within the same time frame. The entire CCN analysis was conducted in IGOR Pro (Wavemetrics, Inc., Portland, OR, USA).

2.3 Backward trajectories

The backward-trajectory (BT) analysis and classification in this study has been adopted from C. Pöhlker et al. (2018), where an in-depth description of the procedure can be found. Briefly, the BT analysis is based on the Hybrid Single Particle Lagrangian Integrated Trajectory Model (HYSPLIT, NOAA-ARL) with meteorological input data from the Global Data Assimilation System (GDAS1) (Draxler and Hess, 1998). Three-day BTs have been calculated every 1 h with a starting height of 1000 m above ground level (a.g.l.) at the ATTO site for the time period of 1 January 2008 until 30 June 2016. A sensitivity test confirmed that starting heights of the BTs at 200 and 1000 m a.g.l. gave similar results. Accordingly, the chosen start height at 1000 m appears to be a good representation of the origin of the boundary layer (BL) air masses at ATTO. Subsequently, the resulting ensemble of 74 496 individual BTs was classified into 15 clusters with k-means cluster analysis (CA). Figure S1 in the Supplement shows a map of the northeastern Amazon Basin with the ATTO site and the mean track of the 15 BT clusters. It illustrates that the air masses arrive almost exclusively in a rather narrow easterly wind sector (between 45 and 120°). Within this sector, four main directions of air mass advection can be identified: (i) a northeasterly (NE) track including the clusters NE1, NE2, and NE3; (ii) an east-northeasterly (ENE) track including the clusters ENE1, ENE2, ENE3, and ENE4; (iii) an easterly (E) track including the clusters E1, E2, E3, and E4; and (iv) a group of "inland" trajectories in east-southeasterly (ESE) directions including clusters ESE1, ESE2, and ESE3 as well as

one cluster towards the southwest (SW1). For a detailed characterization of the land cover, including potential trace gas, aerosol, and CCN sources, within the BT-derived footprint region of the ATTO site, we refer the reader to C. Pöhlker et al. (2018).

2.4 Satellite data and analysis

The satellite data products used in this study were obtained from the NASA Giovanni web interface (http://giovanni.gsfc.nasa.gov/; last access: 26 May 2017), developed and maintained by the NASA Goddard Earth Sciences Data and Information Services Center (GES DISC) (Acker and Leptoukh, 2007). The following satellite products were used:

- Cloud top temperature data (AIRX3STD_v006 product) from the atmospheric infrared sounder (AIRS) instruments on board the satellites Terra and Aqua (data included from 4 July 2002 to 30 June 2016). For the corresponding time series in this study, the Aqua and Terra data were averaged per day for a representative region (i.e., $\mathrm{ROI_{ATTO}}$; see below).
- Cloud cover data were obtained by the Moderate Resolution Imaging Spectroradiometer (MODIS) on board the Terra and Aqua satellites (included data from 4 July 2002 to 30 June 2016). The obtained Aqua and Terra time series were averaged for the $\mathrm{ROI_{ATTO}}$. Note that cloud cover strongly depends on the spatial resolution of the instrument as outlined in King et al. (2013).
- Cloud droplet effective radius, r_e, data were calculated from MODIS products (included data from 4 July 2002 to 30 June 2016) for the $\mathrm{ROI_{ATTO}}$. Since r_e varies with vertical cloud development and total CCN abundance, we filtered the r_e data by cloud top temperature (King et al., 2013).
- Precipitation rate data, P_TRMM, are obtained from the Tropical Rainfall Measuring Mission (TRMM) within the $\mathrm{ROI_{ATTO}}$. The TRMM_3B42_Daily_v7 product was used for the time period 1 January 1998 until 30 June 2016.

The satellite data were used as time series of area-averaged data products within a region of interest around the ATTO site ($\mathrm{ROI_{ATTO}}$: 3.5° S–2.4° N, 59.5–54° W) as specified in Fig. S1.

2.5 Seasonal cycles of remote-sensing and in situ data

To provide an overall picture of the seasonal cycle of selected aerosol, meteorological, and cloud microphysical parameters representative for the ATTO region, various multi-year data sets were analyzed and compared. Remote-sensing data products were used in the time frames outlined in Sect. 2.4. For $M_{\mathrm{BC_e}}$, c_CO, and the particle concentrations in the accumulation mode range (N_acc), in the Aitken mode range (N_Ait), and in the total particle population ($N_{\mathrm{CN},10}$), 4–6 years of ATTO site measurements were available. Additionally, $M_{\mathrm{BC_e}}$ data measured at the ZF2 site, located 40 km northwest of Manaus, were used to reflect the conditions back to 2008 (e.g., Martin et al., 2010a). In terms of sources and conditions, the ATTO and ZF2 sites are comparable (Saturno et al., 2017a; C. Pöhlker et al., 2018). Accordingly, combined $M_{\mathrm{BC_e}}$ time series from ATTO and ZF2 spanning from January 2008 to May 2017 were included here. The c_CO data include ATTO measurements from March 2012 to April 2017. The N_acc, N_Ait, and $N_{\mathrm{CN},10}$ data are based on SMPS measurements at ATTO from February 2014 to January 2017.

2.6 Aerosol sampling and scanning electron microscopy with X-ray spectroscopy

Aerosol samples for electron microspectroscopy were collected by impaction. A homemade single-stage impactor (flow rate = 1–1.5 L min^{-1}; nominal cut-off: $D_\mathrm{cut} \approx 500$ nm) was used for collection. The collection efficiency below D_cut decreases steeply; however, a certain fraction of particles in this size range is still collected. Moreover, a fraction of very small particles is additionally collected via diffusive deposition and therefore available for the microscopic analysis. Aerosol particles were deposited onto silicon nitride substrates (Si_3N_4; membrane width: 500 µm; membrane thicknesses: 100 or 150 nm; Silson Ltd., Northhampton, UK). Immediately after sampling, samples were stored in airtight containers at −20 °C.

Without further treatment like sputter coating, particles were analyzed in a high-resolution scanning electron microscope (SEM; FEI Quanta 200F, FEI, Eindhoven, the Netherlands). An acceleration voltage of 12.5 kV with a spot size of approximately 3 nm was used. X-ray emission was analyzed using energy-dispersive X-ray analysis (EDX; Edax Genesis, Edax Inc.). The system is able to record characteristic X-ray emissions for all elements with $Z > 5$. Obviously, in the present work Si could not be quantified due to the Si_3N_4 substrate (Kandler et al., 2011).

2.7 Definition of empirically pristine rain forest aerosol conditions at ATTO

The term pristine is bound to a pre-human reference state with prevailing natural atmospheric conditions, in the absence of any anthropogenic influences. Andreae (2007) pointed out that in the present-day atmosphere "there are no places where we can expect to find truly pristine conditions". This is particularly true with respect to long-lived trace gases, such as CO_2 and CH_4, which have accumulated in the atmosphere due to man-made activities. However, the aerosol abundance and composition are also substantially perturbed by anthropogenic emissions. This also includes aerosols at remote locations, which are altered to varying degrees by a

globally pervasive background pollution. It has been controversially debated if and to what extent certain marine and remote continental locations still approximate pristine atmospheric conditions (e.g., Andreae, 2009; Martin et al., 2010b; Pöschl et al., 2010; Chi et al., 2013; Hamilton et al., 2014). Frequently, conditions with low anthropogenic influences are characterized as "clean" or "near pristine", although these terms are rather differently and often vaguely defined. The discussion is inherently difficult since truly pristine conditions are not available anymore to quantify how close the present-day atmosphere still gets to its original pre-human state. Accordingly, truly pristine conditions remain hypothetical, and any degree of a near-pristine state has to be defined indirectly with respect to the absence of man-made emissions.

In the Amazon Basin, aerosol conditions during most of the wet season are comparatively clean with low – though detectable – concentrations of background pollution. During the multi-month wet-season period that can overall be characterized as near pristine, certain episodes can be identified where pollution concentrations drop even further and below analytical detection limits. Under these conditions, the aerosol composition can be regarded as empirically undistinguishable from a pristine state. The present study uses these episodes to operationally define a pristine state of the aerosol composition and properties in a tropical rain forest environment, which we call empirically pristine rain forest (PR) aerosol.

The selection of a robust marker is crucial for the assessment of the PR state. In previous studies, the concentrations of BC, CO, and CN as well as the air mass origin by means of BTs have been used as corresponding markers at other locations; however all of them are characterized by certain limitations (Hamilton et al., 2014, and reference therein). For the present study, we explored the suitability of BC, CO, CN, and BTs as well as combinations of them as PR markers. Their strengths and limitations can be summarized as follows:

- BT-based PR filter: BTs help to identify periods with comparatively clean air mass advection due to fact that the BTs which reach furthest to the northeast across the South American continent overpass the largest fraction of uninhibited and, thus, untouched forest regions (C. Pöhlker et al., 2018). Accordingly, a BT filter allows local and regional sources of anthropogenic pollution to be excluded. However, BTs do not allow long-range-transport aerosols to be filtered out reliably, particularly from African sources. Accordingly, BTs are not suitable as a stand-alone PR filter; however, they are useful in combination with other PR markers as outlined below.

- CN-based PR filter: the total particle concentration per se is not a good filter for clean or (near-)pristine states since natural aerosol conditions range from very low (e.g., N_{CN} in Antarctica reaching down to $10\,cm^{-3}$; Fiebig et al., 2014) to very high concentrations (e.g., N_{CN} in the upper troposphere (UT) reaching above $10\,000\,cm^{-3}$; Andreae et al., 2018). Accordingly, N_{CN} is also not a good stand-alone PR filter. However, with respect to the "typical" Amazonian aerosol concentrations in the boundary layer (i.e., a few hundred up to few thousand particles per cubic meter), the total particle concentrations provide at least a helpful reference level for the extent of pollution.

- BC-based definition of PR, called PR_{BC}: BC represents a unique indicator for combustion aerosol particles, which in the Amazon Basin almost entirely originate from anthropogenic sources (i.e., fossil fuel and biomass burning in South American and Africa). Accordingly, we defined PR_{BC} episodes by means of the absence of detectable BC_e. Petzold and Schönlinner (2004) determined the detection limit of the MAAP "as the minimum resolvable absorbance" by considering "the variability of blank filter optical properties". The detection limit corresponds to the resulting mean absorbance of the blank filter $+3\times$ the standard deviation (SD) resulting in an absorption coefficient of $0.132\,Mm^{-1}$ for 30 min averages. The M_{BC_e} was calculated by using mass absorption cross sections (MACs) retrieved by fitting MAAP absorption coefficients at 637 nm and Single Particle Soot Photometer (SP2) rBC mass measurements during the different seasons as explained in Saturno et al. (2017a, c). Using the MAC values measured at ATTO (MAC for the wet season: $11.4 \pm 1.2\,m^2\,g^{-1}$; MAC for the dry season: $12.3 \pm 1.3\,m^2\,g^{-1}$), the conversion to M_{BC_e} corresponds to 0.011–0.012 $\mu g\,m^{-3}$. Note that this threshold would be higher if a "traditional" MAC value of $6.6\,m^2\,g^{-1}$ were used to calculate M_{BC_e} ($\sim 0.019\,\mu g\,m^{-3}$). Here, we selected a threshold concentration of $M^*_{BC_e} = 0.01\,\mu g\,m^{-3}$ when the ATTO-specific MAC values are taken into account. Accordingly, PR_{BC} periods fulfill the criterion $M_{BC_e} < M^*_{BC_e}$ for ≥ 6 h (after applying a five-point running average to the 1 h M_{BC_e} data).

- CO-based definition of PR, called PR_{CO}: the BC approach has the potential drawback that it may overemphasize periods with strong precipitation, since heavy rain removes the BC/aerosol content in actually polluted air masses irrespective of the gas phase composition (see Hamilton et al., 2014). Accordingly, the PR_{CO} filter is based on the gas phase combustion marker, CO. In our definition, PR_{CO} conditions prevailed during periods in which the ATTO c_{CO} concentrations dropped below the monthly background CO levels at the following reference stations (https://www.esrl.noaa.gov/gmd/dv/site/CPT.html; last access: 7 April 2018): whenever the ATTO c_{CO} data were associated with northern hemispheric (NH) BTs (i.e., NE or ENE BT clusters, Fig. S1)

and dropped below the average of the monthly CO levels obtained at the three background stations at Ragged Point in Barbados (RPB), Assekrem in Algeria (ASK), and Izaña in Cape Verde (IZO), the episode was flagged as PR_{CO}. Analogously, whenever the ATTO c_{CO} data were associated with southern hemispheric (SH) BTs (i.e., E and ESE BT clusters) and dropped below the monthly CO levels obtained at the background station on Ascension Island (ACS), the episode was also flagged as PR_{CO}. Note that the time series of monthly c_{CO} levels from the reference stations was linearly interpolated to hourly values for the comparison with ATTO c_{CO} data. The BTs from the northern hemisphere (i.e., NE and ENE BT clusters) account for ∼ 70 % of all BTs during the wet season. Among these ∼ 70, ∼ 30 % can be attributed to the NE BT clusters. The locations of the CO background stations, the wet-season ATTO BT ensemble, and the hemispheric CO distribution are shown in Fig. S2.

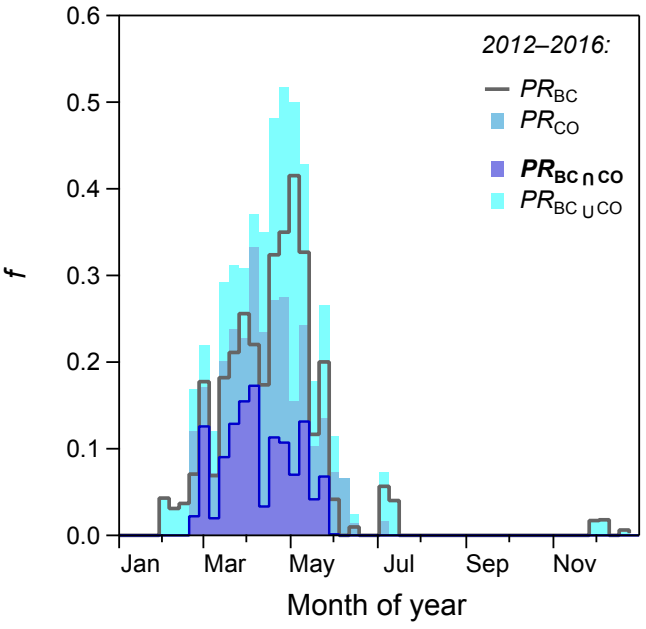

Figure 1. Seasonality of frequency of occurrence, f, of empirically pristine rain forest (PR) aerosol conditions at ATTO by means of PR_{BC}, PR_{CO}, $PR_{BC\cap CO}$, and $PR_{BC\cup CO}$ filters (see Sect. 2.7). $PR_{BC\cap CO}$ as the most robust case is used as the main PR filter throughout this work. Data are shown as weekly averages for the time period from March 2012 until June 2016. An analogous representation for the year 2014 as the CCN focal period of this study is shown in Fig. S4.

The seasonality in the frequency of occurrence, f, of the PR_{BC} and PR_{CO} filters is generally very similar, as shown in Fig. 1: the first PR_{BC} and PR_{CO} episodes occur in February. Their highest f is reached around the second half of April and the first half of May. Afterwards, f decreases steeply and PR conditions occur only occasionally in June and July. Overall, PR_{BC} and PR_{CO} episodes overlap ∼ 25 % of the total time that is flagged by at least one of the two filters. Since both approaches are associated with certain limitations and uncertainties, we further analyzed two combinations of PR_{BC} and PR_{CO}: the union of both sets ($PR_{BC\cup CO}$) and the intersection of both sets ($PR_{BC\cap CO}$) as shown in Fig. 1. For the in-depth analysis of aerosol and CCN properties in this work, we chose the $PR_{BC\cap CO}$ filter, which we consider as the most strict and, thus, robust since the criteria of both filters have to be fulfilled.

With respect to the PR filters, the following aspects are worth mentioning: PR episodes at ATTO exclusively occur during the wet season due to a combination of two effects. First, the ATTO site is very remote and the characteristic wet-season air mass advection occurs mostly over uninhabited areas (see C. Pöhlker et al., 2018). Second, the high precipitation rates entail strong scavenging and, thus, relatively short aerosol particle lifetimes, which reduces the long-range transport of the background pollution aerosol load. In contrast, dry-season PR episodes have almost never been observed at ATTO due to the extensive biomass burning emissions in South America and Africa in combination with low scavenging rates and, thus, long atmospheric aerosol lifetimes. This is relevant since wet- vs. dry-season conditions were likely associated with different atmospheric states, for example with respect to volatile organic compound (VOC) concentrations and aerosol populations as well as photochemical conditions. While wet-season PR states are still experimentally accessible as outlined in this work, the dry-season PR state appears to be entirely swamped by pollution.

The primary filters are based on the combustion markers BC and CO, which do not allow a discrimination between wildfires and man-made fires. Accordingly, the contribution of wildfire emissions, which were part of an originally pristine atmosphere in the Amazon, is erroneously filtered out. Generally, wildfires in the tropical Amazonian forests are rare events due to the fact that the dense and moist canopies – if unperturbed – effectively maintain a fire-immune state (e.g., Cochrane, 2003; Nepstad et al., 2008). Nevertheless, wildfires play a certain, although minor, role for the ATTO observations, since the wet-season BTs cover the Guianan savanna ecoregions that account for ∼ 8 % of the ATTO footprint region (Olson et al., 2001; C. Pöhlker et al., 2018). Within these regions, the infrequent occurrence of wildfires is part of the savanna-specific fire regime (de Carvalho and Mustin, 2017). Figure S3 illustrates the relevance of wildfires for ATTO under wet-season conditions.

Moreover, Saharan dust as well as marine aerosols from the Atlantic Ocean are advected towards the ATTO region via wet-season LRT plumes, which are most frequent in February and March (Moran-Zuloaga et al., 2017). Saharan dust and marine aerosols can also be considered as part of an original pristine atmospheric state in the Amazon. However, all

LRT plumes arriving at ATTO are filtered out by the PR_{BC} and PR_{CO} approaches due to the fact that virtually all LRT plumes contain a substantial fraction of smoke from mostly man-made fires in West Africa (Moran-Zuloaga et al., 2017). Accordingly, the role of the present-day LRT plumes arriving at ATTO has to be differentiated carefully as they represent a (partly internal) mixture of natural and anthropogenic aerosols.

3 Results and discussion

3.1 Aerosol and cloud microphysical seasonality in the Amazon

Prior to the in-depth analysis of the aerosol and CCN cycling for characteristic conditions, this section provides an overview of the aerosol and cloud microphysical seasonality in the ATTO region. The pollution markers c_{CO} and M_{BC_e} in Fig. 2a show a pronounced seasonal cycle with a prevalence of clean conditions in the wet season vs. the biomass-burning-related pollution maximum in the dry season (Andreae et al., 2015). The annual minimum in M_{BC_e} levels occurs at the end of April (with weekly M_{BC_e} means of $\sim 0.03\,\mu g\,m^{-3}$), whereas its highest concentrations were observed in August and September (with weekly M_{BC_e} means of $\sim 0.40\,\mu g\,m^{-3}$). The seasonal cycle of c_{CO} shows a temporal shift of about 1 month with its minimum in the beginning of June (with weekly c_{CO} means ~ 100 ppb) and largest values from October to December (with weekly c_{CO} means ~ 200 ppb). The phase shift between the c_{CO} and M_{BC_e} seasonality can be explained by the spatiotemporal interplay of combustion-related BC and CO sources, aerosol wet scavenging, and alternating advection of NH vs. SH air masses (Martin et al., 2010b; Andreae et al., 2012, 2015). Similar to the M_{BC_e} trends, the total aerosol particle concentration, $N_{CN,10}$, tracks the seasonality in biomass burning activities (in South America and Africa) with lowest concentrations in March and April ($N_{CN,10}$ weekly means from 200 to 300 cm^{-3}) and highest values between August and November ($N_{CN,10}$ weekly means from 1000 to 2000 cm^{-3}) as shown in Fig. 2b. The CCN concentrations at a supersaturation of 0.5 %, $N_{CCN}(0.5\,\%)$, which were calculated based on long-term SMPS data and the κ-Köhler parametrization as outlined in our Part 1 paper, mostly tracked the seasonal trends in $N_{CN,10}$. Its minimum around March and April showed weekly mean $N_{CCN}(0.5\,\%)$ values around 200 cm^{-3}, whereas the maximum showed values between 1000 and 2000 cm^{-3}.

Figure 2c shows the seasonal cycles of two precipitation data products: first, P_{TRMM} data represent the area-averaged precipitation rate in the ROI_{ATTO} (see Fig. S1). The P_{TRMM} data reveal a rather broad wet-season precipitation maximum from March to May. The smallest precipitation rates are observed from September to November. Second, the P_{BT} data

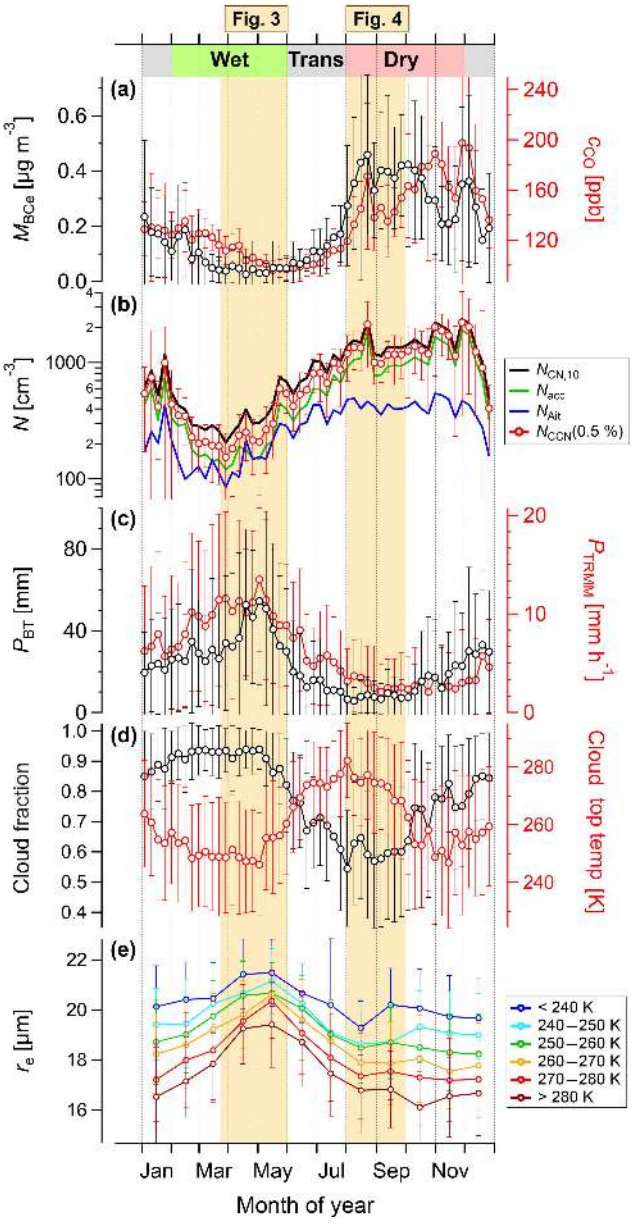

Figure 2. Seasonal cycle of selected trace gas, aerosol, and cloud microphysical parameters. **(a)** Pollution tracers, M_{BC_e} and c_{CO}. **(b)** Total aerosol number concentration, $N_{CN,10}$; Aitken mode number concentration, N_{Ait}; accumulation mode concentration, N_{acc}; and CCN number concentration at $S = 0.5\,\%$, $N_{CCN}(0.5\,\%)$. **(c)** Precipitation products, P_{BT}, representing cumulative precipitation along BT tracks, and P_{TRMM}, representing TRMM-derived precipitation within the ROI_{ATTO} as defined in Fig. S1. **(d)** Satellite-derived cloud fraction and cloud top temperature within the ROI_{ATTO}. **(e)** Satellite-derived cloud droplet effective radius, r_e, within the ROI_{ATTO}. For a detailed characterization of the land use and recent land use change in the ATTO footprint, including the ROI_{ATTO}, we refer to C. Pöhlker et al. (2018). Data in **(a)** to **(d)** are shown as weekly averages. Data in **(e)** are shown as monthly averages. Error bars represent 1 standard deviation. Vertical orange shading represents 2-month time in 2014 frames of representative clean and polluted conditions as shown in detail in Figs. 3 and 4.

represent the cumulative precipitation along the BTs arriving at ATTO (for details see C. Pöhlker et al., 2018). Thus, P_{BT} represents a measure for the extent of rain-related aerosol scavenging – particularly of long-range-transport aerosols – during air mass transport towards ATTO. A pronounced maximum in P_{BT} and the related scavenging is observed for the months April and May, which coincides with the minimum in aerosol parameters (i.e., M_{BC_e} and $N_{CN,10}$) (see also Moran-Zuloaga et al., 2017).

Figure 2d shows the seasonal cycles in cloud fraction and cloud top temperature within the ROI_{ATTO}. Both are predominantly influenced by the position of the ITCZ with its belt of extended deep convective cloud systems and strong precipitation (e.g., Moran-Zuloaga et al., 2017). According to Fig. 2d, the densest cloud cover and deepest convection (represented by lowest cloud top temperature) occurs upon northerly passage of the ITCZ in the middle of the wet season (i.e., March and April) as well as upon southerly passage of the ITCZ at the end of the dry season (around November). The maximum in deep convection in March and April – expectedly – corresponds to the peak in P_{TRMM}. A global picture of the spatiotemporal trends in cloud microphysical properties can be found in King et al. (2013).

Figure 2e presents the satellite-derived effective radius, r_e, of liquid cloud droplets that links the seasonality in aerosol and cloud properties. The r_e data have been filtered by cloud top temperature to discriminate the different r_e growth states at different heights of the convective clouds. It is well established that increased CCN loads entail an influence on cloud properties, which typically results in a corresponding decrease in droplet diameter (e.g., Freud et al., 2008; Stevens and Feingold, 2009). Figure 2e underlines this behavior by means of a clear seasonality in r_e with its maximum during the clean wet season (i.e., April and May) and its minimum during the polluted dry season (i.e., August to November). A detailed understanding of the impact of the CCN loading on the cloud microphysical properties, however, is the subject of ongoing studies at ATTO and further locations worldwide.

In essence, Fig. 2 provides a coherent picture of the aerosol, cloud, and precipitation seasonality as well as their corresponding linkages. The following sections will zoom into this overall picture by presenting detailed aerosol and CCN data from characteristic wet- and dry-season conditions of the year 2014.

3.2 Aerosol and CCN time series for representative wet-season conditions

During the Amazonian wet season (February to May), the influence of local and regional anthropogenic pollution (i.e., from biomass burning) decreases to a minimum, and simultaneous strong precipitation causes efficient aerosol scavenging (see Fig. 2). The combination of both effects results in a comparatively clean state of the Amazonian atmosphere (Martin et al., 2010b; Andreae et al., 2015). During this time of the year, biogenic aerosols from the surrounding rain forest ecosystem, such as secondary organic aerosol (SOA) from the oxidation of biogenic volatile organic compounds (BVOCs) as well as primary biological aerosol particles (PBAP), prevail (Pöschl et al., 2010; Huffman et al., 2012; Yañez-Serrano et al., 2015). However, the regionally and biogenically dominated background state of the atmosphere is frequently perturbed by the episodic advection of LRT aerosols from Africa in air masses that bypass the major rain fields and, therefore, "survive" the intense scavenging (Moran-Zuloaga et al., 2017). The frequent intrusion of LRT aerosols is a characteristic feature during the Amazonian wet season and represents a strong and important influence on the rain forest ecosystem (e.g., Chen et al., 2009; Bristow et al., 2010; Baars et al., 2011; Abouchami et al., 2013; Yu et al., 2015; Rizzolo et al., 2017). These LRT plumes mostly comprise a complex mixture of Saharan dust, African biomass burning smoke, and marine aerosols from the transatlantic air passage (e.g., Talbot et al., 1990; Swap et al., 1992; Gläser et al., 2015).

The 2-month period in Fig. 3 can be regarded as representative for typical wet-season conditions in the ATTO region as it includes both scenarios: periods with a prevalence of the local (biogenic) background aerosol and episodes under the influence of LRT plumes, as well as intermediate states. In general, the wet season of 2014 showed average hydrological conditions without significant precipitation anomalies within the ROI_{ATTO}, which is in stark contrast to 2015/16 with its pronounced El Niño influence and an associated negative precipitation anomaly (see C. Pöhlker et al., 2018; Saturno et al., 2017a). Furthermore, the pollution tracers – $N_{CN,10}$, M_{BC_e}, and c_{CO} – showed comparatively low values with concentrations around $N_{CN,10} = 330 \pm 130\,cm^{-3}$, $M_{BC_e} = 0.03 \pm 0.05\,\mu g\,m^{-3}$, and $c_{CO} = 110 \pm 10\,ppb$ (given as mean $\pm$ 1 SD for the entire time period in Fig. 3) in agreement with previous studies (e.g., Andreae et al., 2012, 2015; Artaxo et al., 2013). In terms of atmospheric circulation, the first half of the 2-month time frame was dominated by backward-trajectory arrivals from the northeast (blue and green BT clusters; see Figs. 3a and S1), whereas during the second half the dominant wind direction shifted towards easterly directions (orange and red BT clusters; see Figs. 3a and S1) (compare Andreae et al., 2015; Moran-Zuloaga et al., 2017). This gradual swing of the dominant wind direction from NH to SH relates to the northwards movement of the ITCZ.

In Fig. 3, the orange background shading emphasizes several episodes with detectable LRT influence, according to Moran-Zuloaga et al. (2017). A comparatively strong LRT plume at ATTO – labeled as LRT case study in Fig. 3 – is the subject of a detailed CCN analysis in Sect. 3.5. The interested reader will find further in-depth analysis of this particular LRT event in Moran-Zuloaga et al., 2017 (where it is discussed as event "2014_7"). Andreae et al. (2012) argued that the "atmospheric state and processes in the Ama-

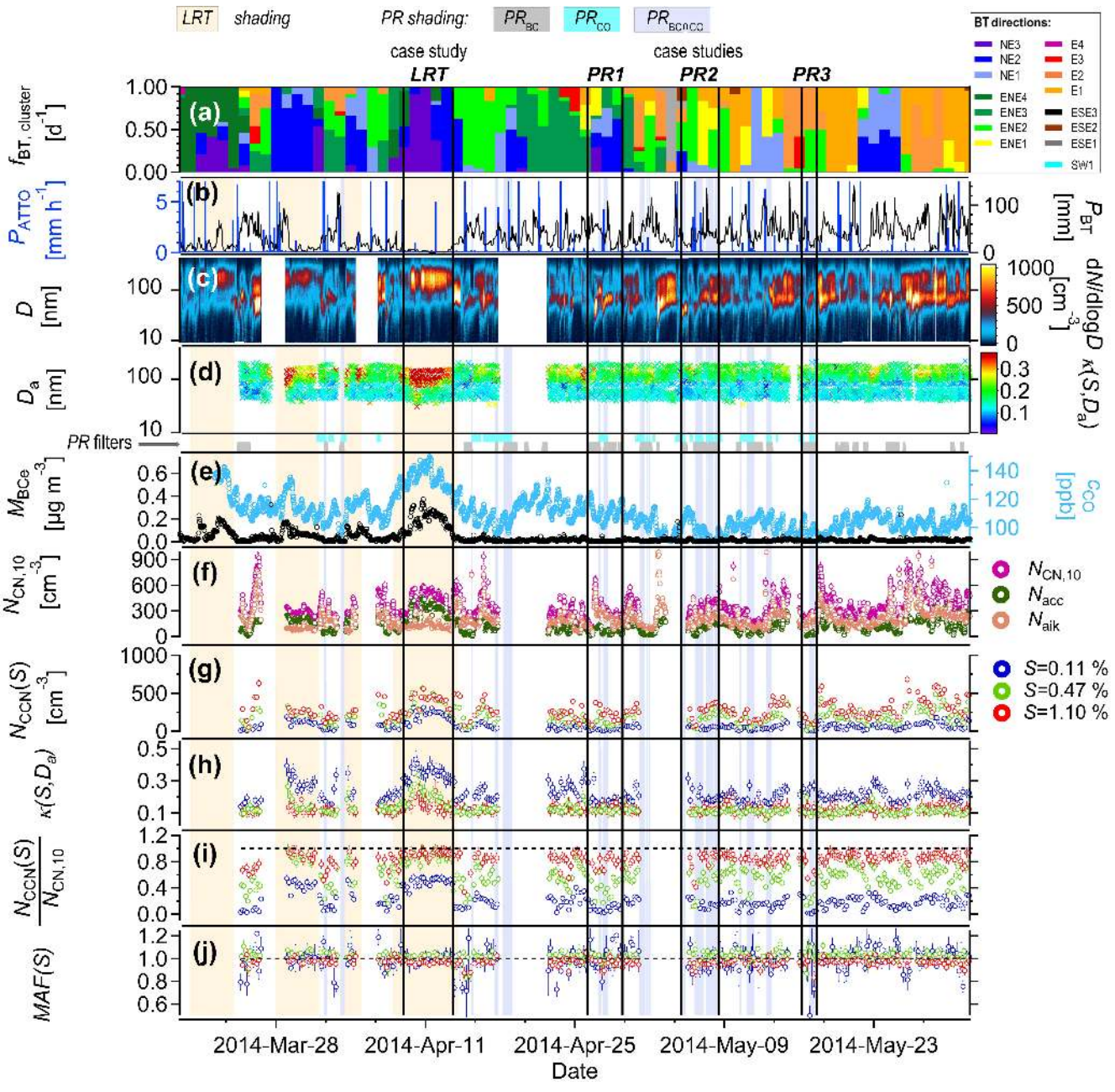

Figure 3. Overview plot illustrating selected meteorological, trace gas, aerosol, and CCN time series for representative wet-season conditions in the central Amazon. The shown time period from 23 March to 31 May covers a comparatively clean and extended time frame throughout the entire CCN measurement period. Individual panels represent **(a)** daily frequency of occurrence of 15 different BT clusters, $f_{\mathrm{BT,cluster}}$, with color code corresponding to Fig. S1; **(b)** precipitation rate (P_{ATTO}) measured locally at ATTO and cumulative precipitation from BT analysis (P_{BT}) as a measure for aerosol wet deposition; **(c)** SMPS-derived time series of number size distributions spanning nucleation, Aitken, and accumulation modes; **(d)** CCNC-derived time series of $\kappa(S, D_{\mathrm{a}})$ size distributions; **(e)** concentrations of biomass burning tracers, CO mole fraction (c_{CO}) and $\mathrm{BC_e}$ mass concentration ($M_{\mathrm{BC_e}}$); **(f)** total number concentrations of the entire aerosol population ($N_{\mathrm{CN,10}}$), Aitken mode particles (N_{Ait}); and accumulation mode particles (N_{acc}); **(g)** CCN concentrations, $N_{\mathrm{CCN}}(S)$, for selected supersaturations S; **(h)** hygroscopicity parameter, $\kappa(S, D_{\mathrm{a}})$, for selected S; **(i)** CCN efficiencies, $N_{\mathrm{CCN}}(S)/N_{\mathrm{CN,10}}$, for selected S; and **(j)** maximum activated fraction, MAF(S), for selected S. All CCN data are provided at the original time resolution of about 4.5 h. Light blue vertical shadings represent empirically pristine rain forest (PR) aerosol conditions according to the $\mathrm{PR_{BC\cap CO}}$ filter as defined in Sect. 2.7. Vertical lines highlight PR1, PR2, and PR3 periods selected for detailed analysis in Sect. 3.4. Light orange shading represents LRT episodes according to Moran-Zuloaga et al. (2017). Vertical lines highlight LRT case study for detailed analysis in Sect. 3.5.

zon Basin cannot be understood without the consideration of pollutant inputs by long-range transport". This is evidently true for the major LRT plumes in Fig. 3 with M_{BC_e} reaching up to $0.3\,\mu g\,m^{-3}$ as well as associated increases in N_{acc}. However, a closer analysis of the extended and relatively clean period from 14 April until 31 May 2014 also reveals that during $\sim 85\,\%$ of the time detectable amounts of background pollution were present (i.e., M_{BC_e} exceeding $M_{BC_e}*$; see Sect. 2.7). Although (highly) diluted, the advected aerosols can impact the CCN population, as discussed in Sect. 3.4. Only when pollution levels actually drop below detection limits and the conditions satisfy our rather strict $PR_{BC\cap CO}$ filter do empirically pristine aerosol conditions prevail, which are emphasized by a blue shading in Fig. 3. A statistical overview of the relative fraction of PR episodes for the years 2012 to 2016 is shown in Fig. 1. It shows that PR conditions typically occur from March to May, with their highest abundance around late April and early May, when weekly frequencies of occurrence reach up to $\sim 20\,\%$, according to the strict $PR_{BC\cap CO}$ filter, or even higher. Note that the PR episodes in 2014 mostly occurred in April and May (compare Figs. 3 and S4), which is in good agreement with the multi-year observations.

The following picture emerges for the CCN parameters: the time series of the $\kappa(S, D_a)$ size distributions in Fig. 3d clearly illustrates the different $\kappa(S, D_a)$ of Aitken and accumulation modes as discussed in our Part 1 study (Pöhlker et al., 2016). Overall, $\kappa(S, D_a)$ shows a clear variability for low S, representing the accumulation mode, and rather stable values for higher S, representing the Aitken mode (see Fig. 3h). The occurrence of the LRT plumes stands out clearly by causing a significant enhancement of $\kappa(S, D_a)$, with κ_{Acc} reaching 0.4 and κ_{Ait} reaching 0.25 (see Fig. 3d and h). Moreover, the LRT events are also associated with increased $N_{CCN}(S)$ and $N_{CCN}(S)/N_{CN}$ values (Fig. 3g and i). Note that the occurrence of the LRT events precisely coincides with the minima in P_{BT} and, thus, "windows" in aerosol scavenging (see Moran-Zuloaga et al., 2017).

For the extended and comparatively clean period from 14 April until end of May, the SMPS contour plot (Fig. 3c) reveals equally strong Aiken and accumulation modes as well as a "patchy" appearance, due to frequent rainfall causing (local) aerosol scavenging. As outlined in Part 1, the aerosol abundance in the particle size range >40 nm predominantly defined the measured CCN population (Pöhlker et al., 2016). Accordingly, the $N_{CCN}(S)$ and $N_{CCN}(S)/N_{CN}$ time series directly track the SMPS-derived patchy pattern. The low S levels (i.e., $N_{CCN}(0.11\,\%)$), which do not activate Aitken mode particles, closely followed the accumulation mode concentration, N_{acc}, time series, whereas the higher S levels (i.e., $N_{CCN}(1.10\,\%)$), which also activated particles in the Aitken mode, closely tracked $N_{CN,10}$ $(= N_{Ait} + N_{acc})$. Two of the subsequent case studies will focus in more detail on the specific CCN properties of the PR (Sect. 3.4) and LRT (Sect. 3.5) conditions (see also Table 1).

3.3 Aerosol and CCN time series for representative dry-season conditions

During the dry season (August to November), the central Amazon is under continuous influence of pronounced anthropogenic pollution. The predominant type is biomass burning smoke from deforestation fires, which led to the coining of the term "biomass burning season" (Freud et al., 2008). In addition, various urban and industrial emission sources in eastern and southern Brazil as well as southern Africa may also contribute by hard-to-define quantities (e.g., Andreae et al., 1994; Saturno et al., 2017a). The minimum in precipitation rates and, thus, in aerosol scavenging fosters the distribution of pollution aerosols over large areas by extending their atmospheric lifetime (see Fig. 2).

Figure 4 represents the dry-season counterpart of Fig. 3 and shows the corresponding time series for a characteristic dry-season period from 1 August until 30 September 2014. The BT clusters in Fig. 4a show that easterly and southeasterly BTs prevailed, since the ITCZ was located north of the ATTO site. The BT clusters which are most characteristic for the dry season approached the Amazon River delta from the South Atlantic and then followed the river in a westerly direction towards ATTO (red and orange clusters; see Fig. S1). These "dry-season river BTs" are the subject of a more detailed discussion in the case study in Sect. 3.7. For certain episodes, the wind swings further to southeasterly directions and brings air masses from inland directions (black, brown, and grey BT clusters; see Fig. S1). These "dry-season inland BTs" are further discussed in the case study in Sect. 3.6.

In contrast to the wet season, the accumulation mode clearly dominates the size distribution, which explains the increased CCN efficiencies, particularly at low S (Fig. 4c and i). The frequent "pulses" in the accumulation mode concentration can be attributed to (aged) biomass burning plumes, which impact the ATTO site episodically, typically for few days (see Freitas et al., 2005). The M_{BC_e}, $N_{CN,10}$, and c_{CO} levels are typical for dry-season conditions in the northeast Amazon Basin with $M_{BC_e} = 0.55 \pm 0.35\,\mu g\,m^{-3}$, $N_{CN,10} = 1520 \pm 780\,cm^{-3}$, and $c_{CO} = 140 \pm 50$ ppb (given as mean $\pm$ 1 SD for the time period in Fig. 4) (e.g., Rissler et al., 2004; Andreae et al., 2012, 2015; Artaxo et al., 2013; Saturno et al., 2017a).

The most obvious event in Fig. 4 is the advection of a strong BB plume from 17 to 23 August 2014, the highest pollution levels that were observed during the entire CCN measurement period. This event can be recognized by means of strong pulses in N_{Acc}, M_{BC_e}, and c_{CO} as well as a dip in $\kappa(S, D_a)$. The ACSM-derived organic-to-sulfate ratio confirms that the biomass burning pulse comprised a predominantly organic aerosol. In general, the measured $\kappa(S, D_a)$ levels respond inversely to the organic-to-sulfate ratio, confirming previous studies which stated that organic matter and sulfate constituents mostly define the aerosol's hygroscopicity in the Amazon (Roberts et al., 2002; Gunthe et al., 2009).

Table 1. Overview of conditions and corresponding time frames for detailed aerosol and CCN analysis. Note that time frames of different length were averaged for certain aerosol and CCN data products (i.e., size distributions, composition, CCN key parameters) depending on data availability.

Conditions		Time frames (UTC)	Specific remarks
Empirically pristine rain forest (PR) aerosol	All available PR periods	Defined in Sect. 2.7; filter time series available as separate data file	– For $N_{CN}(D)$, $N_{CCN}(S,D)$, $\kappa(S, D_a)$, CCN efficiency spectra (Fig. 6a and b): all available $PR_{BC \cap CO}$ episodes within CCN measurement period (Mar 2014–Feb 2015) were averaged.
	PR1	24 Apr 06:00–29 April 10:00 2014	– Episodes PR1, PR2, and PR3 highlighted in Fig. 3 and shown in detail in Fig. 5.
	PR2	4 May 23:00–8 May 10:00 2014	– For ACSM results (Table 3): all $PR_{BC \cap CO}$ episodes within time frame 1 Aug 2014 to 30 Sep 2016 were averaged.
	PR3	16 May 06:00–17 May 16:00 2014	
Long-range transport (LRT) aerosol (in wet season)	LRT	9 Apr 12:00–13 Apr 12:00 2014	– LRT time frame averaged for $N_{CN}(D)$, $N_{CCN}(S,D)$, $\kappa(S, D_a)$, CCN efficiency spectra (Fig. 6c and d). – LRT episode highlighted in Fig. 3 and shown in detail in Fig. 7.
	All available LRT episodes	See Moran-Zuloaga et al. (2017)	– For ACSM results (Table 3): all LRT episodes according to Moran-Zuloaga et al. (2017) within time frame 1 Aug 2014 to 30 Sep 2016 were averaged.
Biomass burning (BB) aerosol	BB	18 Aug 00:00–22 Aug 00:00 2014	– BB time frame averaged for $N_{CN}(D)$, $N_{CCN}(S,D)$, $\kappa(S, D_a)$, CCN efficiency spectrum (Fig. 6e and f), and ACSM results (Table 3). – BB episode highlighted in Fig. 4 and shown in detail in Fig. 8.
Mixed pollution (MPOL) aerosol (in dry season)	MPOL-BB MPOL-LRT	Entire period: 22 Sep 00:40–1 Oct 03:30 2014 (for details refer to Fig. 9)	– Subcategories MPOL-BB and MPOL-LRT during MPOL episode averaged independently for $N_{CN}(D)$, $N_{CCN}(S,D)$, $\kappa(S, D_a)$, CCN efficiency spectra in Fig. 6g, h and i, and ACSM averages (Table 3). – MPOL highlighted in Fig. 4 and shown in detail in Fig. 9.

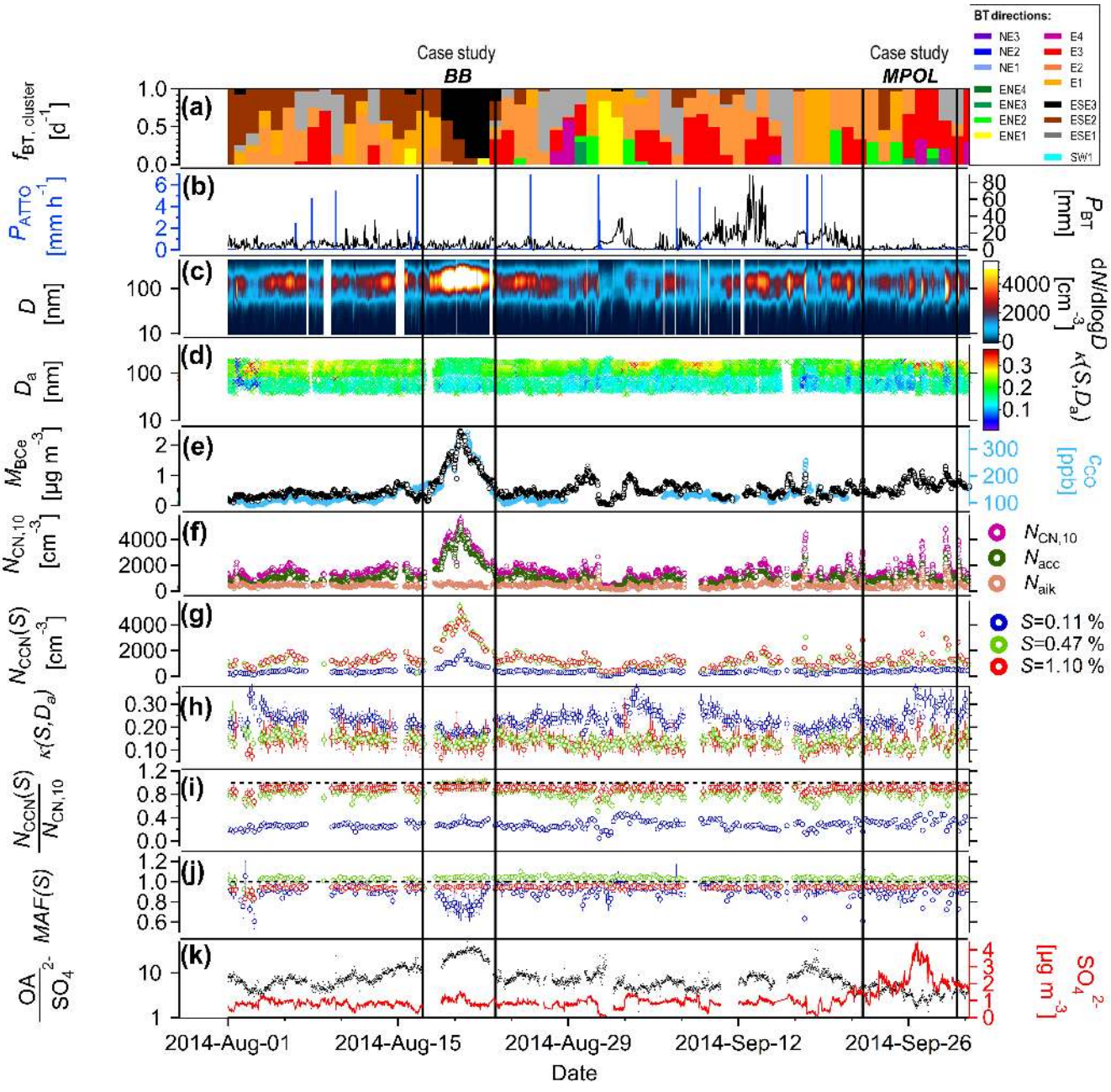

Figure 4. Overview plot illustrating selected meteorological, trace gas, aerosol, and CCN time series for representative dry-season conditions in the central Amazon. The shown time period from 1 August to 31 September covers the most polluted time frame throughout the entire CCN measurement period. Individual panels represent **(a)** daily frequency of occurrence of 15 different BT clusters, $f_{BT,cluster}$, with color code corresponding to Fig. S1; **(b)** precipitation rate (P_{ATTO}) measured locally at ATTO and cumulative precipitation from BT analysis (P_{BT}) as a measure for aerosol wet deposition; **(c)** SMPS-derived time series of number size distributions spanning nucleation, Aitken, and accumulation modes; **(d)** CCNC-derived time series of $\kappa(S, D_a)$ size distributions; **(e)** concentrations of biomass burning tracers, CO mole fraction (c_{CO}) and BC_e mass concentration (M_{BC_e}); **(f)** total number concentrations of the entire aerosol population ($N_{CN,10}$), Aitken mode particles (N_{Ait}), and accumulation mode particles (N_{acc}); **(g)** CCN concentrations, $N_{CCN}(S)$, for selected supersaturations S; **(h)** hygroscopicity parameter, $\kappa(S, D_a)$, for selected S; **(i)** CCN efficiencies, $N_{CCN}(S)/N_{CN,10}$, for selected S; **(j)** maximum activated fraction, MAF(S), for selected S; and **(k)** ACSM-derived sulfate mass concentration ($M_{sulfate}$) and organic-to-sulfate ratio (OA / SO_4^{2-}). All CCN data are provided at the original time resolution of about 4.5 h. Vertical lines highlight BB case study on biomass burning conditions for detailed analysis in Sect. 3.6 and MPOL case study on mixed pollution conditions for detailed analysis in Sect. 3.7.

The major biomass burning plume in August 2014 is the subject of the detailed case study BB in Sect. 3.6.

Beside this major biomass burning plume, several shorter pulses, which were supposedly also caused by upwind fires, were observed throughout the dry-season period, and their frequency of occurrence increased towards the end (i.e., after 12 September). Phenomenologically, the major and minor biomass burning plumes were similar as they exhibit peaks in N_{CN}, M_{BC_e}, and c_{CO} and simultaneous dips in $\kappa(S, D_a)$ and the organic-to-sulfate ratio. The second half of September comprised conditions with comparatively high sulfate concentrations and a sequence of short biomass burning plumes. This period is influenced by a mixture of different (pollution) aerosol populations from African long-range transport and regional South American sources. A detailed description of the case study MPOL can be found in Sect. 3.7.

Similar to the wet season, different $\kappa(S, D_a)$ levels for the Aitken and accumulation modes as well as comparably low $\kappa(S, D_a)$ variability over time ($\kappa_{Ait} = 0.14 \pm 0.03$ vs. $\kappa_{Acc} = 0.23 \pm 0.04$, covering the entire time period in Fig. 4d and h) were observed. The MAF(S) values tend to reach unity, except for MAF(0.11 %) under the influence of biomass burning smoke (i.e., for the smaller and major smoke plumes).

3.4 Case study PR on empirically pristine rain forest aerosols

Aerosol–cloud interactions remain the largest uncertainty in global climate models, and a better understanding of a preindustrial atmospheric state is essential to reduce this uncertainty (Carslaw et al., 2013; Seinfeld et al., 2016). As outlined in Sect. 2.7, the Amazonian wet season provides the rare chance to analyze episodes of very clean continental conditions, which are our best approximation of a pristine rain forest atmosphere. This case study extracts the characteristic aerosol and CCN properties during the identified PR periods. Figure 5 zooms into three selected episodes – called PR1, PR2, and PR3 as highlighted in Fig. 3 – and combines meteorological, aerosol, and CCN time series for a detailed analysis.

The meteorological parameters in Fig. 5a, b, and c illustrate typical wet-season conditions: (i) a rather high degree of cloudiness, which can be seen by means of the strong cloud-related dimming of the incoming shortwave radiation, SW_{in}; (ii) frequent local (P_{ATTO}) and regional (P_{TRMM}) rain events; (iii) a comparatively stable northeasterly wind direction, which is consistent with the BT analysis in Fig. 3; (iv) a rather constant wind speed, U, for most of the time, which got more vigorous during rain events; (v) high-relative-humidity (RH) conditions, being inversely related to SW_{in} and reaching saturation during the nights; and (vi) a characteristic time series of the equivalent potential temperature, θ_e, which tracked the daily onset of solar heating (see simultaneous increase of SW_{in} and θ_e) and further provides valuable information on vertical atmospheric mixing, particularly in connection with rain events. Specifically, sudden drops in θ_e indicate a downward transport of air masses from upper-tropospheric layers, which occurred frequently with the onset of strong rain (for more details see Wang et al., 2016).

The corresponding aerosol variability is shown as an aerosol number size distribution ($dN/d\log D$) contour plot in Fig. 5d. Under PR conditions we found a dominant Aitken mode and a comparatively weak accumulation mode, as reported previously (e.g., Andreae et al., 2015; Pöhlker et al., 2016). Moreover, the Aitken and accumulation modes reveal a patchy and discontinuous abundance with rather sudden concentration increases and drops. These observations can be explained by a combination of different effects and processes: first, the strong and persistent (mostly combustion-related) sources of accumulation mode aerosol particles, which are responsible for the continuous and dominant accumulation mode in the dry season, were absent.

Second, the frequent rain events acted as an efficient aerosol removal mechanism via aerosol rain-out (i.e., particle activation into cloud/rain droplets) and wash-out (i.e., particle collection by falling droplets below clouds). The wash-out efficiency is slightly higher ($\sim$ factor 1.5) for Aitken than accumulation mode particles (Wang et al., 2010; Zikova and Zdimal, 2016). In contrast, the rain-out efficiency, corresponding to CCN activation, is typically much higher for accumulation than Aitken mode particles (Pöhlker et al., 2016). Accordingly, the rain pulses strongly modulated the aerosol's abundance via sudden and efficient deposition, which is visible in Fig. 5d as characteristic "notches" in the aerosol contour plot. The notches represent the (removed) part of the aerosol size fraction that was activated as CCN into cloud droplets. Illustrative examples can be found during days with strong rain showers, such as 27 April, 5 May, and 6 May. Note that the "depth of the notches", corresponding to the smallest activated particles, could in principle be used to estimate the S levels during the corresponding events (Krüger et al., 2014). Further note in this context that, besides depletion of the accumulation relative to the Aitken mode, aerosol activation and cloud processing are also known to foster the opposite effect: the growth of Aitken mode particles into the accumulation mode via formation of aqueous-phase reaction products (i.e., sulfate and aqueous-phase SOA) in the cloud droplets, followed by droplet re-evaporation and deposition of the newly formed compounds onto the particles (e.g., Ervens, 2015; Farmer et al., 2015). During 7 May, cloud processing might have been responsible for the formation of a rather strong accumulation mode from an existing Aitken mode population.

As a third process, the Aitken mode population in the rain forest BL was frequently replenished by pulse-like appearance of particles with diameters < 50 nm. These events are supposed to be convection-related downward transport of air masses from an UT particle pool and the subsequent growth of the injected fine particles (Wang et al., 2016; Andreae

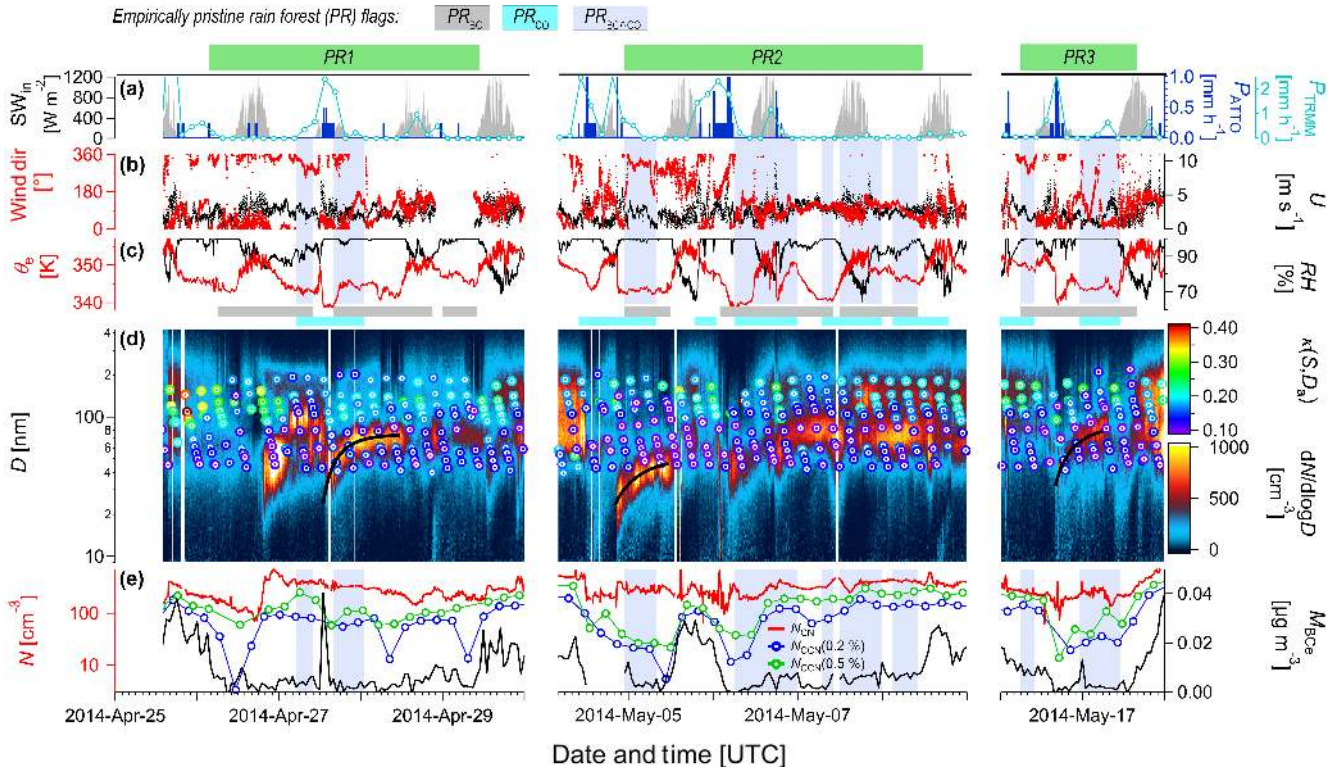

Figure 5. Selected meteorological, aerosol, and CCN time series from ATTO measurements for the empirically pristine rain forest (PR) case study periods PR1, PR2, and PR3 (see Fig. 3). **(a)** Incoming shortwave radiation, SW_{in}; precipitation rates from TRMM satellite mission, P_{TRMM}; and in situ measurements at ATTO, P_{ATTO}. **(b)** Wind direction and wind speed, U, at ATTO. **(c)** Equivalent potential temperature, θ_e, and relative humidity, RH, at ATTO. **(d)** Overlay of two data layers showing aerosol number size distribution contour plot, $dN/d\log D$, as well as color-coded markers, representing time series of $\kappa(S, D_a)$ size distributions. **(e)** CCN concentrations, $N_{CCN}(S)$, for two selected S levels; total aerosol number concentration, $N_{CN,10}$; and BC_e mass concentration, M_{BC_e}. Vertical shadings represent $PR_{BC\cap CO}$ periods according to the definition in Sect. 2.7.

et al., 2018). Remarkably, the combination of all these effects results in a comparatively constant total particle abundance, N_{CN}, across the rain showers, due to compensating effects of accumulation mode particle losses and simultaneous increases in Aitken mode abundance (see details in Wang et al., 2016). The convection-related downward transport of fine UT particles and their subsequent growth – presumably by the condensation of low-volatility vapors – is a characteristic feature of the Amazonian wet season. At least three pronounced examples for this process are included in the time frame of Fig. 5 (i.e., 27/28 April, 4/5 May, and 16/17 May). After their injection into the forest BL, the fine particles (initial diameters between 20 and 50 nm for the events in Fig. 5) reveal a "banana-like" growth into the Aitken mode size range ($\sim$ 70 nm) in the course of about 12–24 h. For the events in Fig. 5, we calculated an initial, and thus maximum, growth rate of 0.6 to 6 nm h^{-1}, which agrees well with the 1 to 6 nm h^{-1} reported by Kulmala et al. (2004) for tropical regions as well as the reported 5 nm h^{-1} in Zhou et al. (2002) for an Amazonian site. Note that these "Amazonian bananas" differ from the classical new-particle formation (NPF) events that have been reported for various continental sites (i.e., in northern hemispheric temperate regions) (Kulmala et al., 2004), since the number concentrations are lower by orders of magnitude and their nucleation and initial growth do not occur in the BL but in the UT (Ekman et al., 2008; Engstrom et al., 2008; Pöschl et al., 2010; Andreae et al., 2018). Accordingly, the UT particle population that is frequently injected into the BL is already aged to a certain extent and, thus, presumably reflects chemical processes different from the atmospheric chemistry in the BL. The physicochemical details of the UT nucleation and growth are still largely unknown and the subject of ongoing research (e.g., Andreae et al., 2018).

The CCN properties during PR conditions are represented by time series of $\kappa(S, D_a)$ size distributions (Fig. 5d) and $N_{CCN}(S)$ for two selected S (Fig. 5e). The temporal pattern of the $\kappa(S, D_a)$ size distributions, which provides indications of the aerosol particles' chemical composition, reflects the pattern of the underlying $dN/d\log D$ contour plot. Consistent with our observations in Part 1 (Pöhlker et al., 2016), the accumulation mode reveals higher $\kappa(S, D_a)$ levels than

the Aitken mode, likely due to chemical aging through cloud processing and a related increase in hygroscopicity (Farmer et al., 2015). The lowest $\kappa(S, D_a)$ levels were observed for the "Amazonian bananas" (see Fig. 5d). Both the accumulation and Aitken mode $\kappa(S, D_a)$ levels show a variability that tracks the Aitken and accumulation mode abundance. Note that $N_{CCN}(0.5\,\%)$ and particularly $N_{CCN}(0.2\,\%)$ show pronounced increases during periods with increased M_{BC_e} levels (e.g., 25 April, 5 May, and 17 May). This emphasizes the remarkable impact of diluted pollution on the CCN population in an aerosol-limited regime according to Reutter et al. (2009).

Figure 6a and b summarize the average aerosol and CCN key properties under PR conditions.[1] Figure 6a shows the characteristic average $N_{CN}(D)$ size distribution with a pronounced bimodal appearance, comprising a dominant Aitken mode ($D_{Ait} \approx 70$ nm, $N_{Ait} \approx 160\,cm^{-3}$) and a comparatively weak accumulation mode ($D_{acc} \approx 160$ nm, $N_{acc} \approx 90\,cm^{-3}$) (see Table 2). This bimodal shape is typical for clean Amazonian conditions as reported previously (e.g., Gunthe et al., 2009) and further resembles aerosol size distributions under marine background conditions (e.g., Atwood et al., 2017). The corresponding $N_{CCN}(S,D)$ size distributions for all S levels show that for $S < 0.3\,\%$ mostly accumulation mode particles were activated, whereas for $S > 0.3\,\%$ the Aitken mode particles also acted as CCN. Furthermore, Fig. 6a shows the average $\kappa(S, D_a)$ size dependence with a characteristic stepwise increase of $\kappa(S, D_a)$ towards larger D. The Aitken mode $\kappa(S, D_a)$ levels are rather low and sharply defined (mean $\pm$ SD: 0.12 ± 0.01), whereas the accumulation mode $\kappa(S, D_a)$ levels are slightly higher (0.18 ± 0.02). The results suggest that the Aitken mode particles, which are frequently injected into the BL via downward transport from the UT, are mostly comprised of organic matter. This observation agrees well with recent results showing that "the UT particles consist predominantly of organic material, with minor amounts of nitrate and very small fractions of sulfate" (Andreae et al., 2018). The hygroscopicity of organic material, κ_{org}, is typically assumed as ~ 0.10; however, κ_{org} can vary substantially (close to 0 up to 0.3) as a function of the organic material and its oxygen-to-carbon (O : C) ratio (Jimenez et al., 2009; Thalman et al., 2017). The $\kappa(S, D_a)$ levels of the accumulation mode similarly indicate the presence of predominantly organic particles, albeit with somewhat more inorganic constituents than in the Aitken mode. This is consistent with the corresponding ACSM results in Table 3, underlining that organic matter accounts for most of the mass (90 %), whereas nitrate (4 %) and sulfate (6 %) add only small contributions. Note that M_{NH_4}, M_{Cl}, and M_{BC_e} were below the detection limit for PR conditions and were omitted in the calculation of the mass fractions accordingly (see Sect. 2.1).[2] A predicted average hygroscopicity parameter, κ_p, of 0.16 ± 0.01 was calculated based on the ACSM results – excluding M_{NH_4}, M_{Cl}, and M_{BC_e} – and agrees with the measured value of $\kappa(0.11\,\%) = 0.18 \pm 0.05$ (Table 3).

Figure 6b displays the CCN efficiency spectrum for PR conditions, which can be regarded as the CCN signature of the corresponding aerosol population (for details refer to the Part 1 companion paper). The pronounced bimodal particle size distribution with its characteristic Hoppel minimum and the stepwise increase of $\kappa(S, D_a)$ (see Fig. 6a) result in a weak plateau at about $S = 0.4\,\%$, which required to apply a double-erf fit. For comparison, we also applied a single-erf fit. Expectedly, the double-erf fit is the better representation of the experimental data, although the single-erf fit also covers the data reasonably well, since the plateau is not particularly pronounced. However, a closer look reveals differences between the single- and double-erf fits for low and high S. For very low S ($< 0.1\,\%$), the double-erf fit indicates that the PR aerosol particles start acting as CCN only above about $S = 0.06\,\%$, which can probably be explained by the absence of suitable CCN in the size range of several hundred nanometers, which are indeed comparatively sparse under PR conditions according to Fig. 5. However, this size range was not covered directly by our CCN measurements, making it hard to draw conclusions. Since the double-erf fit describes the data more accurately than the single-erf fit, its extrapolation for $S > 1.1\,\%$ is likely more accurate and suggests that "full" activation ($\sim 90\,\%$) is reached at $S \approx 1.5\,\%$.

The CCN efficiency spectra represent a tool with which to visualize characteristic differences in the behavior of certain (contrasting) aerosol populations in cloud formation. Of particular relevance is the slope of the CCN efficiency spectra, $d(N_{CCN}(S)/N_{CN,10})/dS$, as the sensitivity of the activated CCN fraction of a given aerosol population within a given S range to changes in supersaturation, ΔS. Accordingly, high $d(N_{CCN}(S)/N_{CN,10})/dS$ slopes indicate a regime in which even a subtle ΔS has relatively strong effects on the $N_{CCN}(S)$ and, thus, N_d concentrations (assuming constant $N_{CN,10}$), whereas low $d(N_{CCN}(S)/N_{CN,10})/dS$ values indicate a regime that is characterized by more stable $N_{CCN}(S)$ and N_d concentrations, even upon large ΔS.

The CCN efficiency spectra can be linked to a concept introduced by Reutter et al. (2009), which classifies the sensitivity of N_d concentrations in response to changes in N_{CN} and w_b. This results in three distinct regimes: (i) an *aerosol-limited* regime, which is characterized by high S_{max} ($> 0.5\,\%$), a high w_b / N_{CN} ratio, high activated fractions

[1] The aerosol and CCN key properties are similar for all PR filters (i.e., PR_{BC}, PR_{CO}, $PR_{BC \cup CO}$, $PR_{BC \cap CO}$; see Sect. 2.7). For completeness, the $N_{CN}(D)$ and $\kappa(S, D_a)$ size distributions for all four PR filters are summarized in Fig. S5. For comparison, Fig. S6 shows $N_{CN}(D)$ size distributions after a classification by means of a statistical analysis of the total aerosol concentrations, which resemble the PR filter-based results. Furthermore, Fig. S7 shows the corresponding $N_{CN}(D)$ and $\kappa(S, D_a)$ size distributions filtered for the comparatively clean BT clusters NE1, NE2, and NE3.

[2] M_{BC_e} was per definition below the detection limit for PR conditions.

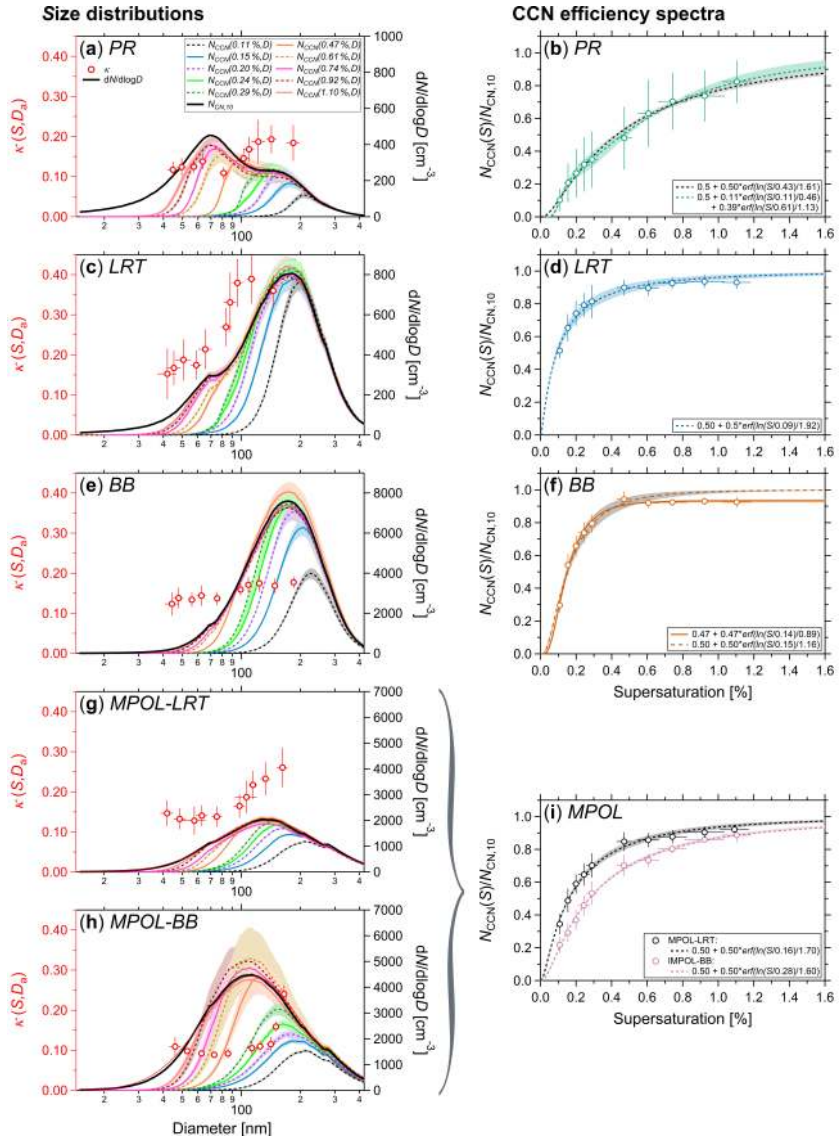

Figure 6. Overview of case study conditions for empirically pristine rain forest (PR), long-range transport of African aerosols (LRT), biomass burning (BB), and mixed pollution of African and Amazonian sources (MPOL), showing size dependence of hygroscopicity parameter ($\kappa(S, D_a)$), number size distributions of total aerosol particles ($N_{CN}(D)$), and number size distributions of cloud condensation nuclei ($N_{CCN}(S,D)$) at all 10 S levels ($S = 0.11$–$1.10\,\%$) (left side) as well as CCN efficiency spectra with erf fits (right side). For the size distributions (left), values of $\kappa(S, D_a)$ for every S level are plotted against their corresponding midpoint activation diameter, $D_a(S)$. For $\kappa(S, D_a)$, the error bars represent 1 SD. For $D_a(S)$, the experimentally derived error is shown. The standard errors of the number size distributions – $N_{CN}(D)$ and $N_{CCN}(S,D)$ – are indicated as shading of the individual lines. For the CCN efficiency spectra (right), $N_{CN,10}$ was chosen as a reference concentration. The experimental data were fitted with single- or double-erf fits dashed lines with shading as uncertainty of the fits. The error bars at the markers represent the measurement error in S and 1 SD in the $N_{CCN}(S)/N_{CN,10}$ dimension. The shading represents the uncertainty of the fits. An overview of the erf fits from all case study conditions and seasonal averages can be found in Fig. 11. The parameters of all erf fits are summarized in Table 4. Data for PR conditions in **(a)** and **(b)** represent averages of all $PR_{BC \cap CO}$ episodes during the entire CCN measurement period as defined in Sect. 2.7. For the PR CCN efficiency spectrum, the double-erf fit is the better representation, although the single-erf fit also works as a good approximation. Data for LRT conditions, shown in **(c)** and **(d)**, represent the LRT3 period as shown in Fig. 3. A single-erf fit describes the experimental data accurately. Data for BB conditions, shown in **(c)** and **(d)**, represent the time period in August 2014 as shown in Fig. 4. For the BB case, the experimental data have been fitted with a single-erf fit with two modifications: (i) the "default" fit with predefined variable $a_1 = 1$ as utilized for all other case studies tends to overestimate $N_{CCN}(S)/N_{CN,10}$ at high S; (ii) a corresponding fit with a free variable a_1 describes the experimental data more accurately. Data for MPOL conditions were separated into a MPOL-LRT case **(g)**, representing sulfate-rich African aerosols, and a MPOL-BB case **(h)**, representing plumes from close-by fires. MPOL CCN efficiency spectra are combined in **(i)** including single-erf fits. All fit parameters of the erf fits shown here are summarized in Table 4. The colors of the CCN efficiency spectra were chosen according to Wong (2011).

Table 2. Properties (position, x_0; integral number concentration, N_{CN}; width, σ) of Aitken and accumulation modes from single or double lognormal fits of the total particle size distribution. Values are given as means of the case study periods, whereas corresponding seasonally averaged results can be found in the Part 1 study. The errors represent the uncertainty of the fit parameters. No meaningful double lognormal fit was obtained for the monomodal MPOL case – thus, a single lognormal fit was conducted to describe the properties of the main peak. For the cases $PR_{BC\cap CO}$ and LRT with clearly resolved bimodal size distributions, values for the position of the Hoppel minimum, D_H, as the intersection of fitted and normalized modes as well as estimated average peak supersaturation in cloud, $S_{cloud}(D_H, \kappa)$, according to Krüger et al. (2014) and Part 1 study are listed. The error in $S_{cloud}(D_H, \kappa)$ is the experimentally derived error in S. Analogous information for the PR_{BC}, PR_{CO}, and $PR_{BC\cup CO}$ filters can be found in Table S1.

Conditions		Mode or size range	N_{CN} (cm^{-3})	κ	x_0 (nm)	σ	R^2	D_H (nm)	$S_{cloud}(D_H,\kappa)$ (%)
Empirically pristine rain forest (PR) aerosol ($PR_{BC\cap CO}$ filter)[a]		Aitken accumulation	162 ± 4 86 ± 8	0.12 ± 0.01 0.18 ± 0.01	69 ± 2 157 ± 1	0.46 ± 0.01 0.44 ± 0.01	0.99	103 ± 2	0.29 ± 0.01
Long-range-transport (LRT) aerosol		Aitken accumulation	125 ± 12 313 ± 11	0.18 ± 0.02 0.35 ± 0.04	79 ± 3 179 ± 2	0.60 ± 0.03 0.52 ± 0.01	0.99	118 ± 2	0.15 ± 0.01
Biomass burning (BB) aerosol		Aitken accumulation	140 ± 29 3439 ± 39	0.14 ± 0.01 0.17 ± 0.02	70 ± 1 167 ± 1	0.20[b] 0.58 ± 0.01	0.99	–	–
Mixed-pollution (MPOL) aerosol	MPOL-LRT	<100 nm >100 nm	1272 ± 27	0.14 ± 0.01 0.22 ± 0.03	135 ± 5	0.85 ± 0.01	0.99	–	–
	MPOL-BB	<150 nm >150 nm	2764 ± 84	0.10 ± 0.01 0.20 ± 0.04	113 ± 1	0.81 ± 0.01	0.99	–	–

[a] Double lognormal fits for the PR cases were limited to size range 50 to 350 nm since presence of particles in nucleation mode size range (<50 nm) interferes with fit of Aitken mode. [b] Width of Aitken mode in double lognormal fit of BB case was predefined to ensure meaningful convergence of fit.

N_d / N_{CN}, and a linear relationship between N_{CN} and N_d; (ii) an *updraft-limited* regime, which is characterized by rather low S_{max} (<0.2 %), a low w_b / N_{CN} ratio, low activated fractions N_d / N_{CN}, and a linear relationship between w_b and N_d; and (iii) a *transitional* regime with intermediate states and nonlinear dependencies of N_d on N_{CN} and w_b. Note that the concept of Reutter et al. has been developed for the conditions of pyro-convective clouds and, thus, represents an extreme case, which has to be kept in mind in the subsequent comparison with the CCN efficiency spectra.[3] Pöschl et al. (2010) applied the concept of Reutter et al. (2009) to wet-season rain forest conditions. Based on Reutter et al. and Pöschl et al., PR conditions with the associated low aerosol concentrations ($N_{CN,10} \approx 260\,cm^{-3}$, Table 4) can be characterized as aerosol-limited, due to the overall low abundance of potential CCN. However, the CCN efficiency spectrum in Fig. 6b suggests that the PR aerosol population also has a certain sensitivity to w_b, since changes in updraft velocity Δw_b – and the associated ΔS (even for $S > 1$ %) – strongly modulate the activated fraction, $N_{CCN}(S)/N_{CN,10}$. In this sense, the PR CCN efficiency spectrum has a very characteristic shape and differs clearly from the other conditions, as it keeps increasing over a wide S range with a somewhat larger slope for $S < 0.3$ % and a slightly decreasing slope for $S > 0.3$ %.[4] Accordingly, the PR case appears to be aerosol- *and* updraft-sensitive, which makes the corresponding aerosol–cloud interactions highly dynamic. For more quantitative insights, modeling runs according to Reutter et al. based on the characteristic PR bimodal $N_{CN}(D)$ size distribution in Fig. 6a as well as adjusted N_{CN} and w_b ranges are required.

3.5 Case study LRT on Saharan dust, African smoke, and Atlantic marine aerosols

The African continent is of significant importance for the Amazonian atmospheric composition as it represents a major source of desert dust and pollution aerosols (e.g., Swap et al., 1992; Andreae et al., 1994; Yu et al., 2015; Rizzolo et al., 2017). A systematic overview of the properties and relevance of LRT plume arrivals in the ATTO region during the Amazonian wet season can be found in Moran-Zuloaga et al. (2017). Furthermore, a general characterization of the CCN population's response to LRT conditions during the wet season can be found in our Part 1 paper (Pöhlker et al., 2016).

[3] The cloud parcel modeling by Reutter et al. (2009) was conducted for the specific case of pyro-convective conditions, developing over strong fires. Accordingly, a typical (monomodal) biomass burning aerosol size distribution with an accumulation mode maximum at 120 nm was used. In this sense, the study is bound to rather specific and extreme conditions. However, Reutter et al. state that the "key features of the three regimes of CCN activation … are not specific for young biomass burning aerosols and pyro-convective conditions but likely to apply also for other types of aerosols and meteorological conditions".

[4] For completeness, the CCN efficiency spectra for all four PR filters according Sect. 2.7 (i.e., PR_{BC}, PR_{CO}, $PR_{BC\cup CO}$, $PR_{BC\cap CO}$) are shown in the comparison Fig. S8.

Table 3. Aerosol chemical composition from ACSM measurements at ATTO for characteristic conditions and seasons. ACSM data were available for time period from 1 August 2014 to 30 September 2016, and the averaged values are shown as mean ± SE (SE was rounded up if SE < 0.01). Mass fractions were calculated as outlined in Sect. 2.1. The shown ACSM 3σ detection limits for 30 min averaging time were obtained from Ng et al. (2011). The MAAP-based M_{BC_e} detection limits are specified in Sect. 2.7. Note that M_{NH_4}, M_{Cl}, and M_{BC_e} ranged below the instrument detection limit in certain cases, which makes the corresponding results unreliable. The predicted average aerosol hygroscopicity parameter, κ_p, was calculated according to the Part 1 study (Pöhlker et al., 2016) and is shown as mean ± SE. The $\kappa(0.10\,\%)$ results are shown with the experimentally derived error. Analogous information for the PR_{BC}, PR_{CO}, and $PR_{BC\cup CO}$ filters can be found in Table S2.

Conditions and seasons	Mass concentrations $M_{species}$ ($\mu g\,m^{-3}$) (*Mass fraction (%)*)						OA / SO_4^{2-}	κ_p	$\kappa(0.10\,\%)$
	OA	NO_3^-	NH_4^+	SO_4^{2-}	Cl	BC_e			
Empirically pristine rain forest (PR) aerosol ($PR_{BC\cap CO}$ filter)	0.64 ± 0.02 *(90)**	0.03 ± 0.01 *(4)**	0.17 ± 0.01[a] (–)*	0.04 ± 0.01 *(6)**	$< (0.01 \pm 0.01)$[a] (–)*	$< (0.01 \pm 0.01)$[a] (–)*	~ 53	0.16 ± 0.01*	0.18 ± 0.05
Long-range transport (LRT) aerosol	1.81 ± 0.04 *(67)*	0.08 ± 0.01 *(3)*	0.30 ± 0.01 *(11)*	0.25 ± 0.01 *(9)*	0.04 ± 0.01 *(1)*	0.21 ± 0.01 *(8)*	~ 24	0.24 ± 0.01	0.35 ± 0.04
Biomass burning (BB) aerosol	21.14 ± 0.50 *(88)*	0.55 ± 0.02 *(2)*	0.58 ± 0.02 *(2)*	0.82 ± 0.02 *(3)*	0.03 ± 0.01 *(0)*	0.89 ± 0.03 *(4)*	~ 26	0.15 ± 0.01	0.18 ± 0.01
Mixed-pollution (MPOL) aerosol — MPOL-LRT	5.50 ± 0.06 *(65)*	0.22 ± 0.01 *(3)*	0.54 ± 0.01 *(6)*	1.75 ± 0.03 *(21)*	0.03 ± 0.01 *(0)*	0.37 ± 0.01 *(4)*	~ 3	0.28 ± 0.01	0.26 ± 0.05
Mixed-pollution (MPOL) aerosol — MPOL-BB	7.88 ± 0.18 *(68)*	0.36 ± 0.03 *(3)*	0.68 ± 0.03 *(6)*	2.03 ± 0.08 *(18)*	0.05 ± 0.01 *(0)*	0.57 ± 0.02 *(5)*	~ 4	0.26 ± 0.01	0.24 ± 0.02
Wet season (Feb–May)	1.02 ± 0.01 *(78)**	0.05 ± 0.01 *(4)**	0.20 ± 0.03[a] (–)*	0.14 ± 0.01 *(11)**	0.02 ± 0.01 *(1)**	0.07 ± 0.01 *(5)**	~ 23	0.19 ± 0.01*	0.21 ± 0.05
Transition periods (Jun/Jul & Dec/Jan)	3.26 ± 0.04 *(77)*	0.11 ± 0.01 *(3)*	0.32 ± 0.01 *(7)*	0.32 ± 0.01 *(8)*	0.02 ± 0.01 *(1)*	0.20 ± 0.01 *(5)*	~ 21	0.21 ± 0.01	0.24 ± 0.05
Dry season (Aug–Nov)	5.86 ± 0.05 *(79)*	0.19 ± 0.01 *(3)*	0.33 ± 0.01 *(5)*	0.64 ± 0.01 *(9)*	0.02 ± 0.01 *(0)*	0.34 ± 0.01 *(5)*	~ 11	0.18 ± 0.01	0.21 ± 0.04
Detection limits of ACSM and MAAP	0.15	0.01	0.28	0.02	0.01	0.01	–	–	–

[a] Here, the measured $M_{species}$ ranged below the instrument detection limits, and the shown values are questionable. In these cases (i.e., $PR_{BC\cap CO}$ and wet-season average), mass fractions and κ_p were calculated by omitting the corresponding $M_{species}$ as outlined in Sect. 2.1. The corresponding mass fractions and κ_p are marked by *.

Table 4. Gaussian error function (erf) fit parameters describing CCN efficiency spectra, $N_{CCN}(S)/N_{CN,10}$ vs. S, as model input data representing (i) $PR_{BC \cap CO}$, LRT, BB, and MPOL conditions according to present work, (ii) seasonal averages from the Part 1 companion paper (Pöhlker et al., 2016), and (iii) CCN efficiency spectra adapted from Roberts et al. (2001) and Andreae et al. (2004). A reference concentration of $N_{CN,10}$ has been used in all cases. N_{CN} is shown as mean ± SE. The errors in S_{mode} and w_{mode} represent the uncertainty of the fit parameters (see Sect. 2.2). All CCN efficiency spectra are plotted in Fig. 11 for comparison. Analogous information for the PR_{BC}, PR_{CO}, and $PR_{BC \cup CO}$ filters can be found in Table S3.

Conditions and seasons	N_{CN} (cm^{-3})	erf fit	Mode	a_{mode}	S_{mode} (%)	w_{mode}	R^2	Comment
Empirically pristine rain forest (PR) aerosol ($PR_{BC \cap CO}$ filter)	260 ± 3	Single	1	1	0.43 ± 0.01	1.61 ± 0.07	0.99	
		Double	1	1	0.11 ± 0.01	0.46 ± 0.30	0.99	
			2	0.21 ± 0.09	0.61 ± 0.08	1.13 ± 0.20		
Long-range transport (LRT) aerosol	439 ± 3	Single	1	1	0.09 ± 0.01	1.92 ± 0.15	0.97	Fit parameters for CCN efficiency spectra representing
Biomass burning (BB) aerosol	3584 ± 28	Single	1	1	0.15 ± 0.01	1.15 ± 0.13	0.96	conditions defined in present work
			1	0.93 ± 0.01	0.14 ± 0.01	0.89 ± 0.06	0.99	
Mixed pollution MPOL-LRT	1277 ± 6	Single	1	1	0.16 ± 0.01	1.70 ± 0.08	0.99	
(MPOL) aerosol MPOL-BB	2777 ± 38	Single	1	1	0.28 ± 0.01	1.60 ± 0.04	0.99	
Wet season	323 ± 2	Single	1	1	0.35 ± 0.01	1.80 ± 0.06	0.99	
LRT season	426 ± 3	Single	1	1	0.22 ± 0.01	2.39 ± 0.10	0.98	Fit parameters for seasonal CCN efficiency spectra
Transitions periods	943 ± 4	Single	1	1	0.28 ± 0.01	1.70 ± 0.05	0.99	from Part 1 study (Pöhlker et al., 2016)
Dry season	1528 ± 5	Single	1	1	0.18 ± 0.01	1.57 ± 0.11	0.98	
"Cloud-processed smoke" conditions	2000–8000	Single	1	1	0.47 ± 0.02	1.64 ± 0.15	0.97	Fit parameters for CCN efficiency spectra for biomass
"Fresh smoke" conditions	2000–8000	Single	1	1	1.00 ± 0.05	1.56 ± 0.12	0.98	burning smoke conditions from Andreae et al. (2004)
Wet-season period (Mar/Apr 1998)	390 ± 250	Single	1	1	0.62 ± 0.02	1.46 ± 0.07	0.99	Fit parameters for CCN efficiency spectra representing wet-season period from Roberts et al. (2001)

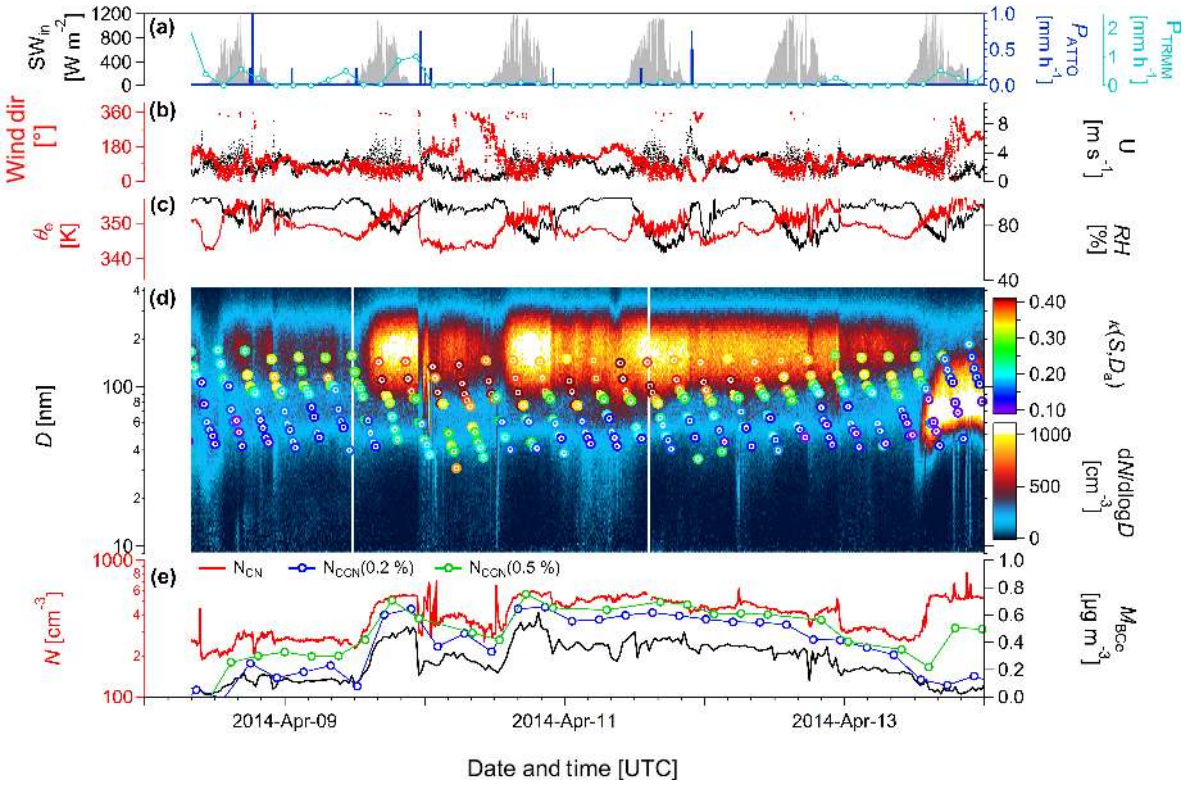

Figure 7. Selected meteorological, aerosol, and CCN time series from ATTO measurements for the long-range-transport (LRT) study period (see Fig. 3). **(a)** Incoming shortwave radiation, SW_{in}; precipitation rates from TRMM satellite mission, P_{TRMM}; and in situ measurements at ATTO, P_{ATTO}. **(b)** Wind direction and wind speed, U, at ATTO. **(c)** Equivalent potential temperature, θ_e, and relative humidity, RH, at ATTO. **(d)** Overlay of two data layers showing aerosol number size distribution contour plot, $dN/d\log D$, as well as color-coded markers, representing time series of $\kappa(S, D_a)$ size distributions. **(e)** CCN concentrations, $N_{CCN}(S)$, for two selected S levels; total aerosol number concentration, $N_{CN,10}$; and BC_e mass concentration, M_{BC_e}.

Based on these previous studies, the present paper analyzes the characteristic impact of LRT plumes on the wet-season CCN population in detail.

The characteristic impact of LRT plumes on the aerosol and CCN data can already be seen in Fig. 3. For a detailed analysis, the strongest LRT episode in Fig. 3 has been chosen and is represented in Fig. 7 by selected meteorological, aerosol, and CCN time series. Note that the advected dust plumes typically cause clear increases in both the coarse mode, which plays a secondary role here, and the accumulation mode, which explains their relevance for the CCN variability (Moran-Zuloaga et al., 2017). The LRT influence is visible in Fig. 7 by means of increases in M_{BC_e} (due to the LRT plume's smoke component), in the accumulation mode abundance in the $dN/d\log D$ contour plot, in the concentrations N_{CN} and $N_{CCN}(S)$, and in $\kappa(S, D_a)$.

The plume's influence on the ATTO site lasted for about 4 days, with its onset on 9 April ∼ 12:00 and its end on 13 April ∼ 12:00, which is in good agreement with the corresponding remote-sensing data in Moran-Zuloaga et al. (2017). During these 4 days, meteorology determined the variability of the LRT aerosol in the rain forest BL via air mass advection (i.e., wind speed and direction), rain-related scavenging (i.e., P_{ATTO} and P_{TRMM}), and convective mixing (represented by SW_{in} as a proxy). Throughout the LRT period, the dominant wind direction was mostly NE to E, which is characteristic for wet-season conditions (compare Fig. 3). Note that the BTs arriving from the NE are particularly prone to bringing dust-laden air into the ATTO region (Moran-Zuloaga et al., 2017). Furthermore, only few (major) rain events and related aerosol scavenging occurred during this time, which is a further prerequisite for efficient LRT transport. The arrival of the LRT plume during afternoon hours of 9 April occurred via convective downward mixing of the aerosol into the forest BL (see simultaneous increases in SW_{in}, θ_e, and the accumulation mode in $dN/d\log D$), and its influence lasted until 13 April, when the concentration time series decreased gradually. Note that the advected LRT plumes are transported into the ATTO region as compact and stratified aerosol layers up to altitudes of 2–3 km (Moran-Zuloaga et al., 2017). Aerosol concentrations were highest during the afternoon hours on 9, 10, and 11 April, when convection (see SW_{in}) is most efficient in mixing the aerosols downward into the BL. Furthermore, a sudden rain-related air mass change, lasting for

about 12 h (see wind direction and θ_e changes) at the end of 9 April/beginning of 10 April, was associated with a simultaneous drop in LRT aerosol concentrations. The CCN population responded noticeably to the injection of the LRT event, which can be seen in $N_{CCN}(S)$, $N_{CCN}(S)/N_{CN,10}$, and $\kappa(S, D_a)$ in Fig. 3. Figure 7 displays the $N_{CCN}(0.2\,\%)$ and $N_{CCN}(0.5\,\%)$ time series, which show a 2- to 3-fold increase upon LRT aerosol intrusion. Moreover, the $\kappa(S, D_a)$ data can be used as an indirect measure for the aerosol chemical composition, reflecting the average ratio of organic to inorganic constituents in the particles. In Fig. 7d, the occurrence of elevated $\kappa(S, D_a)$ levels coincides with the variability in $dN/d\log D$. For this particular event, κ_{Acc} increased from ~ 0.3 to ~ 0.4, whereas κ_{Ait} increased from ~ 0.15 to ~ 0.25.

Figure 6c summarizes the characteristic $N_{CN}(D)$ and $N_{CCN}(S,D)$ size distributions as well as the size dependence of $\kappa(S, D_a)$ during LRT influence. In general, the comparison of Fig. 6a and c contrasts the characteristic LRT vs. PR conditions and emphasizes that the intrusion of African LRT plumes into the wet-season BL has significant influence on the aerosol and CCN populations. Specifically, the accumulation mode under LRT conditions ($D_{acc} \approx 180$ nm, $N_{acc} \approx 300\,cm^{-3}$) is about 5× enhanced in comparison to the PR episodes. The Aitken mode ($D_{Ait} \approx 80$ nm, $N_{Ait} \approx 120\,cm^{-3}$) shows comparable absolute strength to that under PR conditions (see Table 2) but appears in the LRT $N_{CN}(D)$ distribution only as a shoulder. The $N_{CCN}(S,D)$ size distributions show that supersaturations $S \leq 0.3\,\%$ activate particles mostly in the accumulation mode range, whereas $S > 0.3\,\%$ starts activating the Aitken mode population. The $\kappa(S, D_a)$ size distribution shows κ_{Acc} reaching rather high levels up to 0.40 ($\kappa_{Acc} = 0.35 \pm 0.04$) and κ_{Ait} with values up to 0.2 ($\kappa_{Ait} = 0.18 \pm 0.02$). In comparison to the PR conditions, κ_{Acc} was clearly enhanced due to the presence of aged, internally mixed, and salt-rich particles (see discussion in subsequent section). In contrast, the κ_{Ait} levels were only slightly higher than during the PR periods, probably due to a broader accumulation mode base, which reached into the Aitken mode range. Note that the relative increase in $\kappa(S, D_a)$ for the contrasting LRT and PR conditions is large enough to exert an influence on the CCN population, which is an exceptional case throughout the Amazonian seasons, since the $\kappa(S, D_a)$ levels for most of the year vary within a rather narrow range (0.1 to 0.2) (see Part 1 paper).

The African LRT plumes that frequently impact the Amazon Basin during the wet season comprise a complex mixture of different aerosols components, including (i) a fraction of Saharan dust (mostly > 1 µm), (ii) biomass burning aerosols from fires in West Africa (mostly in the accumulation mode), and (iii) marine aerosols from the plume's transatlantic passage (in coarse and accumulation modes) (Andreae et al., 1986; Talbot et al., 1990; Swap et al., 1992; Weinzierl et al., 2017). Note that the African fires in West Africa are to a large extent agriculture-related and, thus, man-made (e.g., Barbosa et al., 1999; Capes et al., 2008). Fresh soot and uncoated dust particles typically have low hygroscopicities, whereas sea salt particles (i.e., NaCl and sulfates) represent comparatively efficient CCN. The LRT plumes make a rather long atmospheric journey – about 10 days according to Gläser et al. (2015) – which is associated with strong atmospheric processing and typically results in complex internally mixed particles (see Andreae et al., 1986). The resulting mixtures of dust and salt as well as coated soot particles, as commonly found in the dust plumes, readily act as CCN at realistic S levels (< 1 %) (Andreae and Rosenfeld, 2008).

Table 3 summarizes the ACSM results on aerosol chemical composition during LRT influence.[5] Note that the ACSM only measures the non-refractory fraction of the particle mass and, thus, does not detect a large fractions of the dust and salt constituents. During LRT conditions and with respect to the non-refractory part, organic mass dominated the particle composition (67 %), with minor nitrate contributions (3 %) and larger fractions of ammonium (11 %) and sulfate (9 %). Furthermore, a slight sea-salt-related increase in detected chloride mass (1 %) relative to the PR state was observed. Based on the ACSM results, a predicted κ_p of 0.24 ± 0.01 was obtained, which agrees reasonably well with the measured hygroscopicity level, $\kappa(0.11\,\%) = 0.35 \pm 0.04$. Accordingly, the observed elevated fractions of sulfate and ammonium were responsible for part of the increase in $\kappa(S, D_a)$. The remaining difference between κ_p and $\kappa(0.11\,\%)$ can likely be explained by further refractory inorganics that were not covered by the ACSM. As an illustration of the complex mixing state of the African LRT aerosol population, Figs. S10 and S11 provide selected SEM-EDX data from a characteristic LRT aerosol sample. Note that these results merely serve as a qualitative example here, whereas a quantitative microspectroscopic analysis of LRT samples is the subject of ongoing work. The observed particles' morphology underlines the influence of atmospheric processing and shows a high degree of internal mixing. Chemically, the EDX maps show dust particles, sulfate salts, and a rather large abundance of NaCl particles.

Figure 6d displays the characteristic CCN efficiency spectrum for the LRT conditions, which – expectedly – shows a rather steep increase at low S due to two effects pointing in the same direction: an enhanced accumulation mode and the presence of rather "good" CCN with comparatively high $\kappa(S, D_a)$ levels. This large initial slope corresponds to a very small value for the characteristic variable $S_1 = 0.09\,\%$, which shows that, at comparatively low S (lowest S_1 among all analyzed conditions), 50 % of the aerosol population were al-

[5] ACSM data were available from August 2014 to September 2016. Accordingly, the ACSM time frame does not cover the highlighted LRT event, which is discussed in detail in this work. Instead, we analyzed the ACSM data for 12 comparable LRT episodes in 2015 and 2016 according to Moran-Zuloaga et al. (2017) (see also Table 1).

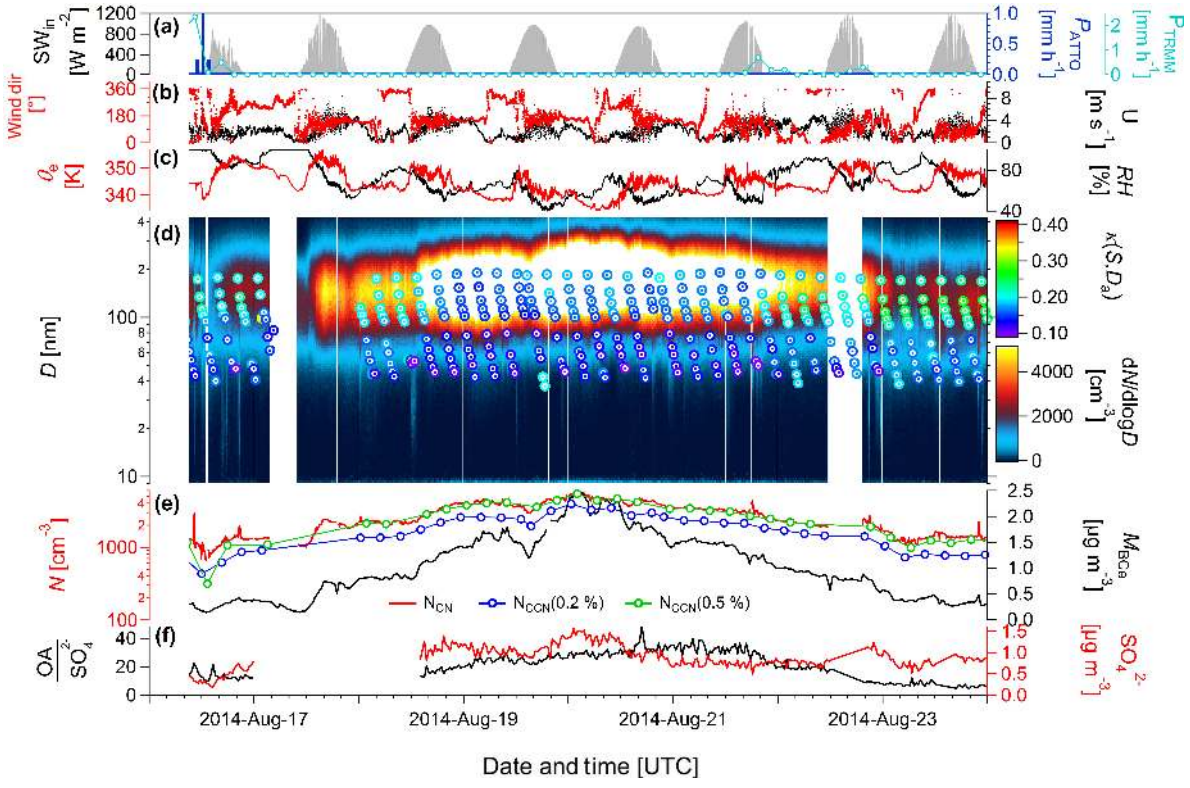

Figure 8. Selected meteorological, aerosol, and CCN time series from ATTO measurements for the biomass burning case study period, BB (see Fig. 4). **(a)** Incoming shortwave radiation, SW_{in}; precipitation rates from TRMM satellite mission, P_{TRMM}; and in situ measurements at the ATTO site, P_{ATTO}. **(b)** Wind direction and wind speed, U, at ATTO. **(c)** Equivalent potential temperature, θ_e, and relative humidity, RH, at ATTO. **(d)** Overlay of two data layers showing aerosol number size distribution contour plot, $dN/d\log D$, as well as color-coded markers, representing time series of $\kappa(S, D_a)$ size distributions. **(e)** CCN concentrations, $N_{CCN}(S)$, for two selected S levels; total aerosol number concentration, $N_{CN,10}$; and BC_e mass concentration, M_{BC_e}. **(f)** ACSM-derived sulfate mass concentrations and organic-to-sulfate mass ratio.

ready activated as CCN (Table 4). At S levels around 0.3 %, ~ 80 % of the aerosols acted as CCN; "full" activation (90 %) was reached at just $S \approx 0.5$ %. At higher S (i.e., > 0.9 %) the efficiency spectrum approaches unity. This is in stark contrast to the PR CCN efficiency spectrum in Fig. 6b, where 50 % of the particles were activated at significantly higher S around 0.5 %, whereas full activation (90 %) was reached at high S around 1.5 %. Thus, the LRT episodes show a pronounced sensitivity to ΔS only in the low-S regime, in contrast to the PR case with a sensitivity to ΔS spanning across a wide S range. With the characteristic shape of the CCN efficiency spectrum (i.e., rather strong accumulation mode) and the rather low aerosol concentrations ($N_{CN,10} \approx 440\,cm^{-3}$, Table 4), the LRT conditions are located at the border between aerosol-limited and transitional regimes (compare Reutter et al., 2009; Pöschl et al., 2010).

3.6 Case study BB on aged biomass burning smoke

During the dry season, the ATTO site is frequently influenced by smoke from biomass burning (BB) activities in different regions of the Amazon forest (Freitas et al., 2005; Andreae et al., 2012, 2015; C. Pöhlker et al., 2018). As a characteristic example, the case study BB focuses on the strong biomass burning plume that was observed at the ATTO site in the middle of August 2014. During this event, pollution aerosol and trace gas concentrations reached their annual maxima, with $N_{CN,10}$ peaking at 5000 cm^{-3}, c_{CO} peaking at 350 ppb, and M_{BC_e} reaching up to 2.5 µg m^{-3}, as shown in Fig. 4. Selected meteorological, aerosol, and CCN time series of the event are shown in Fig. 8. This case study provides the opportunity to analyze the CCN properties of aged smoke from a rather defined large-scale BB plume in the Amazon region.

Figure 8 shows that the influence of the BB smoke plume on the ATTO site lasted for about 6 days (18 to 22 August) with a gradual onset and decay. In terms of meteorology, this period was characterized by mostly cloud-free conditions (see SW_{in}) without precipitation, comparatively low RH levels, and some variability in wind direction. Note that, during the presence of this major smoke plume, atmospheric dimming in the ATTO region could be recognized (i.e., compare SW_{in} maxima for the seven consecutive days).

The signature of the smoke aerosol particles can very clearly be seen in the $dN/d\log D$ contour plot, N_{CN}, as well as M_{BC_e}. In terms of particle size, the pronounced increase mostly occurred in the accumulation mode, which appears to be comparatively broad for this specific event. The CCN concentrations – e.g., $N_{CCN}(0.2\,\%)$ and $N_{CCN}(0.5\,\%)$ – track the relative increase in total aerosol abundance and show a 4- to 5-fold increase as well. At the same time, the presence of the pyrogenic aerosols correspond to a clear drop in aerosol hygroscopicity in both the Aitken ($\Delta\kappa_{Ait} \approx -0.05$) and accumulation modes ($\Delta\kappa_{Acc} \approx -0.1$), relative to the conditions before and after the major BB plume (see overlay of $\kappa(S, D_a)$ size distributions and the $dN/d\log D$ contour plot in Fig. 8d). This drop in $\kappa(S, D_a)$ is associated with a high organic-to-sulfate, OA / SO_4^{2-}, ratio (Fig. 8f), reflecting the dominant role of organic constituents in biomass burning particles as documented in previous studies (Fuzzi et al., 2007; Artaxo et al., 2013; Lathem et al., 2013).

Geographically, the location of the fires and, thus, the origin of the strong biomass burning plume could be found by means of a combination of BTs and satellite data products as shown in Fig. S12 (Draxler and Hess, 1998; Acker and Leptoukh, 2007; Justice et al., 2011). The strong pollution at the ATTO site resulted from the presence of intense fires in the southern Amazon and a temporary "swing" of the BT track over the fire locations. During the dry season, the BTs mostly belong to the E and ESE clusters (see Figs. S1 and 4). For the period before and after the biomass burning plume, the BT track follows a "coastal path" and enters the continent in the region of the Amazon River delta (about 0° N 50° W). Subsequently, the air masses "follow" the Amazon River in westerly directions to the ATTO site. During the peak period of the BB event the BTs deviate from the coastal path and follow an "inland path" across the southeast of Brazil (see Figs. S12a and 4). At about 7° S and 55° W, the BTs intersect a region with strong fire activities, which are clearly visible in satellite products such as NO_2 total column measurements. These fires are localized along the Cuiabá–Santarém highway (BR-163). This highway corridor is known as a region of intense logging and burning of primary forest and its conversion to cattle pasture (Nepstad et al., 2002; Fearnside, 2007; C. Pöhlker et al., 2018). The transport time of the smoke from the fires to the ATTO site is about 2–3 days (given by the BTs), which provides a reference for the residence time and aging of the aerosol particles in the atmosphere. The satellite image in Fig. S12b shows the smoke plume that originated in the BR-163 region and traveled northwestwards. It clearly impacts the area around Manaus and the ATTO site precisely during the "event days" in August.

For a further characterization of the BB case study, we calculated a ratio of excess $N_{CN,10}$ to excess c_{CO} ($\Delta N_{CN,10} / \Delta c_{CO}$) for the event of $17.9 \pm 0.7\,cm^{-3}\,ppb^{-1}$ (see Fig. S13a), which agrees well with the typical range for a variety of vegetation fires ($30 \pm 15\,cm^{-3}\,ppb^{-1}$), in contrast to much higher $\Delta N_{CN,10} / \Delta c_{CO}$ levels for urban (100–300 $cm^{-3}\,ppb^{-1}$) and power plant emissions (up to $900\,cm^{-3}\,ppb^{-1}$) (Janhäll et al., 2010; Kuhn et al., 2010; Andreae et al., 2012). Furthermore, the ratios of excess $N_{CCN}(S)$ to excess c_{CO}, $\Delta N_{CCN}(S) / \Delta c_{CO}$, for the individual S levels range between $6.7 \pm 0.5\,cm^{-3}\,ppb^{-1}$ for the lowest $S = 0.11\,\%$ and values around $18.0 \pm 1.3\,cm^{-3}\,ppb^{-1}$ for higher S (see Table S4 and Fig. S13b). The $\Delta N_{CCN}(S)/\Delta c_{CO}$ ratios converge against $\Delta N_{CN} / \Delta c_{CO}$ even for comparably small S (i.e., $> 0.24\,\%$), which can be explained by the fact that small S already activate a substantial fraction of the pronounced (mostly pyrogenic) accumulation mode (see discussion below). Kuhn et al. (2010) reported $\Delta N_{CCN}(0.6\,\%) / \Delta c_{CO}$ ratios around $26\,cm^{-3}\,ppb^{-1}$ for biomass burning plumes, which is consistent with our observations (i.e., $\Delta N_{CCN}(0.6\,\%) / \Delta c_{CO} = 17.9 \pm 1.3\,cm^{-3}\,ppb^{-1}$; see Table S4). The obtained $\Delta N_{CCN}(S) / \Delta c_{CO}$ ratios were utilized in a dedicated CCN parameterization scheme in our Part 1 study (Pöhlker et al., 2016).

Figure 6e summarizes the corresponding N_{CN} and $N_{CCN}(S)$ size distributions as well as the size dependence of $\kappa(S, D_a)$ for the BB case study. It shows a very strong accumulation mode ($D_{acc} \approx 170\,nm$, $N_{acc} \approx 3400\,cm^{-3}$), "swamping" the Aitken mode ($D_{Ait} \approx 70\,nm$, $N_{Ait} \approx 140\,cm^{-3}$) almost completely, giving the entire distribution a monomodal appearance. For $S < 0.5\,\%$ almost the entire aerosol population is activated as CCN. The averaged $\kappa(S, D_a)$ levels are rather low for both the Aitken and accumulation modes ($\kappa_{Ait} = 0.14 \pm 0.01$ and $\kappa_{acc} = 0.17 \pm 0.02$), in which κ_{acc} is among the lowest values found in the accumulation mode size range throughout the entire study. The low $\kappa(S, D_a)$ levels can be explained by the fact that pyrogenic aerosols predominantly contain organic constituents and rather low levels of inorganic species. The ACSM results during the BB period emphasize the predominant mass fraction of organics (87 %) as well as the minor contribution by nitrate (2 %), ammonium (3 %), and sulfate (4 %) (Table 3). The predicted κ_p of 0.15 ± 0.01 agrees reasonably well with the measurement result, $\kappa(0.11\,\%) = 0.18 \pm 0.01$.

Figure 6f displays the characteristic CCN efficiency spectrum for the BB period, which levels out clearly below unity. The dashed line shows the erf fit forced to go from 0 to 1 (i.e., with the pre-defined variable $a_1 = 1$), which does not match the data points for $S > 0.5\,\%$. This fit has been included here, since the activated fraction must reach 100 % eventually. For comparison, the solid line is an erf fit of the data where the plateau is an open fit parameter. This erf fit matches the data points very well, and the fit parameters as presented in Table 4 reveal the plateau at 93 %. Physically, this indicates the presence of an externally mixed aerosol population with 7 % of the particles being hydrophobic (e.g., a certain fraction of rather fresh soot) and not acting as CCN in the measured S range. The slope of the efficiency spectrum shows a steep increase for $S < 0.4\,\%$. According to these findings,

the ΔS-sensitive range is rather small with $S < 0.4\,\%$. According to Reutter et al. (2009), the BB case study conditions with the large number of available CCN (e.g., N_{CCN} (0.47 %) $> 4000\,\mathrm{cm}^{-3}$) fall into the updraft-limited regime.

It can be expected that the large aerosol load, its optical properties, and its ability to serve as CCN must already influence cloud properties and the stability of the thermodynamic profile of the atmosphere at both local and regional scales (Cecchini et al., 2017b). As mentioned above, the incoming solar radiation was dimmed compared to the days before and after this BB event. Furthermore, the cloud fraction decreased, which might result from stabilizing the atmosphere due to increased absorption of solar radiation in and above the boundary layer, the "semidirect effect" (e.g., Koren et al., 2004; Rosenfeld et al., 2008; Rosário et al., 2013). A detailed investigation of the direct radiative forcing and the modification of cloud properties by aerosol particles in the Amazon rain forest are clearly beyond the scope of this study. Nevertheless, the results shown here may serve as input for dedicated regional climate simulations.

3.7 Case study MPOL on the complex aerosol mixtures during the dry season

The previous BB case study presented the aerosol and CCN properties of a strong and well-defined regional biomass burning plume. However, the dry-season aerosol mixture at ATTO can be rather complex due to the influence of a variety of sources, such as biomass burning, fossil fuel combustion, and industrial emissions from local/regional sources as well as from African long-range transport, in addition to the natural aerosol background (i.e., PBAP, SOA, marine aerosols) (e.g., Freud et al., 2008; Artaxo et al., 2013; Saturno et al., 2017a; C. Pöhlker et al., 2018). Accordingly, the dry-season aerosol mixture is highly variable and no single episode reflects the conditions comprehensively. Therefore, we defined a mixed pollution (MPOL) case study, which is evidently influenced by local/regional biomass burning in South America and the long-range transport of African aerosols. The MPOL case serves as an example of the highly variable aerosol conditions during the Amazonian dry season. The 7-day MPOL period in September 2014 shows an exceptionally low OA / SO_4^{2-} mass ratio (Table 3). Saturno et al. (2017b) recently showed that the high sulfate concentrations can be explained by the long-range transport of volcanogenic aerosols from Africa (i.e., from the Nyiragongo and Nyamuragira volcanoes in eastern Congo) into the Amazon (compare also Fioletov et al., 2016). While the volcanogenic aerosol shows characteristic properties that allow this LRT component to be distinguished from the local/regional BB aerosol, African BB aerosols can be transported similarly; however, an experimental discrimination of African vs. Amazonian BB aerosol is difficult (see Saturno et al., 2017a). Upon arrival of the African plume in the Amazonian atmosphere, the LRT aerosol has mixed with local/regional fires emissions.

Meteorologically, the time frame of the MPOL period was mostly cloud-free (see daily profile in $\mathrm{SW}_{\mathrm{in}}$) and without precipitation (see P_{TRMM} and P_{ATTO}), as well as characterized by rather stable wind conditions (Fig. 9). With respect to the aerosol and CCN parameters, the relevant time series – such as N_{CN}, $M_{\mathrm{BC_e}}$, and $N_{\mathrm{CCN}}(S)$ – show a high variability. Specifically, the $\mathrm{d}N/\mathrm{dlog}D$ contour plot shows an alternating pattern: on one hand, and marked by a grey shading, rather extended periods with comparably low aerosol concentrations (around $1000\,\mathrm{cm}^{-3}$) and high $\kappa(S, D_{\mathrm{a}})$ values (up to 0.35) can be observed. The $\kappa(S, D_{\mathrm{a}})$ levels reaching ~ 0.35 are among the highest in the entire dry season of 2014 (compare Fig. 4). On the other hand, and marked by a light purple shading, these conditions are interrupted by several pulses with strongly enhanced aerosol concentrations (up to $5000\,\mathrm{cm}^{-3}$) as well as substantially lower $\kappa(S, D_{\mathrm{a}})$ values (around 0.1). The changes in $\kappa(S, D_{\mathrm{a}})$ occur with simultaneous changes in the aerosol chemical composition: slight increases of the OA / SO_4^{2-} ratio indicate that the pulses comprise organic-rich aerosol due to the influence of local/regional BB plumes, whereas the lower OA / SO_4^{2-} aerosol is comparatively rich in sulfate due to the volcanogenic origin.

A combination of BTs and satellite data during the MPOL period shows that all BTs follow an easterly direction along the Amazon River (Fig. S14), which is the most frequent scenario during the dry season (see C. Pöhlker et al., 2018). The same study also shows that during this period the shores of the Amazon River can be regarded as the core region of the ATTO site footprint, where BT densities are highest. Accordingly, all aerosol and trace gas sources in these areas are of primary importance for the ATTO region. For instance, this is true for a deforestation hot spot in the area around the cities Oriximina and Òbidos as well as a variety of anthropogenic sources (i.e., industry, power plants, cities, shipping) (compare Fig. S14 and C. Pöhlker et al., 2018). During the MPOL time frame, several (smaller) deforestation fires were observed within the fetch of the corresponding BTs (Fig. S14). These fires, which mostly burnt for less than a day according to satellite observation, are likely responsible for the low-$\kappa(S, D_{\mathrm{a}})$ and high-OA / SO_4^{2-} pulses within the MPOL period. Thus, the pulses can be considered as the advection of nearby biomass burning plumes into the ATTO region. According to the BT data, the smoke experienced a transport and aging time of 12–18 h. Thus, the smoke plumes during MPOL are fresher than during the BB case study, which experienced atmospheric aging for 2–3 days. This difference in aging might be related to differences in the corresponding $\kappa(S, D_{\mathrm{a}})$ values, with fresh smoke during MPOL showing a lower hygroscopicity ($\kappa_{<100\,\mathrm{nm,MPOL}} \approx 0.10$) and the aged smoke showing higher values ($\kappa_{\mathrm{Ait,BB}} \approx 0.14$, $\kappa_{\mathrm{acc,BB}} \approx 0.17$). Note that biomass burning smoke cannot explain the sulfate-rich aerosol during

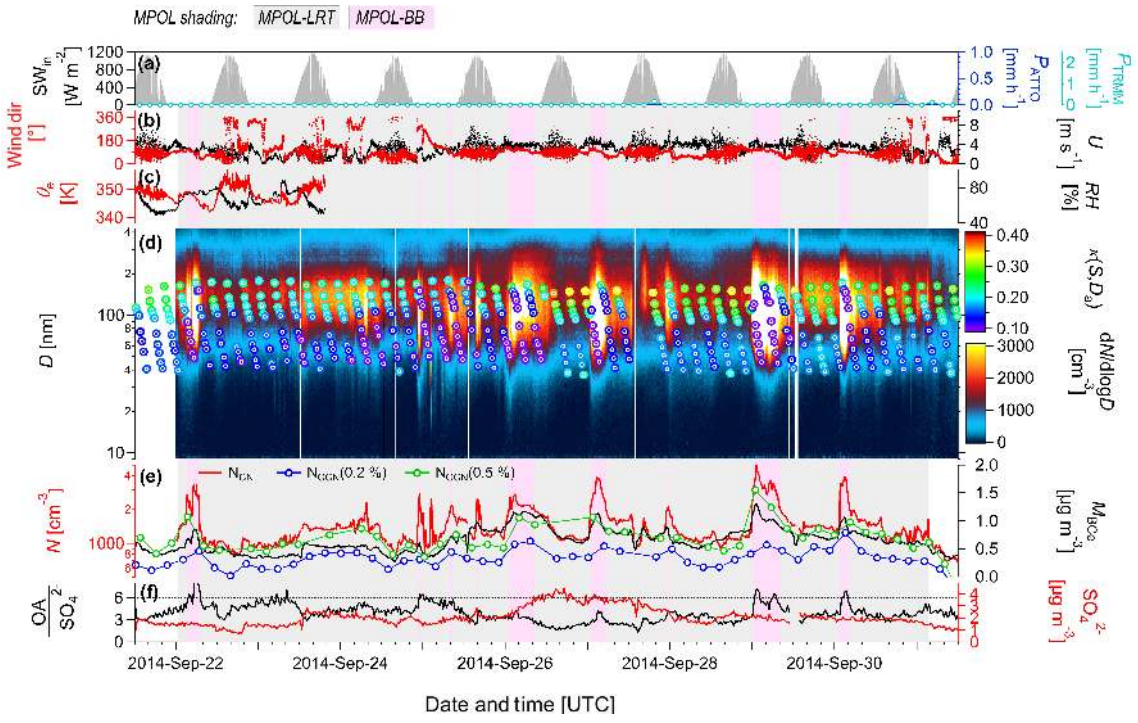

Figure 9. Selected meteorological, aerosol, and CCN time series from ground-based ATTO site measurements for the mixed pollution case study period, MPOL (see Fig. 4). **(a)** Incoming shortwave radiation, SW_{in}; precipitation rates from TRMM satellite mission, P_{TRMM}; and in situ measurements at the ATTO site, P_{ATTO}. **(b)** Wind direction and wind speed, U, at ATTO. **(c)** Equivalent potential temperature, θ_e, and relative humidity, RH, at ATTO. **(d)** Overlay of two data layers showing aerosol number size distribution contour plot, $dN/d\log D$, as well as color-coded markers, representing time series of $\kappa(S, D_a)$ size distributions. **(e)** CCN concentrations, $N_{CCN}(S)$, for two selected S levels; total aerosol number concentration, $N_{CN,10}$; and BC_e mass concentration, M_{BC_e}. **(f)** ACSM-derived sulfate mass concentrations and organic-to-sulfate mass ratio. The vertical shading highlights episodes under the influence of local/regional fires (MPOL-BB) vs. periods that are dominated by long-range transport of African aerosols (MPOL-LRT).

MPOL since BB-related sulfate contents are typically below 6–7 % (e.g., compare BB case in Table 3 as well as Fuzzi et al., 2007; Gunthe et al., 2009; Saturno et al., 2017b).

Figure 6g and h summarize the $N_{CN}(D)$, $N_{CCN}(S,D)$, and $\kappa(S, D_a)$ size distributions during MPOL, separately for the biomass burning pulses (MPOL-BB with $OA / SO_4^{2-} \approx 4$) and LRT influence (MPOL-LRT with lower $OA / SO_4^{2-} \approx 3$). In both cases, the size distributions show a broad monomodal distribution, which did not allow a stable double lognormal mode fitting of Aitken and accumulation modes (see Table 4). The mode is centered at ~ 135 nm for MPOL-LRT, whereas the relatively fresh biomass burning smoke during MPOL-BB shows a modal diameter of ~ 113 nm, in agreement with ~ 100 nm for fresh biomass burning smoke reported by Andreae et al. (2004). The corresponding $N_{CCN}(S,D)$ size distributions show similar shapes, albeit with substantial absolute differences in CCN concentrations. Furthermore, clear differences are also observed for the average $\kappa(S, D_a)$ size distributions: during MPOL-LRT, $\kappa(S, D_a)$ shows a pronounced size dependence. The average κ for sizes < 100 nm is rather size independent ($\kappa_{< 100\,nm} = 0.14 \pm 0.01$). Instead, the average $\kappa_{> 100\,nm}$ increases with D up to 0.26 (on average: $\kappa_{> 100\,nm} = 0.22 \pm 0.03$). According to the shape of the $\kappa(S, D_a)$ size distribution in Fig. 6g, it can be assumed that the aerosol hygroscopicity was even higher for D larger than the covered size range here (i.e., > 170 nm). During the dry season, the highest $\kappa(S, D_a)$ levels for accumulation mode particles were observed during the peak abundance of sulfate at the ATTO site. The hygroscopicity during the MPOL-BB pulses shows generally lower values and weaker size dependence for particles < 150 nm. The average $\kappa_{< 150\,nm} = 0.10 \pm 0.01$ was even smaller than during BB and PR conditions and represents one of the lowest values measured during the entire observation period. For larger particles (e.g., > 150 nm), $\kappa(S, D_a)$ strongly increased towards values comparable to those during MPOL-LRT, showing that both conditions are superimposed (on average: $\kappa_{> 150\,nm} = 0.20 \pm 0.04$).

Figure 6i shows the CCN efficiency spectra for the two MPOL states. The slope of the MPOL-LRT spectrum is significantly steeper than the slope of the MPOL-BB spectrum. The S_1 level of 50 % activation for the sulfate-rich aerosol population (0.16 %) is clearly lower than during the short

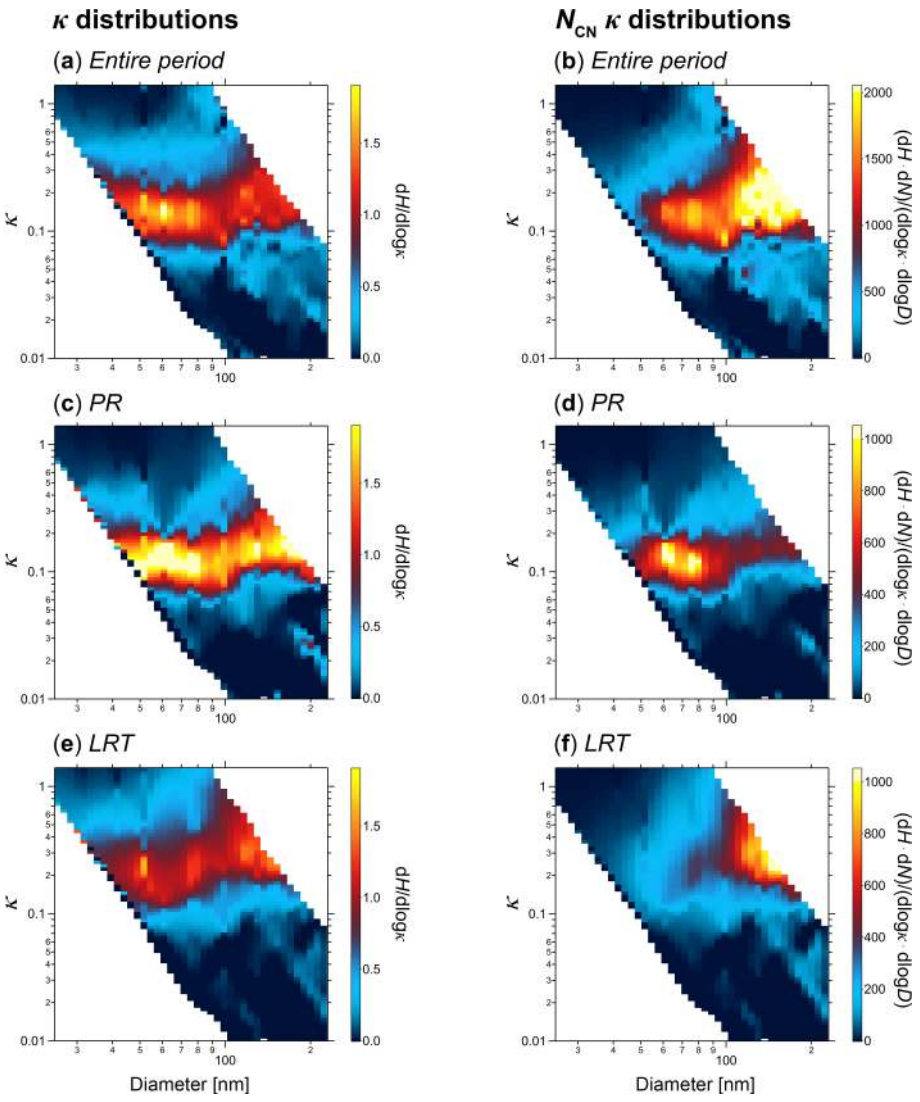

Figure 10.

biomass burning pulses (0.28 %). This rather large difference can be explained by the smaller modal diameter of the MPOL-BB relative to the MPOL-LRT case. Furthermore, κ is significantly decreased for the biomass burning pulses, which are dominated by organic constituents. However, note that the absolute CCN concentration is – while being less hygroscopic – significantly higher for MPOL-BB periods.

In general, the MPOL case study emphasizes the following aspects: (i) the dry-season aerosols that arrive at the ATTO site can be rather complex mixtures of superimposed emissions from different sources with contrasting chemical properties. (ii) The properties of the aerosol and CCN population can change rather suddenly and substantially (see N_{CN} and $N_{CCN}(S)$ changes by a factor of 3–4 within a few hours). Similarly, the aerosol hygroscopicity can vary quite strongly from the lowest value observed in the entire study (~ 0.1) to values around 0.35 and higher, which are among to the largest values observed here during the dry season. These quickly and substantially changing aerosol regimes will presumably also impact the cloud conditions during the dry season. (iii) Finally, the Amazonian aerosol and CCN population can be substantially perturbed by emissions from sources (e.g., volcanoes in eastern Congo) that are remarkably far away from the ATTO site ($\sim 10\,000$ km) (Saturno et al., 2017b). This emphasizes very clearly that intercontinental influences have to be considered carefully in the analysis of the Amazonian atmospheric composition.

3.8 Aerosol particle hygroscopicity distributions and aerosol mixing state

In this section, we investigate the aerosol particle mixing state for the different case study conditions with the help of the aerosol particle hygroscopicity distribution – or κ dis-

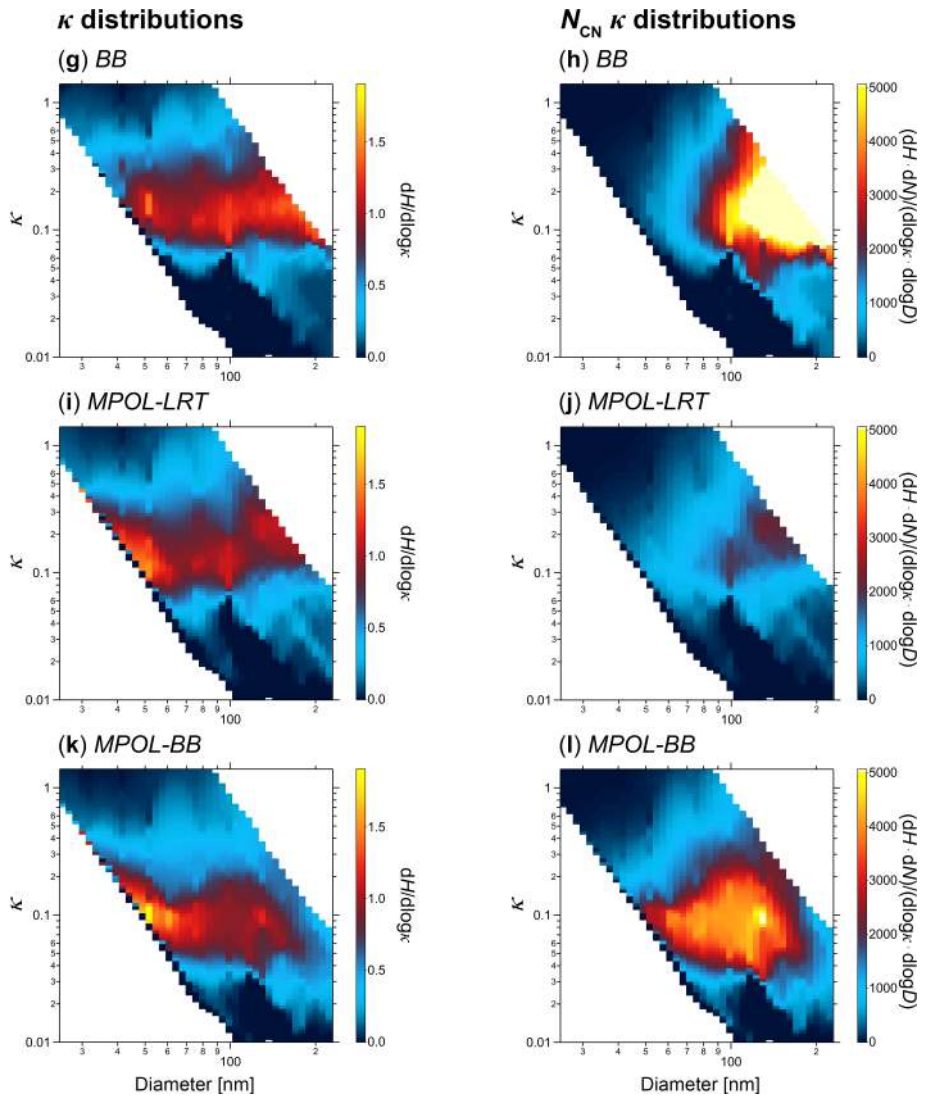

Figure 10. Average probability distribution of particle hygroscopicity, $dH/d\log\kappa$, on the left side and the same quantity weighted by the particle number size distribution, $(dH \cdot dN)/(d\log\kappa \cdot d\log D)$, on the right side, plotted over the effective hygroscopicity parameter, κ, and dry-particle diameter, D, for (**a** and **b**) the entire measurement period as well as (**c** and **d**) PR, (**e** and **f**) LRT, (**g** and **h**) BB, (**i** and **j**) MPOL-LRT, and (**k** and **l**) MPOL-BB conditions. The particle size distributions used for the weighting are shown in Fig. 6.

tribution – concept introduced by Su et al. (2010). This approach visualizes the spread of κ values among particles of a given size. Specifically, in an ideal internal particle mixture, all particles have the same chemical composition and therefore the same hygroscopicity, resulting in a narrow and defined κ distribution. In an external mixture, the particles at a given size can have widely different chemical compositions and hygroscopicities, resulting in a broad κ distribution.

Figure 10 summarizes two versions of κ distributions for the contrasting case study conditions: (i) the "classical" κ distributions according to Su et al. (2010), which emphasize the spread of κ levels for all particle diameters across the measured size range, and (ii) κ distributions weighted with the corresponding average particle size distributions from Fig. 6, which provide a quantitative overview of particle abundance as a function of hygroscopicity and size (N_{CN} κ distribution). The comparison of the κ and N_{CN} κ distributions for the contrasting case study conditions emphasizes similarities and differences between the corresponding aerosol populations, which allows drawing conclusions on the aerosol mixing state and microphysical properties.

The κ distributions for most conditions reflect a bimodal character of the corresponding aerosol distributions with distinctly different properties in the Aitken and accumulation modes as outlined in Fig. 6. Specifically, all distributions show an increasing spread of κ levels towards larger particle diameters, which suggests a higher degree of external particle mixing and therefore a higher diversity of particle

properties (i.e., hygroscopicity) in the accumulation than in the Aitken mode. As an example, the BB and MPOL-BB cases show a κ spread in the accumulation mode range that reaches from values well below 0.1 up to levels of about 1. Remarkably, the PR κ distribution differs from all other cases since it shows overall the smallest spread of κ over the entire size range. This suggests the Aitken and accumulation mode particles under PR conditions are two distinct and chemically rather homogeneous aerosol populations with a comparatively high degree of internal mixing. As an example, the PR Aitken mode particle population covers a defined κ range between ~ 0.1 and ~ 0.15. In contrast, the LRT, BB, and MPOL aerosol populations appear to be more externally mixed.

In addition to the diversity of the hygroscopicity as visible in the κ distributions, the N_{CN} κ distributions further emphasize the quantitative abundance of particles in the hygroscopicity-size space. Accordingly, the N_{CN} κ distributions can be regarded as signature-like representations of the aerosol microphysical state under certain conditions. Note that the N_{CN} κ distributions in Fig. 10 differ substantially from each other. The PR case shows a unique signature. The LRT and MPOL-LRT cases show certain similarities due to the fact that both are characterized by similar aerosol size distributions and comparatively high κ levels. The comparison of the relatively fresh MPOL-BB smoke and the relatively aged BB smoke emphasizes the aging-related increases in particle size and hygroscopicity by means of a characteristic shift of the dominant mode in the N_{CN} κ distributions. In both cases the spread of κ is rather large, indicating a comparatively strong external mixing in the smoke plumes. In essence, the κ distributions and N_{CN} κ distributions are valuable overview representations, which combine characteristic aerosol properties in terms of particle size, particle concentration, κ diversity, and the aerosol mixing state in a fingerprint-like manner. So far, only very few studies (e.g., Mahish et al., 2018) have used the κ distribution or related concepts to characterize ambient aerosol properties. In light of the results in Fig. 10, we suggest that this concept should be used more broadly as it provides valuable insights into the particle mixing state beyond the more established characterizations of aerosol and CCN properties.

3.9 Overview of CCN efficiency spectra and corresponding CCN spectra

CCN efficiency spectra serve as normalized CCN signatures. Their shape is influenced by (i) the shape of the N_{CN} size distribution (i.e., relative strength of Aitken vs. accumulation modes), (ii) the aerosol composition through the $\kappa(S, D_a)$ values and its size dependence, and (iii) the mixing state of the aerosol as represented in the κ and N_{CN} κ distributions. CCN spectra provide quantitative information on the actual CCN concentrations as a function of S. From the CCN efficiency spectra, CCN spectra are readily obtained by multiplication with the corresponding average N_{CN} concentrations (Table 4). This last section combines the CCN efficiency spectra (i.e., the erf fits) and CCN spectra of all analyzed case study conditions from this work with the seasonally averaged spectra from the Part 1 study and literature data. Figure 11 shows an overview of all spectra. The direct comparison emphasizes characteristic similarities and differences as a basis for a concluding discussion on aerosol–cloud interactions. Note in this context that Farmer et al. (2015) presented "cumulative numbers of CCN, normalized to CN", which is conceptually related to the CCN efficiency spectra reported here. Accordingly, a comparison of the spectra reported by Farmer et al. (2015) with Fig. 11 may help to put the characteristics of the Amazonian CCN population into a broader context.

The peak supersaturation and its variability are an essential parameter to understand aerosol–cloud interactions. However, only sparse quantitative information on the actually relevant S range is available. The spectra in Fig. 11 are plotted for a broad S range from 0.001 to 20 %. According to Reutter et al. (2009), this range can be generally subdivided into very low ($S < 0.1$ %), low ($S < 0.2$ %), transitional ($0.2\,\% < S < 0.5\,\%$), and high ($S > 0.5$ %) supersaturation regimes. Furthermore, a recent study by Fan et al. (2018) suggests that under certain conditions even very high supersaturations ($S \gg 1$ %) can be reached in deep convective clouds. One approach to actually quantify ATTO-relevant average peak S at cloud base, $S_{cloud}(D_H,\kappa)$, uses the position of the Hoppel minimum, D_H, as outlined in Hoppel et al. (1986) and Krüger et al. (2014). According to results in our Part 1 companion paper and the present study (see Table 2), ATTO-relevant $S_{cloud}(D_H,\kappa)$ values range from ~ 0.15 to ~ 0.34 %. This $S_{cloud}(D_H,\kappa)$ range is shown as a "S landmark" in Fig. 11 for orientation.

The array of condition-specific CCN efficiency spectra in Fig. 11a shows the diversity of spectral shapes. The PR-specific spectrum represents the lower limiting case with the "slowest" increase in activated fraction upon increasing S (e.g., 50 % activation reached at $S \approx 0.5$ %), whereas the BB and LRT spectra represent the upper limiting cases, reaching high activated fractions at relatively low S (50 % activation at $S \approx 0.15$ % for the BB case and at $S \approx 0.1$ % for the LRT case). The slopes of the spectra, $\mathrm{d}(N_{CCN}(S)/N_{CN,10})/\mathrm{d}S$, indicate how sensitively the activated fractions react towards changes in supersaturation, ΔS. Overall, the highest sensitivities towards ΔS occur between ~ 0.1 and ~ 1.0 %. However, the cases have to be investigated individually to obtain condition-specific "high-sensitivity regimes". For low S (< 0.1 %) – corresponding to the activation of accumulation and coarse-mode particles – the aerosol populations that act as CCN most efficiently are those with strong accumulation modes and high κ levels, such as the sea-salt-rich LRT and sulfate-rich MPOL-LRT populations. In contrast, the PR aerosol acts as CCN least efficiently as it is characterized by a small fraction of accumulation mode particles with rather

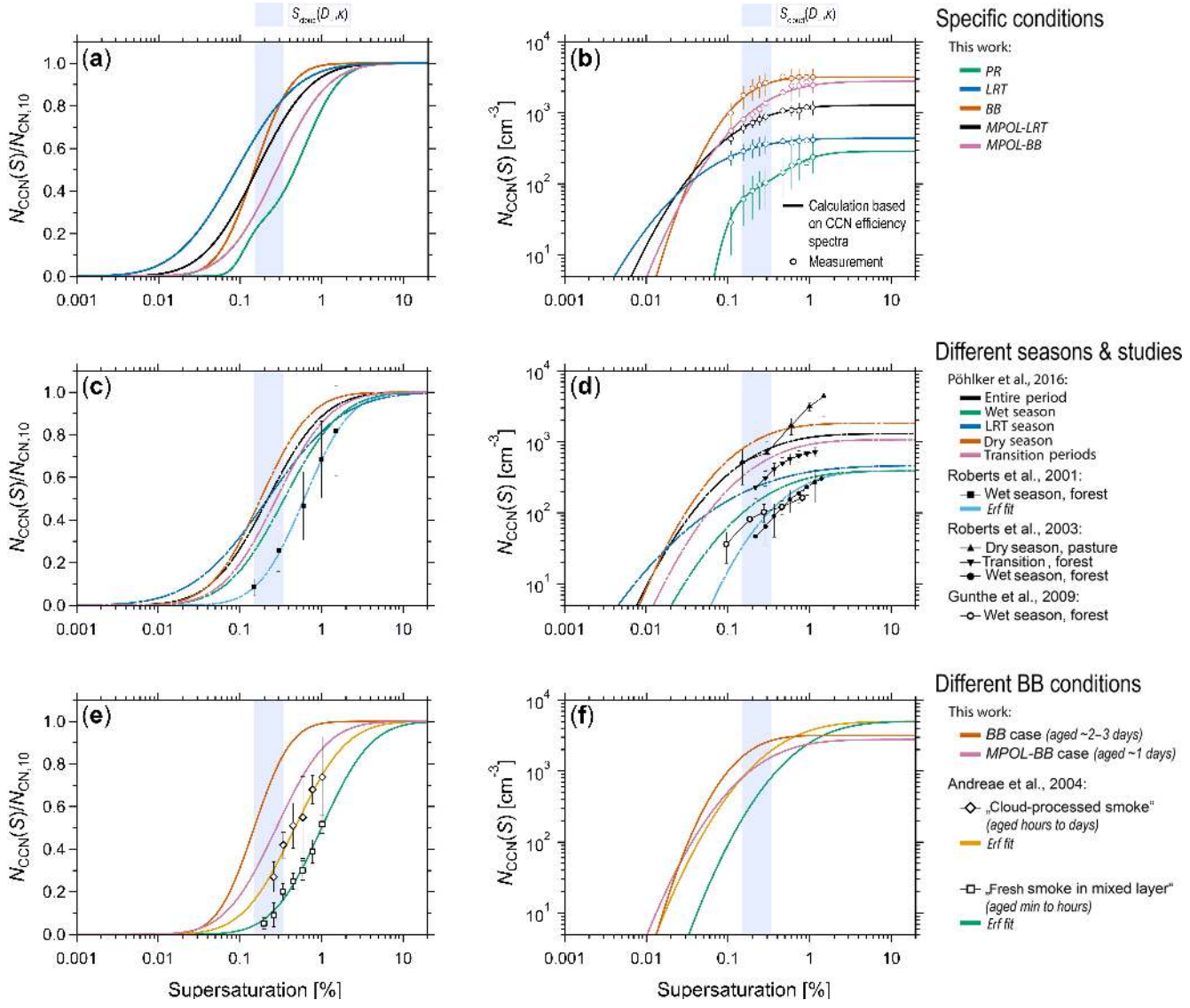

Figure 11. Overview and comparison of normalized CCN efficiency spectra and number-concentration-based CCN spectra for characteristic conditions and seasons. (**a** and **b**) PR, LRT, BB, MPOL-LRT, and MPOL-BB conditions as defined in this paper. (**c** and **d**) Seasonally averaged spectra from the Part 1 companion paper (Pöhlker et al., 2016), CCN efficiency spectrum from Roberts et al. (2001), and CCN spectra from Roberts et al. (2003) and Gunthe et al. (2009). (**e** and **f**) Conditions representing different aging states of biomass burning aerosols based on BB and MPOL-BB conditions from present work and data from a previous study by Andreae et al. (2004). For clarity the erf fit with the pre-defined variable $a_1 = 1$ was used for the BB case (compare Fig. 6f). CCN spectra in **(b)** were obtained from multiplication of CCN efficiency spectra in **(a)** with corresponding average aerosol number concentrations in Table 4. Markers represent measured average CCN concentrations for case study periods. Error bars at markers represent 1 SD. Good agreement of CCN spectra and markers underlines reliability of CCN efficiency spectra in representation of CCN population. Blue vertical shading represents estimated peak supersaturations at cloud base, $S_{\mathrm{cloud}}(D_{\mathrm{H}},\kappa)$, in the ATTO region according to Pöhlker et al. (2016) and the present study. The colors were chosen according to Wong (2011).

low κ. In the transitional S regime with $0.2\,\% < S < 0.5\,\%$ – corresponding to the activation of particles between the Aitken and accumulation modes (i.e., the Hoppel minimum size range) – the individual spectra show their highest divergence and thus the largest differences in CCN efficiency. Note that this range is collocated with the experimentally deduced and ATTO-relevant $S_{\mathrm{cloud}}(D_{\mathrm{H}},\kappa)$ levels. For high S ($> 1\,\%$) – corresponding to the activation of Aitken mode and even smaller particles – full activation is reached and sensitivities towards ΔS decrease.

For comparison, the season-specific CCN efficiency spectra from our Part 1 study are shown in Fig. 11c. Generally,

the shapes of the condition-specific spectra and the season-specific spectra agree well (e.g., relationship between wet and dust seasons and between PR and LRT conditions). However, the characteristic spectral features are more pronounced for the conditions than for the seasons, due to the fact that the case studies on certain conditions incorporate more defined aerosol plumes and/or populations. As an example, the LRT season spectrum includes several LRT events, as well as clean periods in between, whereas the LRT case study spectrum includes only the core period of one defined LRT episode (see Table 1).

Since the size and composition of aerosol particles change dynamically due to atmospheric aging and processing, the CCN efficiency spectra also change accordingly. Figure 11e emphasizes the dynamic character of the shape of the CCN efficiency spectra by means of different aging states of biomass burning plumes. Here we combined four biomass-burning-related CCN efficiency spectra: (i) the BB case study spectrum from this work, which represents smoke after $\sim$2–3 days of atmospheric aging; (ii) the MPOL-BB case study spectrum from this work, which represents smoke after $\sim$1 day of aging; (iii) "cloud-processed smoke" from biomass burning regions in southeast Brazil after hours to days of atmospheric aging according to Andreae et al. (2004); and (iv) "fresh smoke in the mixed layer", also from southeastern Brazil, which was sampled in the fire plumes and thus was aged for minutes to hours only (also from Andreae et al., 2004). The spectral shapes in Fig. 11e clearly differ: the lowest activated fractions were observed for the fresh smoke (50 % activation at $S \approx 1.0$ %; 90 % at $S \approx 4.0$ %), followed by the cloud-processed smoke (50 % activation at $S \approx 0.5$ %; 90 % at $S \approx 2.0$ %), then the MPOL-BB spectrum (50 % activation at $S \approx 0.3$ %; 90 % at $S \approx 1.2$ %), and finally the BB spectrum (50 % activation at $S \approx 0.2$ %; 90 % at $S \approx 0.4$ %) with the highest activated fractions as the upper limiting case. Atmospheric aging tends to increase the particle size through coagulation and condensational growth, and to enhance the particle hygroscopicity through oxidation, aqueous-phase chemistry, and reaction product deposition. Therefore, aging tends to increase the strength of the accumulation at the expense of the Aitken mode and increases κ. Accordingly, it evolves the smoke's CCN efficiency spectra from the "fresh-smoke" conditions – as the initial state – towards the BB case study conditions and presumably even further. This underlines the well-known trend that atmospheric aging increases the suitability of a given particle population to act as CCN (Andreae and Rosenfeld, 2008). Important to note in the context of this study is the following: the CCN efficiency spectra represent signatures of a given aerosol population in a given state of atmospheric aging. Accordingly, the atmospheric aerosol aging and the dynamic evolution of the CCN efficiency spectra's shape have to be kept in mind during discussion and utilization of the spectra in follow-up studies.

From all CCN efficiency spectra the corresponding CCN spectra were calculated as displayed in Fig. 11b, d, and f. Moreover, measured CCN spectra from previous, mostly short-term, campaigns in the Amazon Basin are also shown and agree well with our results (Roberts et al., 2001, 2003; Andreae et al., 2004; Gunthe et al., 2009). Beyond the literature data shown in Fig. 11, good agreement was further observed with Andreae (2009) and Martins et al. (2009). Overall, Fig. 11 may serve as a basis for dedicated cloud microphysical studies on the characteristic differences between the aerosol/CCN populations and their impacts on cloud properties. Particularly, the results obtained here (i.e., N_{CN} concentrations and CCN efficiency spectra) can be used to investigate the sensitivity of clouds under PR conditions, as an approximation for pristine atmospheric conditions in tropical continental regions. The large differences between PR background conditions and perturbed atmospheric states related to anthropogenic (aged) BB smoke in terms of total aerosol concentration as well as the shape of the CCN efficiency spectra are evident. Similarly, the differences between the PR and LRT case studies suggest that the frequent LRT events in the wet season are related to simultaneous changes in the cloud microphysical state, although the changes in total aerosol concentration are comparatively small.

4 Summary and conclusions

In a recent synthesis paper on aerosol–cloud interactions and their highly uncertain representation in global climate models, Seinfeld et al. (2016) proposed that long-term and focused observations in "geographic areas that are critical in climate response" are necessary to obtain a detailed process understanding. Further, studies in "those regions of the present-day atmosphere that approximate preindustrial conditions" will help to "replicate preindustrial aerosol–cloud relationships". In these regions – such as the Amazon Basin – clouds are particularly sensitive to small changes in CCN concentrations (Carslaw et al., 2013). Accordingly, observations are needed here to obtain crucial knowledge on the man-made perturbation of preindustrial aerosol–cloud interactions. This work aims to help tackle this major scientific challenge by presenting detailed long-term aerosol and CCN data for characteristic atmospheric states at the Amazon Tall Tower Observatory (ATTO) in the central Amazon Basin, which is a unique, climate-relevant location with atmospheric conditions oscillation between pristine and anthropogenically strongly perturbed states.

The basis for this work is size-resolved measurements of atmospheric aerosol and cloud condensation nuclei (CCN) concentrations and hygroscopicity at ATTO over a full seasonal cycle (March 2014–February 2015). The results of these observations are presented in two papers: the recently published Part 1 paper provides an in-depth analyses of the multi-month patterns in the Amazonian CCN population as

well as seasonal averages of the key CCN parameters (Pöhlker et al., 2016). Further, Part 1 compares and discusses different CCN parametrization schemes and their suitability to represent the Amazonian CCN cycling in modeling studies. The present Part 2 study completes this picture by analyzing the CCN variability at the original time resolution (4.5 h), which is sufficient to resolve its short-term variability in relation to air mass changes as well as aerosol emission and transformation processes.

A focal point of both studies is the concept of CCN efficiency spectra, which represent a tool to visualize the different behaviors of contrasting aerosol populations in cloud formations and, thus, can be regarded as "CCN signatures". Analytically, the CCN efficiency spectra can be described precisely and in a physically correct way by Gaussian single- or double-error-function (erf) fits. In contrast to other common analytical functions, the erf approach describes the measurement results very accurately and allows CCN properties to be extrapolated to experimentally hardly accessible supersaturations in the low- and high-S regimes.

Here, we zoom into the long-term CCN data in two steps: first, we discuss the aerosol and CCN variability for two 2-month periods that represent contrasting regimes in the aerosol, cloud microphysical, and precipitation seasonality in the central Amazon. The selected periods provide insights into the characteristic atmospheric cycling during the clean wet season and the polluted dry season. Second, we focus on the following four selected case study periods, which represent particularly relevant atmospheric states:

Empirically pristine rain forest (PR) conditions are one of the scientifically most relevant atmospheric states at ATTO. Here, we defined PR conditions by means of black carbon and CO concentrations as pollution tracers. At ATTO, the PR frequency of occurrence peaks between the second half of April and the first half of May. Under PR conditions, aerosol concentrations are very low ($\sim 290\,\mathrm{cm}^{-3}$), and the aerosol population has a characteristic bimodal shape with a dominant Aitken and comparatively weak accumulation mode ($D_{\mathrm{Ait}} \approx 70\,\mathrm{nm}$; $N_{\mathrm{Ait}} \approx 160\,\mathrm{cm}^{-3}$ vs. $D_{\mathrm{acc}} \approx 160\,\mathrm{nm}$; $N_{\mathrm{acc}} \approx 90\,\mathrm{cm}^{-3}$). The aerosol particles are composed of mostly organic matter with minor amounts of inorganic constituents (OA: 0.64, NO_3^-: 0.03, SO_4^{2-}: 0.04, Cl^-: <0.01, BC_e: $<0.01\,\mu\mathrm{g\,m}^{-3}$). The observed low $\kappa(S, D_a)$ levels agree with the particles' composition and show a size dependence ($\kappa_{\mathrm{Ait}} = 0.12 \pm 0.01$ vs. $\kappa_{\mathrm{acc}} = 0.18 \pm 0.01$). The CCN efficiency spectrum shows a characteristic shape since it converges towards full activation rather slowly (50 % activation at ~ 0.5 %, 90 % activation at ~ 1.5 %). Thus, the CCN population is sensitive towards ΔS in both the low- and high-S regime. Accordingly, the CCN population can be regarded as both aerosol-sensitive due to the low total aerosol concentrations and updraft-sensitive according to the CCN efficiency spectrum with its sensitivity to ΔS across a wide S range.

During long-range-transport (LRT) episodes within the wet season, major amounts of aged North African dust, West African biomass burning smoke, and Atlantic marine aerosols are advected on an event basis into the basin (mostly February–April). Total aerosol concentrations ($\sim 440\,\mathrm{cm}^{-3}$) are slightly enhanced relative to the PR state, and the aerosol population has a bimodal shape with a minor Aitken and a stronger accumulation mode ($D_{\mathrm{Ait}} \approx 80\,\mathrm{nm}$, $N_{\mathrm{Ait}} \approx 120\,\mathrm{cm}^{-3}$ vs. $D_{\mathrm{acc}} \approx 180\,\mathrm{nm}$, $N_{\mathrm{acc}} \approx 300\,\mathrm{cm}^{-3}$). Besides the non-refractory fraction of organics and inorganics (OA: $1.81\,\mu\mathrm{g\,m}^{-3}$; NO_3^-: 0.08; NH_4^+: 0.30; SO_4^{2-}: 0.25; Cl^-: 0.04; BC_e: $0.21\,\mu\mathrm{g\,m}^{-3}$), a larger refractory fraction of mineral dust and sea salts can be found in internally mixed particles. The observed $\kappa(S, D_a)$ levels are increased compared to the PR state in agreement with the chemical composition ($\kappa_{\mathrm{Ait}} = 0.18 \pm 0.02$ vs. $\kappa_{\mathrm{acc}} = 0.35 \pm 0.04$). The CCN efficiency spectrum shows a steep increase – and thus high sensitivity to ΔS – at low S and quickly converges against full activation towards high S (50 % activation at ~ 0.09 %, 90 % activation at ~ 0.53 %). Thus, the CCN regime under LRT influence is at the border of the aerosol-limited and transitional regimes.

Biomass burning (BB) is the predominant anthropogenic influence during the Amazonian dry season, which alters the atmospheric composition substantially. During the BB event analyzed here, we found strongly enhanced aerosol concentrations ($\sim 3600\,\mathrm{cm}^{-3}$) and a size distribution dominated by the accumulation mode ($D_{\mathrm{Ait}} \approx 70\,\mathrm{nm}$, $N_{\mathrm{Ait}} \approx 140\,\mathrm{cm}^{-3}$ vs. $D_{\mathrm{acc}} \approx 170\,\mathrm{nm}$, $N_{\mathrm{acc}} \approx 3400\,\mathrm{cm}^{-3}$). The aged smoke particles comprise mostly organic matter (OA: 21.1; NO_3^-: 0.55; NH_4^+: 0.58; SO_4^{2-}: 0.82; Cl^-: 0.03; BC_e: $0.89\,\mu\mathrm{g\,m}^{-3}$). The observed $\kappa(S, D_a)$ levels were comparatively low and weakly size-dependent ($\kappa_{\mathrm{Ait}} = 0.14 \pm 0.01$ vs. $\kappa_{\mathrm{acc}} = 0.17 \pm 0.02$). The corresponding CCN efficiency spectrum shows a rather steep increase at low S and converges against a threshold (~ 93 %) below full activation at high S (50 % activation at $S \approx 0.15$ %). With respect to the large particle concentrations and the large sensitivity of the CCN efficiency spectrum to ΔS in the low-S regime, the BB case falls into the updraft-limited regime.

During the dry season, the central Amazon often experiences mixed aerosol populations from regional, continental, and even transcontinental sources. Here, we analyzed one characteristic example of such mixed-pollution (MPOL) scenarios, in which a mixture of African volcanogenic emissions and nearby Amazonian fires impacted the ATTO site: under conditions with a predominant influence of the African volcanogenic emissions, we found a broad monomodal size distribution ($D_{\mathrm{mode}} \approx 130\,\mathrm{nm}$, $N_{\mathrm{mode}} \approx 1300\,\mathrm{cm}^{-3}$), strongly enhanced sulfate levels (OA: 5.50; SO_4^{2-}: $1.75\,\mu\mathrm{g\,m}^{-3}$), and correspondingly elevated hygroscopicities ($\kappa_{<100\,\mathrm{nm}} = 0.14 \pm 0.01$ vs. $\kappa_{>100\,\mathrm{nm}} = 0.22 \pm 0.03$). Under conditions with predominant influence by the nearby fires, we found high concentrations in a monomodal distribution ($D_{\mathrm{mode}} \approx 110\,\mathrm{nm}$, $N_{\mathrm{mode}} \approx 2800\,\mathrm{cm}^{-3}$), an enhancement of organic matter on top of the sulfate background

(OA: 7.88; SO_4^{2-}: 2.03 µg m^{-3}), and low hygroscopicities ($\kappa_{<150\,nm} = 0.10 \pm 0.01$ vs. $\kappa_{>150\,nm} = 0.20 \pm 0.04$). Accordingly, the interplay of the aged volcanogenic plume and the fresh smoke resulted in large variations of the total aerosol concentration, aerosol composition, and CCN properties. We suppose that the highly variable CCN population results in associated (microphysical) variations in cloud properties.

Hygroscopicity distributions were analyzed for all conditions, providing detailed and characteristic insights into the mixing state of the different types of aerosols. We found that the spread of κ increases with size for all conditions. The κ distributions suggest that the PR aerosol population is rather internally mixed, whereas the BB, LRT, and MPOL aerosols show more external mixing states. In essence, the κ distributions and N_{CN} κ distributions are valuable overview representations, combining characteristic aerosol properties in terms of particle size, particle concentration, κ levels, and aerosol mixing state in a fingerprint-like manner. This representation helps to further elucidate aerosol–cloud interactions, such as the shapes of the CCN efficiency spectra: as general tendencies, more externally mixed aerosols, resulting in broader κ distributions, also broaden the CCN efficiency spectra – analogous to broad N_{CN} distributions. Internally mixed aerosols with more defined κ distributions tend towards steeper segments in the CCN efficiency spectra. Furthermore, externally mixed aerosols with distinctly different κ levels tend to introduce further steps/plateaus into the CCN efficiency spectra, in addition to plateaus caused by multimodal N_{CN} distributions. However, the CCN efficiency spectra for the conditions reported here are primarily shaped by the particle size distributions and average κ levels, whereas the diversity of κ seems to play a minor role. To clarify exactly how the signatures and patterns in κ and N_{CN} κ distributions are related to the signatures and shapes of the CCN efficiency spectra, dedicated future studies at contrasting locations and modeling support are required.

Finally, the CCN efficiency spectra and CCN spectra for all analyzed cases are discussed in an overview, which emphasizes the following observations: (i) the combination of CCN efficiency spectra for all analyzed conditions show a large variability. (ii) Within this range, the estimated peak supersaturations at cloud base, $S_{cloud}(D_H,\kappa)$, are collocated with the intermediate S range, in which the CCN efficiency spectra show their highest variability, thus underlining the impact of changing aerosol populations on cloud properties. (iii) The sensitivity of the CCN populations to changes in S is conditions-specific with highest susceptibilities towards ΔS between $S = 0.1$ and $S = 1\,\%$. (iv) The combination of CCN efficiency spectra for different, particularly contrasting, aerosol populations provides a basis for follow-up studies on the aerosol-related differences in cloud properties in the Amazon region and beyond. (v) Finally, the atmospheric aging of aerosol particles in the atmosphere is reflected in a corresponding evolution of the shape of the CCN efficiency spectra and has to be kept in mind upon their utilization.

Data availability. The data of the key results presented here have been deposited in supplementary data files for use in follow-up studies. They are available in NASA Ames format under https://doi.org/10.17617/3.1k (M. L. Pöhlker et al.: Available data for ATTO CCN Part 2, 2018b): specifically, all PR filters are available as time series of corresponding flags. Moreover, all data from Fig. 6 (i.e., $N_{CN}(D)$, $N_{CCN}(S,D)$, and $\kappa(S, D_a)$ size distributions as well as measured $N_{CCN}(S)/N_{CN,10}$ and $N_{CCN}(S)$ values) are provided. All numbers are given as mean and 1 SD. The time series of the CCN key parameters for the entire measurement period can be found in the Supplement of the Part 1 paper (Pöhlker et al., 2016). For data requests beyond the available data, please refer to the corresponding authors.

Appendix A: List of frequently used symbols.

Symbol	Quantity and unit
a_{mode} (mode = 1, 2)	Prefactor of single- and double-erf fits
D	Mobility equivalent particle diameter, nm
$D_{\mathrm{a}}(S)$	Midpoint activation diameter determined from CCN activation curve, nm
D_{Ait}	Position of Aitken mode maximum, nm
D_{Acc}	Position of accumulation mode maximum, nm
D_{H}	Position of Hoppel minimum, nm
D_{cut}	Cut-off diameter of aerosol impactor, nm
f	Frequency of occurrence
κ	Hygroscopicity parameter
$\kappa(S, D_{\mathrm{a}})$	Hygroscopicity parameter determined from CCN activation curve
κ_{Acc}	Mean hygroscopicity parameter for accumulation mode particles
κ_{Ait}	Mean hygroscopicity parameter for Aitken mode particles
κ_{p}	Predicted hygroscopicity parameter based on ACSM results
MAF (S)	Maximum activated fraction determined by CCN activation curve
$M_{\mathrm{BC_e}}$	Mass concentration of $\mathrm{BC_e}$, $\mu\mathrm{g\,m^{-3}}$
$M^{*}_{\mathrm{BC_e}}$	Threshold $M_{\mathrm{BC_e}}$ level for definition of $\mathrm{PR_{BC}}$ periods, $\mu\mathrm{g\,m^{-3}}$
M_{Org}	ACSM-derived organic mass concentration, $\mu\mathrm{g\,m^{-3}}$
$M_{\mathrm{NO_3}}$	ACSM-derived nitrate mass concentration, $\mu\mathrm{g\,m^{-3}}$
$M_{\mathrm{NH_4}}$	ACSM-derived ammonium mass concentration, $\mu\mathrm{g\,m^{-3}}$
$M_{\mathrm{SO_4}}$	ACSM-derived sulfate mass concentration, $\mu\mathrm{g\,m^{-3}}$
M_{Cl}	ACSM-derived chloride mass concentration, $\mu\mathrm{g\,m^{-3}}$
N	Number of data points
$N_{\mathrm{CCN}}(S)$	CCN number concentration at a certain S, $\mathrm{cm^{-3}}$
$N_{\mathrm{CCN}}(S, D)$	CCN number concentration at a certain S and D, $\mathrm{cm^{-3}}$
$N_{\mathrm{CCN}}(S)/N_{\mathrm{CN,10}}$	CCN efficiency
$N_{\mathrm{CN,Dcut}}$	CN number concentration ($> D_{\mathrm{cut}}$), $\mathrm{cm^{-3}}$
$N_{\mathrm{CN,10}}$	CN number concentration (> 10 nm), $\mathrm{cm^{-3}}$
$N_{\mathrm{CN,Acc}}$	Accumulation mode particle number concentration, $\mathrm{cm^{-3}}$
$N_{\mathrm{CN,Ait}}$	Aitken mode particle number concentration, $\mathrm{cm^{-3}}$
N_{d}	Cloud droplet number concentration, $\mathrm{cm^{-3}}$
N_{db}	Cloud droplet number concentration at cloud base, $\mathrm{cm^{-3}}$
P_{ATTO}	Precipitation rate at ATTO, $\mathrm{mm\,h^{-1}}$
P_{BT}	Cumulative precipitation from HYSPLIT BTs, mm
P_{TRMM}	Precipitation from TRMM satellite mission, $\mathrm{mm\,h^{-1}}$
r_{e}	Cloud droplet effective radius, µm
S	Water vapor supersaturation, %
$S_{\mathrm{cloud}}(D_{\mathrm{H}},\kappa)$	Average peak supersaturation in cloud, %
S_{mode} (mode = 1, 2)	Midpoint activation supersaturation from CCN efficiency spectra, %
$\mathrm{SW_{in}}$	Incoming shortwave radiation (285 to 2800 nm), $\mathrm{W\,m^{-2}}$
θ_{e}	Equivalent potential temperature, K
U	Wind speed, $\mathrm{m\,s^{-1}}$
w_{b}	Updraft velocity at cloud base, $\mathrm{m\,s^{-1}}$
w_{mode} (mode = 1, 2)	Width of CCN efficiency spectra
σ	Width of lognormal fit in Aitken and accumulation mode fitting
σ_{ap}	Aerosol absorption coefficient, $\mathrm{Mm^{-1}}$
x_0	Position of lognormal fit in Aitken and accumulation mode fitting, nm

Appendix B: List of frequently used acronyms.

Acronym	Description
ACSM	Aerosol Chemical Speciation Monitor
ATTO	Amazon Tall Tower Observatory
BB	Biomass burning
BC	Black carbon
BC_e	Equivalent black carbon
BL	Boundary layer
BT	Backward trajectory
BVOC	Biogenic volatile organic compounds
CCN	Cloud condensation nuclei
CCNC	Cloud condensation nuclei counter
CPC	Condensation particle counter
DSD	Droplet size distribution
erf	Gaussian error function
FIRMS	Fire Information for Resource Management System
GDAS	Global Data Assimilation System
GoAmazon2014/5	Green Ocean Amazon 2014/5
HYSPLIT	Hybrid Single Particle Lagrangian Integrated Trajectory Model
IOP	Intensive observation period
$L\,min^{-1}$	Liters per minute
LRT	Long-range transport
ITCZ	Intertropical Convergence Zone
MAAP	Multiangle Absorption Photometer
MAC	Mass absorption coefficient
MODIS	Moderate Resolution Imaging Spectroradiometer
MPOL	Mixed pollution
MPOL-BB	Mixed pollution with dominance of regional BB
MPOL-LRT	Mixed pollution with dominance of LRT
NOAA	National Oceanic and Atmospheric Administration
NASA	National Aeronautics and Space Administration
NPF	New-particle formation
OA	Organic aerosol
PBAP	Primary biological aerosol particles
PR	Empirically pristine rain forest aerosol conditions
PR_{BC}	BC-based PR filter
PR_{CO}	CO-based PR filter
$PR_{BC \cap CO}$	PR filter as intersection of PR_{BC} and PR_{CO} sets
$PR_{BC \cup CO}$	PR filter as union of PR_{BC} and PR_{CO} sets
rBC	Refractory black carbon
RH	Relative humidity
ROI_{ATTO}	Region of interest, covering ATTO region
SE	Standard error
SMPS	Scanning Mobility Particle Sizer
SOA	Secondary organic aerosol
SP2	Single Particle Soot Photometer
SE	Standard error
SD	Standard deviation
UT	Upper troposphere
UTC	Coordinated Universal Time

Supplement. The supplement related to this article is available online at: https://doi.org/10.5194/acp-18-10289-2018-supplement.

Competing interests. The authors declare that they have no conflict of interest.

Special issue statement. This article is part of the special issue "Amazon Tall Tower Observatory (ATTO) Special Issue". It is not affiliated with a conference.

Acknowledgements. This work has been supported by the Max Planck Society (MPG) and the Max Planck Graduate Center with the Johannes Gutenberg University Mainz (MPGC). For the operation of the ATTO site, we acknowledge the support by the German Federal Ministry of Education and Research (BMBF contract 01LB1001A) and the Brazilian Ministério da Ciência, Tecnologia e Inovação (MCTI/FINEP contract 01.11.01248.00) as well as the Amazon State University (UEA), FAPEAM, LBA/INPA, and SDS/CEUC/RDS-Uatumã. This work has been financially supported from the German Research Foundation (DFG grant KA 2280/2); Saint Petersburg State University, Russia (project 11.37.220.2016); the EU FP7 project BACCHUS (project no. 603445); the Sao Paulo Research Foundation (FAPESP grants 13/05014-0 and 13/50510-5); and the Atmospheric System Research (ASR) program, US Department of Energy. Further, the results in Sect. 3 were supported within RSF grant 18-17-00076. This paper contains results of research conducted under the Technical/Scientific Cooperation Agreement between the National Institute for Amazonian Research, the State University of Amazonas, and the Max-Planck-Gesellschaft e.V.; the opinions expressed are entirely the responsibility of the authors and not of the participating institutions. We highly acknowledge the support by the Instituto Nacional de Pesquisas da Amazônia (INPA). The Office of Biological and Environmental Research of the Office of Science is acknowledged for funding, specifically the Atmospheric Radiation Measurement (ARM) Climate Research Facility and the ASR program. We would like to especially thank all the people involved in the technical, logistical, and scientific support of the ATTO project, in particular Susan Trumbore, Carlos Alberto Quesada, Matthias Sörgel, Thomas Disper, Andrew Crozier, Bettina Weber, Nina Ruckteschler, Uwe Schulz, Steffen Schmidt, Antonio Ocimar Manzi, Alcides Camargo Ribeiro, Hermes Braga Xavier, Elton Mendes da Silva, Nagib Alberto de Castro Souza, Adir Vasconcelos Brandão, Amauri Rodriguês Perreira, Antonio Huxley Melo Nascimento, Thiago de Lima Xavier, Josué Ferreira de Souza, Roberta Pereira de Souza, Bruno Takeshi, and Wallace Rabelo Costa. We acknowledge the use of FIRMS data and imagery from the Land, Atmosphere Near real-time Capability for EOS (LANCE) system operated by the NASA/GSFC/Earth Science Data and Information System (ESDIS) with funding provided by NASA/HQ. Satellite product analyses and visualizations used in this paper were produced with the Giovanni online data system, developed and maintained by the NASA GES DISC. We also acknowledge the MODIS and OMI mission scientists and associated NASA personnel for the production of the data used in this research effort. Further, we thank the GoAmazon2014/5 team for the fruitful collaboration and discussions. We appreciate the help of Hauke Paulsen with the fire map analysis. We thank Peter Hoor for stimulating ideas on CO-based PR filtering. Moreover, we thank Qiaoqiao Wang, Oliver Lauer, Jing Ming, Maria Praß, Kathrin Reinmuth-Selzle, and Daniel Rosenfeld for support and stimulating discussions. Finally, we appreciate the constructive comments by two anonymous referees, which were very fruitful for extending and improving important aspects of the paper.

The article processing charges for this open-access publication were covered by the Max Planck Society.

Edited by: Gilberto Fisch
Reviewed by: two anonymous referees

References

Abouchami, W., Näthe, K., Kumar, A., Galer, S. J. G., Jochum, K. P., Williams, E., Horbe, A. M. C., Rosa, J. W. C., Balsam, W., Adams, D., Mezger, K., and Andreae, M. O.: Geochemical and isotopic characterization of the Bodele Depression dust source and implications for transatlantic dust transport to the Amazon Basin, Earth Planet. Sc. Lett., 380, 112–123, https://doi.org/10.1016/j.epsl.2013.08.028, 2013.

Acker, J. G. and Leptoukh, G.: Online analysis enhances use of NASA Earth science data, EOS T. Am. Geophys. Un., 88, 14–17, https://doi.org/10.1029/2007EO020003, 2007.

Andreae, M. O.: Aerosols before pollution, Science, 315, 50–51, https://doi.org/10.1126/science.1136529, 2007.

Andreae, M. O.: Correlation between cloud condensation nuclei concentration and aerosol optical thickness in remote and polluted regions, Atmos. Chem. Phys., 9, 543–556, https://doi.org/10.5194/acp-9-543-2009, 2009.

Andreae, M. O. and Rosenfeld, D.: Aerosol-cloud-precipitation interactions. Part 1. The nature and sources of cloud-active aerosols, Earth-Sci. Rev., 89, 13–41, https://doi.org/10.1016/j.earscirev.2008.03.001, 2008.

Andreae, M. O., Charlson, R. J., Bruynseels, F., Storms, H., Vangrieken, R., and Maenhaut, W.: Internal Mixture of Sea Salt, Silicates, and Excess Sulfate in Marine Aerosols, Science, 232, 1620–1623, https://doi.org/10.1126/science.232.4758.1620, 1986.

Andreae, M. O., Anderson, B. E., Blake, D. R., Bradshaw, J. D., Collins, J. E., Gregory, G. L., Sachse, G. W., and Shipham, M. C.: Influence of plumes from biomass burning on atmospheric chemistry over the equatorial and tropical South-Atlantic during CITE-3, J. Geophys. Res.-Atmos., 99, 12793–12808, https://doi.org/10.1029/94jd00263, 1994.

Andreae, M. O., Rosenfeld, D., Artaxo, P., Costa, A. A., Frank, G. P., Longo, K. M., and Silva-Dias, M. A. F.: Smoking rain clouds over the Amazon, Science, 303, 1337–1342, https://doi.org/10.1126/science.1092779, 2004.

Andreae, M. O., Artaxo, P., Beck, V., Bela, M., Freitas, S., Gerbig, C., Longo, K., Munger, J. W., Wiedemann, K. T., and Wofsy, S. C.: Carbon monoxide and related trace gases and aerosols over the Amazon Basin during the wet and dry seasons, Atmos. Chem. Phys., 12, 6041–6065, https://doi.org/10.5194/acp-12-6041-2012, 2012.

Andreae, M. O., Acevedo, O. C., Araùjo, A., Artaxo, P., Barbosa, C. G. G., Barbosa, H. M. J., Brito, J., Carbone, S., Chi, X., Cintra, B. B. L., da Silva, N. F., Dias, N. L., Dias-Júnior, C. Q., Ditas, F., Ditz, R., Godoi, A. F. L., Godoi, R. H. M., Heimann, M., Hoffmann, T., Kesselmeier, J., Könemann, T., Krüger, M. L., Lavric, J. V., Manzi, A. O., Lopes, A. P., Martins, D. L., Mikhailov, E. F., Moran-Zuloaga, D., Nelson, B. W., Nölscher, A. C., Santos Nogueira, D., Piedade, M. T. F., Pöhlker, C., Pöschl, U., Quesada, C. A., Rizzo, L. V., Ro, C.-U., Ruckteschler, N., Sá, L. D. A., de Oliveira Sá, M., Sales, C. B., dos Santos, R. M. N., Saturno, J., Schöngart, J., Sörgel, M., de Souza, C. M., de Souza, R. A. F., Su, H., Targhetta, N., Tóta, J., Trebs, I., Trumbore, S., van Eijck, A., Walter, D., Wang, Z., Weber, B., Williams, J., Winderlich, J., Wittmann, F., Wolff, S., and Yáñez-Serrano, A. M.: The Amazon Tall Tower Observatory (ATTO): overview of pilot measurements on ecosystem ecology, meteorology, trace gases, and aerosols, Atmos. Chem. Phys., 15, 10723–10776, https://doi.org/10.5194/acp-15-10723-2015, 2015.

Andreae, M. O., Afchine, A., Albrecht, R., Holanda, B. A., Artaxo, P., Barbosa, H. M. J., Borrmann, S., Cecchini, M. A., Costa, A., Dollner, M., Fütterer, D., Järvinen, E., Jurkat, T., Klimach, T., Konemann, T., Knote, C., Krämer, M., Krisna, T., Machado, L. A. T., Mertes, S., Minikin, A., Pöhlker, C., Pöhlker, M. L., Pöschl, U., Rosenfeld, D., Sauer, D., Schlager, H., Schnaiter, M., Schneider, J., Schulz, C., Spanu, A., Sperling, V. B., Voigt, C., Walser, A., Wang, J., Weinzierl, B., Wendisch, M., and Ziereis, H.: Aerosol characteristics and particle production in the upper troposphere over the Amazon Basin, Atmos. Chem. Phys., 18, 921–961, https://doi.org/10.5194/acp-18-921-2018, 2018.

Artaxo, P., Rizzo, L. V., Brito, J. F., Barbosa, H. M. J., Arana, A., Sena, E. T., Cirino, G. G., Bastos, W., Martin, S. T., and Andreae, M. O.: Atmospheric aerosols in Amazonia and land use change: from natural biogenic to biomass burning conditions, Faraday Discuss., 165, 203–235, https://doi.org/10.1039/c3fd00052d, 2013.

Atwood, S. A., Reid, J. S., Kreidenweis, S. M., Blake, D. R., Jonsson, H. H., Lagrosas, N. D., Xian, P., Reid, E. A., Sessions, W. R., and Simpas, J. B.: Size-resolved aerosol and cloud condensation nuclei (CCN) properties in the remote marine South China Sea – Part 1: Observations and source classification, Atmos. Chem. Phys., 17, 1105–1123, https://doi.org/10.5194/acp-17-1105-2017, 2017.

Baars, H., Ansmann, A., Althausen, D., Engelmann, R., Artaxo, P., Pauliquevis, T., and Souza, R.: Further evidence for significant smoke transport from Africa to Amazonia, Geophys. Res. Lett., 38, L20802, https://doi.org/10.1029/2011gl049200, 2011.

Barbosa, P. M., Stroppiana, D., Gregoire, J. M., and Pereira, J. M. C.: An assessment of vegetation fire in Africa (1981–1991): Burned areas, burned biomass, and atmospheric emissions, Global Biogeochem. Cy., 13, 933–950, https://doi.org/10.1029/1999gb900042, 1999.

Bony, S., Stevens, B., Frierson, D. M. W., Jakob, C., Kageyama, M., Pincus, R., Shepherd, T. G., Sherwood, S. C., Siebesma, A. P., Sobel, A. H., Watanabe, M., and Webb, M. J.: Clouds, circulation and climate sensitivity, Nat. Geosci., 8, 261–268, https://doi.org/10.1038/ngeo2398, 2015.

Braga, R. C., Rosenfeld, D., Weigel, R., Jurkat, T., Andreae, M. O., Wendisch, M., Pöhlker, M. L., Klimach, T., Pöschl, U., Pöhlker, C., Voigt, C., Mahnke, C., Borrmann, S., Albrecht, R. I., Molleker, S., Vila, D. A., Machado, L. A. T., and Artaxo, P.: Comparing parameterized versus measured microphysical properties of tropical convective cloud bases during the ACRIDICON-CHUVA campaign, Atmos. Chem. Phys., 17, 7365–7386, https://doi.org/10.5194/acp-17-7365-2017, 2017.

Bristow, C. S., Hudson-Edwards, K. A., and Chappell, A.: Fertilizing the Amazon and equatorial Atlantic with West African dust, Geophys. Res. Lett., 37, L14807, https://doi.org/10.1029/2010gl043486, 2010.

Capes, G., Johnson, B., McFiggans, G., Williams, P. I., Haywood, J., and Coe, H.: Aging of biomass burning aerosols over West Africa: Aircraft measurements of chemical composition, microphysical properties, and emission ratios, J. Geophys. Res.-Atmos., 113, D00C15, https://doi.org/10.1029/2008jd009845, 2008.

Carbone, S., Brito, J. F., Xu, L., Ng, N. L., Rizzo, L., Holanda, B. A., Wolff, S., Saturno, J., Chi, X., Souza, R. A. F., Pöhlker, M. L., Andreae, M. O., Pöhlker, C., Barbosa, H. M. J., and Artaxo, P.: Long-term chemical composition and source apportionment of submicron aerosol particles in the central Amazon basin (ATTO), Atmos. Chem. Phys., in prep., 2017.

Carslaw, K. S., Lee, L. A., Reddington, C. L., Pringle, K. J., Rap, A., Forster, P. M., Mann, G. W., Spracklen, D. V., Woodhouse, M. T., Regayre, L. A., and Pierce, J. R.: Large contribution of natural aerosols to uncertainty in indirect forcing, Nature, 503, 67–71, https://doi.org/10.1038/nature12674, 2013.

Cecchini, M. A., Machado, L. A. T., Wendisch, M., Costa, A., Krämer, M., Andreae, M. O., Afchine, A., Albrecht, R. I., Artaxo, P., Borrmann, S., Fütterer, D., Klimach, T., Mahnke, C., Martin, S. T., Minikin, A., Molleker, S., Pardo, L. H., Pöhlker, C., Pöhlker, M. L., Pöschl, U., Rosenfeld, D., and Weinzierl, B.: Illustration of microphysical processes in Amazonian deep convective clouds in the gamma phase space: introduction and potential applications, Atmos. Chem. Phys., 17, 14727–14746, https://doi.org/10.5194/acp-17-14727-2017, 2017a.

Cecchini, M. A., Machado, L. A. T., Andreae, M. O., Martin, S. T., Albrecht, R. I., Artaxo, P., Barbosa, H. M. J., Borrmann, S., Fütterer, D., Jurkat, T., Mahnke, C., Minikin, A., Molleker, S., Pöhlker, M. L., Pöschl, U., Rosenfeld, D., Voigt, C., Weinzierl, B., and Wendisch, M.: Sensitivities of Amazonian clouds to aerosols and updraft speed, Atmos. Chem. Phys., 17, 10037–10050, https://doi.org/10.5194/acp-17-10037-2017, 2017b.

Chen, Q., Farmer, D. K., Schneider, J., Zorn, S. R., Heald, C. L., Karl, T. G., Guenther, A., Allan, J. D., Robinson, N., Coe, H., Kimmel, J. R., Pauliquevis, T., Borrmann, S., Pöschl, U., Andreae, M. O., Artaxo, P., Jimenez, J. L., and Martin, S. T.: Mass spectral characterization of submicron biogenic organic particles in the Amazon Basin, Geophys. Res. Lett., 36, L20806, https://doi.org/10.1029/2009gl039880, 2009.

Chi, X., Winderlich, J., Mayer, J.-C., Panov, A. V., Heimann, M., Birmili, W., Heintzenberg, J., Cheng, Y., and Andreae, M. O.: Long-term measurements of aerosol and carbon monoxide at the ZOTTO tall tower to characterize polluted and pristine air in the Siberian taiga, Atmos. Chem. Phys., 13, 12271–12298, https://doi.org/10.5194/acp-13-12271-2013, 2013.

Cochrane, M. A.: Fire science for rainforests, Nature, 421, 913–919, https://doi.org/10.1038/nature01437, 2003.

Davidson, E. A., de Araujo, A. C., Artaxo, P., Balch, J. K., Brown, I. F., Bustamante, M. M. C., Coe, M. T., DeFries, R. S., Keller, M.,

Longo, M., Munger, J. W., Schroeder, W., Soares-Filho, B. S., Souza, C. M., Jr., and Wofsy, S. C.: The Amazon basin in transition, Nature, 481, 321–328, https://doi.org/10.1038/nature10717, 2012.

de Carvalho, W. D. and Mustin, K.: The highly threatened and little known Amazonian savannahs, Nature Ecology & Evolution, 1, 0100, https://doi.org/10.1038/s41559-017-0100, 2017.

Draxler, R. R. and Hess, G. D.: An overview of the HYSPLIT_4 modelling system for trajectories, dispersion and deposition, Aust. Meteorol. Mag., 47, 295–308, 1998.

Ekman, A. M. L., Krejci, R., Engstrom, A., Strom, J., de Reus, M., Williams, J., and Andreae, M. O.: Do organics contribute to small particle formation in the Amazonian upper troposphere?, Geophys. Res. Lett., 35, L17810, https://doi.org/10.1029/2008gl034970, 2008.

Engstrom, A., Ekman, A. M. L., Krejci, R., Strom, J., de Reus, M., and Wang, C.: Observational and modelling evidence of tropical deep convective clouds as a source of mid-tropospheric accumulation mode aerosols, Geophys. Res. Lett., 35, L23813, https://doi.org/10.1029/2008gl035817, 2008.

Ervens, B.: Modeling the Processing of Aerosol and Trace Gases in Clouds and Fogs, Chem. Rev., 115, 4157–4198, https://doi.org/10.1021/cr5005887, 2015.

Fan, J., Rosenfeld, D., Zhang, Y., Giangrande, S. E., Li, Z., Machado, L. A. T., Martin, S. T., Yang, Y., Wang, J., Artaxo, P., Barbosa, H. M. J., Braga, R. C., Comstock, J. M., Feng, Z., Gao, W., Gomes, H. B., Mei, F., Pöhlker, C., Pöhlker, M. L., Pöschl, U., and de Souza, R. A. F.: Substantial convection and precipitation enhancements by ultrafine aerosol particles, Science, 359, 411–418, https://doi.org/10.1126/science.aan8461, 2018.

Farmer, D. K., Cappa, C. D., and Kreidenweis, S. M.: Atmospheric Processes and Their Controlling Influence on Cloud Condensation Nuclei Activity, Chem. Rev., 115, 4199–4217, https://doi.org/10.1021/cr5006292, 2015.

Fearnside, P. M.: Brazil's Cuiaba-Santarem (BR-163) Highway: The environmental cost of paving a soybean corridor through the amazon, Environ. Manage., 39, 601–614, https://doi.org/10.1007/s00267-006-0149-2, 2007.

Fiebig, M., Hirdman, D., Lunder, C. R., Ogren, J. A., Solberg, S., Stohl, A., and Thompson, R. L.: Annual cycle of Antarctic baseline aerosol: controlled by photooxidation-limited aerosol formation, Atmos. Chem. Phys., 14, 3083–3093, https://doi.org/10.5194/acp-14-3083-2014, 2014.

Fioletov, V. E., McLinden, C. A., Krotkov, N., Li, C., Joiner, J., Theys, N., Carn, S., and Moran, M. D.: A global catalogue of large SO_2 sources and emissions derived from the Ozone Monitoring Instrument, Atmos. Chem. Phys., 16, 11497–11519, https://doi.org/10.5194/acp-16-11497-2016, 2016.

Freitas, S. R., Longo, K. M., Diasb, M., Diasb, P. L. S., Chatfield, R., Prins, E., Artaxo, P., Grell, G. A., and Recuero, F. S.: Monitoring the transport of biomass burning emissions in South America, Environ. Fluid Mech., 5, 135–167, https://doi.org/10.1007/s10652-005-0243-7, 2005.

Freud, E., Rosenfeld, D., Andreae, M. O., Costa, A. A., and Artaxo, P.: Robust relations between CCN and the vertical evolution of cloud drop size distribution in deep convective clouds, Atmos. Chem. Phys., 8, 1661–1675, https://doi.org/10.5194/acp-8-1661-2008, 2008.

Fuzzi, S., Decesari, S., Facchini, M. C., Cavalli, F., Emblico, L., Mircea, M., Andreae, M. O., Trebs, I., Hoffer, A., Guyon, P., Artaxo, P., Rizzo, L. V., Lara, L. L., Pauliquevis, T., Maenhaut, W., Raes, N., Chi, X., Mayol-Bracero, O. L., Soto-Garcia, L. L., Claeys, M., Kourtchev, I., Rissler, J., Swietlicki, E., Tagliavini, E., Schkolnik, G., Falkovich, A. H., Rudich, Y., Fisch, G., and Gatti, L. V.: Overview of the inorganic and organic composition of size-segregated aerosol in Rondonia, Brazil, from the biomass-burning period to the onset of the wet season, J. Geophys. Res.-Atmos., 112, D01201, https://doi.org/10.1029/2005jd006741, 2007.

Gläser, G., Wernli, H., Kerkweg, A., and Teubler, F.: The transatlantic dust transport from North Africa to the Americas-Its characteristics and source regions, J. Geophys. Res.-Atmos., 120, 11231–11252, https://doi.org/10.1002/2015jd023792, 2015.

Gonçalves, W. A., Machado, L. A. T., and Kirstetter, P.-E.: Influence of biomass aerosol on precipitation over the Central Amazon: an observational study, Atmos. Chem. Phys., 15, 6789–6800, https://doi.org/10.5194/acp-15-6789-2015, 2015.

Gunthe, S. S., King, S. M., Rose, D., Chen, Q., Roldin, P., Farmer, D. K., Jimenez, J. L., Artaxo, P., Andreae, M. O., Martin, S. T., and Pöschl, U.: Cloud condensation nuclei in pristine tropical rainforest air of Amazonia: size-resolved measurements and modeling of atmospheric aerosol composition and CCN activity, Atmos. Chem. Phys., 9, 7551–7575, https://doi.org/10.5194/acp-9-7551-2009, 2009.

Hamilton, D. S., Lee, L. A., Pringle, K. J., Reddington, C. L., Spracklen, D. V., and Carslaw, K. S.: Occurrence of pristine aerosol environments on a polluted planet, P. Natl. Acad. Sci. USA, 111, 18466–18471, https://doi.org/10.1073/pnas.1415440111, 2014.

Hoppel, W. A., Frick, G. M., and Larson, R. E.: Effect of nonprecipitating clouds on the aerosol size distribution in the marine boundary layer, Geophys. Res. Lett., 13, 125–128, https://doi.org/10.1029/GL013i002p00125, 1986.

Huffman, J. A., Sinha, B., Garland, R. M., Snee-Pollmann, A., Gunthe, S. S., Artaxo, P., Martin, S. T., Andreae, M. O., and Pöschl, U.: Size distributions and temporal variations of biological aerosol particles in the Amazon rainforest characterized by microscopy and real-time UV-APS fluorescence techniques during AMAZE-08, Atmos. Chem. Phys., 12, 11997–12019, https://doi.org/10.5194/acp-12-11997-2012, 2012.

Janhäll, S., Andreae, M. O., and Pöschl, U.: Biomass burning aerosol emissions from vegetation fires: particle number and mass emission factors and size distributions, Atmos. Chem. Phys., 10, 1427–1439, https://doi.org/10.5194/acp-10-1427-2010, 2010.

Jimenez, J. L., Canagaratna, M. R., Donahue, N. M., Prevot, A. S. H., Zhang, Q., Kroll, J. H., DeCarlo, P. F., Allan, J. D., Coe, H., Ng, N. L., Aiken, A. C., Docherty, K. S., Ulbrich, I. M., Grieshop, A. P., Robinson, A. L., Duplissy, J., Smith, J. D., Wilson, K. R., Lanz, V. A., Hueglin, C., Sun, Y. L., Tian, J., Laaksonen, A., Raatikainen, T., Rautiainen, J., Vaattovaara, P., Ehn, M., Kulmala, M., Tomlinson, J. M., Collins, D. R., Cubison, M. J., Dunlea, E. J., Huffman, J. A., Onasch, T. B., Alfarra, M. R., Williams, P. I., Bower, K., Kondo, Y., Schneider, J., Drewnick, F., Borrmann, S., Weimer, S., Demerjian, K., Salcedo, D., Cottrell, L., Griffin, R., Takami, A., Miyoshi, T., Hatakeyama, S., Shimono, A., Sun, J. Y., Zhang, Y. M., Dzepina, K., Kimmel,

J. R., Sueper, D., Jayne, J. T., Herndon, S. C., Trimborn, A. M., Williams, L. R., Wood, E. C., Middlebrook, A. M., Kolb, C. E., Baltensperger, U., and Worsnop, D. R.: Evolution of Organic Aerosols in the Atmosphere, Science, 326, 1525–1529, https://doi.org/10.1126/science.1180353, 2009.

Justice, C., Giglio, L., Roy, D., Boschetti, L., Csiszar, I., Davies, D., Korontzi, S., Schroeder, W., O'Neal, K., and Morisette, J.: MODIS-Derived Global Fire Products, in: Land Remote Sensing and Global Environmental Change, edited by: Ramachandran, B., Justice, C. O., and Abrams, M. J., Remote Sensing and Digital Image Processing, Springer New York, 661–679, 2011.

Kandler, K., Lieke, K., Benker, N., Emmel, C., Kuepper, M., Mueller-Ebert, D., Ebert, M., Scheuvens, D., Schladitz, A., Schuetz, L., and Weinbruch, S.: Electron microscopy of particles collected at Praia, Cape Verde, during the Saharan Mineral Dust Experiment: particle chemistry, shape, mixing state and complex refractive index, Tellus B, 63, 475–496, https://doi.org/10.1111/j.1600-0889.2011.00550.x, 2011.

King, M. D., Platnick, S., Menzel, W. P., Ackerman, S. A., and Hubanks, P. A.: Spatial and Temporal Distribution of Clouds Observed by MODIS Onboard the Terra and Aqua Satellites, IEEE T. Geosci. Remote, 51, 3826–3852, https://doi.org/10.1109/tgrs.2012.2227333, 2013.

Koren, I., Kaufman, Y. J., Remer, L. A., and Martins, J. V.: Measurement of the effect of Amazon smoke on inhibition of cloud formation, Science, 303, 1342–1345, https://doi.org/10.1126/science.1089424, 2004.

Krüger, M. L., Mertes, S., Klimach, T., Cheng, Y. F., Su, H., Schneider, J., Andreae, M. O., Pöschl, U., and Rose, D.: Assessment of cloud supersaturation by size-resolved aerosol particle and cloud condensation nuclei (CCN) measurements, Atmos. Meas. Tech., 7, 2615–2629, https://doi.org/10.5194/amt-7-2615-2014, 2014.

Kuhn, U., Ganzeveld, L., Thielmann, A., Dindorf, T., Schebeske, G., Welling, M., Sciare, J., Roberts, G., Meixner, F. X., Kesselmeier, J., Lelieveld, J., Kolle, O., Ciccioli, P., Lloyd, J., Trentmann, J., Artaxo, P., and Andreae, M. O.: Impact of Manaus City on the Amazon Green Ocean atmosphere: ozone production, precursor sensitivity and aerosol load, Atmos. Chem. Phys., 10, 9251–9282, https://doi.org/10.5194/acp-10-9251-2010, 2010.

Kulmala, M., Vehkamaki, H., Petaja, T., Dal Maso, M., Lauri, A., Kerminen, V. M., Birmili, W., and McMurry, P. H.: Formation and growth rates of ultrafine atmospheric particles: a review of observations, J. Aerosol Sci., 35, 143–176, https://doi.org/10.1016/j.jaerosci.2003.10.003, 2004.

Lathem, T. L., Beyersdorf, A. J., Thornhill, K. L., Winstead, E. L., Cubison, M. J., Hecobian, A., Jimenez, J. L., Weber, R. J., Anderson, B. E., and Nenes, A.: Analysis of CCN activity of Arctic aerosol and Canadian biomass burning during summer 2008, Atmos. Chem. Phys., 13, 2735–2756, https://doi.org/10.5194/acp-13-2735-2013, 2013.

Mahish, M., Jefferson, A., and Collins, D.: Influence of Common Assumptions Regarding Aerosol Composition and Mixing State on Predicted CCN Concentration, Atmosphere, 9, 54, https://doi.org/10.3390/atmos9020054, 2018.

Martin, S. T., Andreae, M. O., Althausen, D., Artaxo, P., Baars, H., Borrmann, S., Chen, Q., Farmer, D. K., Guenther, A., Gunthe, S. S., Jimenez, J. L., Karl, T., Longo, K., Manzi, A., Müller, T., Pauliquevis, T., Petters, M. D., Prenni, A. J., Pöschl, U., Rizzo, L. V., Schneider, J., Smith, J. N., Swietlicki, E., Tota, J., Wang, J., Wiedensohler, A., and Zorn, S. R.: An overview of the Amazonian Aerosol Characterization Experiment 2008 (AMAZE-08), Atmos. Chem. Phys., 10, 11415–11438, https://doi.org/10.5194/acp-10-11415-2010, 2010a.

Martin, S. T., Andreae, M. O., Artaxo, P., Baumgardner, D., Chen, Q., Goldstein, A. H., Guenther, A., Heald, C. L., Mayol-Bracero, O. L., McMurry, P. H., Pauliquevis, T., Pöschl, U., Prather, K. A., Roberts, G. C., Saleska, S. R., Dias, M. A. S., Spracklen, D. V., Swietlicki, E., and Trebs, I.: Sources and properties of Amazonian aerosol particles, Rev. Geophys., 48, RG2002, https://doi.org/10.1029/2008rg000280, 2010b.

Martin, S. T., Artaxo, P., Machado, L., Manzi, A. O., Souza, R. A. F., Schumacher, C., Wang, J., Biscaro, T., Brito, J., Calheiros, A., Jardine, K., Medeiros, A., Portela, B., Sá, S. S. d., Adachi, K., Aiken, A. C., Albrecht, R., Alexander, L., Andreae, M. O., Barbosa, H. M. J., Buseck, P., Chand, D., Comstock, J. M., Day, D. A., Dubey, M., Fan, J., Fast, J., Fisch, G., Fortner, E., Giangrande, S., Gilles, M., Goldstein, A. H., Guenther, A., Hubbe, J., Jensen, M., Jimenez, J. L., Keutsch, F. N., Kim, S., Kuang, C., Laskin, A., McKinney, K., Mei, F., Miller, M., Nascimento, R., Pauliquevis, T., Pekour, M., Peres, J., Petäjä, T., Pöhlker, C., Pöschl, U., Rizzo, L., Schmid, B., Shilling, J. E., Dias, M. A. S., Smith, J. N., Tomlinson, J. M., Tóta, J., and Wendisch, M.: The Green Ocean Amazon Experiment (GoAmazon2014/5) Observes Pollution Affecting Gases, Aerosols, Clouds, and Rainfall over the Rain Forest, B. Am. Meteorol. Soc., 0, https://doi.org/10.1175/bams-d-15-00221.1, 2016a.

Martin, S. T., Artaxo, P., Machado, L. A. T., Manzi, A. O., Souza, R. A. F., Schumacher, C., Wang, J., Andreae, M. O., Barbosa, H. M. J., Fan, J., Fisch, G., Goldstein, A. H., Guenther, A., Jimenez, J. L., Pöschl, U., Silva Dias, M. A., Smith, J. N., and Wendisch, M.: Introduction: Observations and Modeling of the Green Ocean Amazon (GoAmazon2014/5), Atmos. Chem. Phys., 16, 4785–4797, https://doi.org/10.5194/acp-16-4785-2016, 2016b.

Martins, J. A., Goncalves, F. L. T., Morales, C. A., Fisch, G. F., Pinheiro, F. G. M., Leal, J. B. V., Jr., Oliveira, C. J., Silva, E. M., Oliveira, J. C. P., Costa, A. A., and Silva Dias, M. A. F.: Cloud condensation nuclei from biomass burning during the Amazonian dry-to-wet transition season, Meteorol. Atmos. Phys., 104, 83–93, https://doi.org/10.1007/s00703-009-0019-6, 2009.

Moran-Zuloaga, D., Ditas, F., Walter, D., Saturno, J., Brito, J., Carbone, S., Chi, X., Hrabe de Angelis, I., Baars, H., Godoi, R. H. M., Heese, B., Holanda, B. A., Lavric, J. V., Martin, S. T., Ming, J., Pöhlker, M., Ruckteschler, N., Su, H., Wang, Y., Wang, Q., Wang, Z., Weber, B., Wolff, S., Artaxo, P., Pöschl, U., Andreae, M. O., and Pöhlker, C.: Long-term study on coarse mode aerosols in the Amazon rain forest with the frequent intrusion of Saharan dust plumes, Atmos. Chem. Phys. Discuss., https://doi.org/10.5194/acp-2017-1043, in review, 2017.

Nepstad, D., McGrath, D., Alencar, A., Barros, A. C., Carvalho, G., Santilli, M., and Diaz, M. D. V.: Environment – Frontier governance in Amazonia, Science, 295, 629–631, https://doi.org/10.1126/science.1067053, 2002.

Nepstad, D. C., Stickler, C. M., Soares, B., and Merry, F.: Interactions among Amazon land use, forests and climate: prospects for a near-term forest tipping point, Philos. T. R. Soc. B, 363, 1737–1746, https://doi.org/10.1098/rstb.2007.0036, 2008.

Ng, N. L., Herndon, S. C., Trimborn, A., Canagaratna, M. R., Croteau, P. L., Onasch, T. B., Sueper, D., Worsnop,

D. R., Zhang, Q., Sun, Y. L., and Jayne, J. T.: An Aerosol Chemical Speciation Monitor (ACSM) for Routine Monitoring of the Composition and Mass Concentrations of Ambient Aerosol, Aerosol Sci. Tech., 45, 780–794, https://doi.org/10.1080/02786826.2011.560211, 2011.

Nölscher, A. C., Yañez-Serrano, A. M., Wolff, S., de Araujo, A. C., Lavric, J. V., Kesselmeier, J., and Williams, J.: Unexpected seasonality in quantity and composition of Amazon rainforest air reactivity, Nat. Commun., 7, 1–12, https://doi.org/10.1038/ncomms10383, 2016.

Olson, D. M., Dinerstein, E., Wikramanayake, E. D., Burgess, N. D., Powell, G. V. N., Underwood, E. C., D'amico, J. A., Itoua, I., Strand, H. E., Morrison, J. C., Loucks, C. J., Allnutt, T. F., Ricketts, T. H., Kura, Y., Lamoreux, J. F., Wettengel, W. W., Hedao, P., and Kassem, K. R.: Terrestrial Ecoregions of the World: A New Map of Life on Earth, Bioscience, 51, 933–938, https://doi.org/10.1641/0006-3568(2001)051[0933:teotwa]2.0.co;2, 2001.

Petzold, A. and Schonlinner, M.: Multi-angle absorption photometry – a new method for the measurement of aerosol light absorption and atmospheric black carbon, J. Aerosol Sci., 35, 421–441, https://doi.org/10.1016/j.jaerosci.2003.09.005, 2004.

Pöhlker, C., Wiedemann, K. T., Sinha, B., Shiraiwa, M., Gunthe, S. S., Smith, M., Su, H., Artaxo, P., Chen, Q., Cheng, Y. F., Elbert, W., Gilles, M. K., Kilcoyne, A. L. D., Moffet, R. C., Weigand, M., Martin, S. T., Pöschl, U., and Andreae, M. O.: Biogenic Potassium Salt Particles as Seeds for Secondary Organic Aerosol in the Amazon, Science, 337, 1075–1078, https://doi.org/10.1126/science.1223264, 2012.

Pöhlker, C., Walter, D., Paulsen, H., Könemann, T., Rodríguez-Caballero, E., Moran-Zuloaga, D., Brito, J., Carbone, S., Degrendele, C., Després, V. R., Ditas, F., Holanda, B. A., Kaiser, J. W., Lammel, G., Lavric, J. V., Ming, J., Pickersgill, D., Pöhlker, M. L., Praß, M., Ruckteschler, N., Saturno, J., Sörgel, M., Wang, Q., Weber, B., Wolff, S., Artaxo, P., Pöschl, U., and Andreae, M. O.: Land cover and its transformation in the backward trajectory footprint region of the Amazon Tall Tower Observatory, Atmos. Chem. Phys. Discuss., https://doi.org/10.5194/acp-2018-323, in review, 2018.

Pöhlker, M. L., Pöhlker, C., Ditas, F., Klimach, T., Hrabe de Angelis, I., Araújo, A., Brito, J., Carbone, S., Cheng, Y., Chi, X., Ditz, R., Gunthe, S. S., Kesselmeier, J., Könemann, T., Lavric, J. V., Martin, S. T., Mikhailov, E., Moran-Zuloaga, D., Rose, D., Saturno, J., Su, H., Thalman, R., Walter, D., Wang, J., Wolff, S., Barbosa, H. M. J., Artaxo, P., Andreae, M. O., and Pöschl, U.: Long-term observations of cloud condensation nuclei in the Amazon rain forest – Part 1: Aerosol size distribution, hygroscopicity, and new model parametrizations for CCN prediction, Atmos. Chem. Phys., 16, 15709–15740, https://doi.org/10.5194/acp-16-15709-2016, 2016.

Pöhlker, M. L., Ditas, F.,Saturno, J., Klimach, T., Hrabě de Angelis, I., Araùjo, A. C., Brito, J., Carbone, S., Cheng, Y.,Chi, X., Ditz, R., Gunthe, S. S., Holanda, B. A., Kandler, K., Kesselmeier, J., Könemann, T., Krüger, O. O., Lavrič, J. V., Martin, S. T., Mikhailov, E., Moran-Zuloaga, D., Rizzo, L. V., Rose, D., Su, H., Thalman, R., Walter, D., Wang, J., Wolff, S., Barbosa, H., Artaxo, P., Andreae, M. O., Pöschl, U., Pöhlker, C: Available data for ATTO CCN Part 2 study, https://doi.org/10.17617/3.1k, 2018.

Pöschl, U., Martin, S. T., Sinha, B., Chen, Q., Gunthe, S. S., Huffman, J. A., Borrmann, S., Farmer, D. K., Garland, R. M., Helas, G., Jimenez, J. L., King, S. M., Manzi, A., Mikhailov, E., Pauliquevis, T., Petters, M. D., Prenni, A. J., Roldin, P., Rose, D., Schneider, J., Su, H., Zorn, S. R., Artaxo, P., and Andreae, M. O.: Rainforest Aerosols as Biogenic Nuclei of Clouds and Precipitation in the Amazon, Science, 329, 1513–1516, https://doi.org/10.1126/science.1191056, 2010.

Reutter, P., Su, H., Trentmann, J., Simmel, M., Rose, D., Gunthe, S. S., Wernli, H., Andreae, M. O., and Pöschl, U.: Aerosol- and updraft-limited regimes of cloud droplet formation: influence of particle number, size and hygroscopicity on the activation of cloud condensation nuclei (CCN), Atmos. Chem. Phys., 9, 7067–7080, https://doi.org/10.5194/acp-9-7067-2009, 2009.

Rissler, J., Swietlicki, E., Zhou, J., Roberts, G., Andreae, M. O., Gatti, L. V., and Artaxo, P.: Physical properties of the submicrometer aerosol over the Amazon rain forest during the wet-to-dry season transition – comparison of modeled and measured CCN concentrations, Atmos. Chem. Phys., 4, 2119–2143, https://doi.org/10.5194/acp-4-2119-2004, 2004.

Rizzolo, J. A., Barbosa, C. G. G., Borillo, G. C., Godoi, A. F. L., Souza, R. A. F., Andreoli, R. V., Manzi, A. O., Sá, M. O., Alves, E. G., Pöhlker, C., Angelis, I. H., Ditas, F., Saturno, J., Moran-Zuloaga, D., Rizzo, L. V., Rosário, N. E., Pauliquevis, T., Santos, R. M. N., Yamamoto, C. I., Andreae, M. O., Artaxo, P., Taylor, P. E., and Godoi, R. H. M.: Soluble iron nutrients in Saharan dust over the central Amazon rainforest, Atmos. Chem. Phys., 17, 2673–2687, https://doi.org/10.5194/acp-17-2673-2017, 2017.

Roberts, G. C., Artaxo, P., Zhou, J. C., Swietlicki, E., and Andreae, M. O.: Sensitivity of CCN spectra on chemical and physical properties of aerosol: A case study from the Amazon Basin, J. Geophys. Res.-Atmos., 107, 8070, https://doi.org/10.1029/2001jd000583, 2002.

Roberts, G. C., Nenes, A., Seinfeld, J. H., and Andreae, M. O.: Impact of biomass burning on cloud properties in the Amazon Basin, J. Geophys. Res.-Atmos., 108, 4062, https://doi.org/10.1029/2001jd000985, 2003.

Roberts, M. C., Andreae, M. O., Zhou, J. C., and Artaxo, P.: Cloud condensation nuclei in the Amazon Basin: "Marine" conditions over a continent?, Geophys. Res. Lett., 28, 2807–2810, 2001.

Rosário, N. E., Longo, K. M., Freitas, S. R., Yamasoe, M. A., and Fonseca, R. M.: Modeling the South American regional smoke plume: aerosol optical depth variability and surface shortwave flux perturbation, Atmos. Chem. Phys., 13, 2923–2938, https://doi.org/10.5194/acp-13-2923-2013, 2013.

Rose, D., Gunthe, S. S., Mikhailov, E., Frank, G. P., Dusek, U., Andreae, M. O., and Pöschl, U.: Calibration and measurement uncertainties of a continuous-flow cloud condensation nuclei counter (DMT-CCNC): CCN activation of ammonium sulfate and sodium chloride aerosol particles in theory and experiment, Atmos. Chem. Phys., 8, 1153–1179, https://doi.org/10.5194/acp-8-1153-2008, 2008.

Rose, D., Gunthe, S. S., Su, H., Garland, R. M., Yang, H., Berghof, M., Cheng, Y. F., Wehner, B., Achtert, P., Nowak, A., Wiedensohler, A., Takegawa, N., Kondo, Y., Hu, M., Zhang, Y., Andreae, M. O., and Pöschl, U.: Cloud condensation nuclei in polluted air and biomass burning smoke near the mega-city Guangzhou, China – Part 2: Size-resolved aerosol chemical composition, diurnal cycles, and externally mixed weakly

CCN-active soot particles, Atmos. Chem. Phys., 11, 2817–2836, https://doi.org/10.5194/acp-11-2817-2011, 2011.

Rosenfeld, D., Lohmann, U., Raga, G. B., O'Dowd, C. D., Kulmala, M., Fuzzi, S., Reissell, A., and Andreae, M. O.: Flood or drought: How do aerosols affect precipitation?, Science, 321, 1309–1313, https://doi.org/10.1126/science.1160606, 2008.

Rosenfeld, D., Andreae, M. O., Asmi, A., Chin, M., de Leeuw, G., Donovan, D. P., Kahn, R., Kinne, S., Kivekas, N., Kulmala, M., Lau, W., Schmidt, K. S., Suni, T., Wagner, T., Wild, M., and Quaas, J.: Global observations of aerosol-cloud-precipitation-climate interactions, Rev. Geophys., 52, 750–808, https://doi.org/10.1002/2013rg000441, 2014.

Rosenfeld, D., Zheng, Y., Hashimshoni, E., Pöhlker, M. L., Jefferson, A., Pöhlker, C., Yu, X., Zhu, Y., Liu, G., Yue, Z., Fischman, B., Li, Z., Giguzin, D., Goren, T., Artaxo, P., Barbosa, H. M. J., Pöschl, U., and Andreae, M. O.: Satellite retrieval of cloud condensation nuclei concentrations by using clouds as CCN chambers, P. Natl. Acad. Sci. USA, 113, 5828–5834, https://doi.org/10.1073/pnas.1514044113, 2016.

Saturno, J., Holanda, B. A., Pöhlker, C., Ditas, F., Wang, Q., Moran-Zuloaga, D., Brito, J., Carbone, S., Cheng, Y., Chi, X., Ditas, J., Hoffmann, T., Hrabe de Angelis, I., Könemann, T., Lavric, J. V., Ma, N., Ming, J., Paulsen, H., Pöhlker, M. L., Rizzo, L. V., Schlag, P., Su, H., Walter, D., Wolff, S., Zhang, Y., Artaxo, P., Pöschl, U., and Andreae, M. O.: Black and brown carbon over central Amazonia: Long-term aerosol measurements at the ATTO site, Atmos. Chem. Phys. Discuss., https://doi.org/10.5194/acp-2017-1097, in review, 2017a.

Saturno, J., Ditas, F., Penning de Vries, M., Holanda, B. A., Pöhlker, M. L., Carbone, S., Walter, D., Bobrowski, N., Brito, J., Chi, X., Gutmann, A., Hrabe de Angelis, I., Machado, L. A. T., Moran-Zuloaga, D., Rüdiger, J., Schneider, J., Schulz, C., Wang, Q., Wendisch, M., Artaxo, P., Wagner, T., Pöschl, U., Andreae, M. O., and Pöhlker, C.: African volcanic emissions influencing atmospheric aerosol particles over the Amazon rain forest, Atmos. Chem. Phys. Discuss., https://doi.org/10.5194/acp-2017-1152, in review, 2017b.

Saturno, J., Pöhlker, C., Massabò, D., Brito, J., Carbone, S., Cheng, Y., Chi, X., Ditas, F., Hrabe de Angelis, I., Morán-Zuloaga, D., Pöhlker, M. L., Rizzo, L. V., Walter, D., Wang, Q., Artaxo, P., Prati, P., and Andreae, M. O.: Comparison of different Aethalometer correction schemes and a reference multi-wavelength absorption technique for ambient aerosol data, Atmos. Meas. Tech., 10, 2837–2850, https://doi.org/10.5194/amt-10-2837-2017, 2017c.

Seinfeld, J. H., Bretherton, C., Carslaw, K. S., Coe, H., DeMott, P. J., Dunlea, E. J., Feingold, G., Ghan, S., Guenther, A. B., Kahn, R., Kraucunas, I., Kreidenweis, S. M., Molina, M. J., Nenes, A., Penner, J. E., Prather, K. A., Ramanathan, V., Ramaswamy, V., Rasch, P. J., Ravishankara, A. R., Rosenfeld, D., Stephens, G., and Wood, R.: Improving our fundamental understanding of the role of aerosol-cloud interactions in the climate system, P. Natl. Acad. Sci. USA, 113, 5781–5790, https://doi.org/10.1073/pnas.1514043113, 2016.

Stevens, B. and Feingold, G.: Untangling aerosol effects on clouds and precipitation in a buffered system, Nature, 461, 607–613, https://doi.org/10.1038/nature08281, 2009.

Su, H., Rose, D., Cheng, Y. F., Gunthe, S. S., Massling, A., Stock, M., Wiedensohler, A., Andreae, M. O., and Pöschl, U.: Hygroscopicity distribution concept for measurement data analysis and modeling of aerosol particle mixing state with regard to hygroscopic growth and CCN activation, Atmos. Chem. Phys., 10, 7489–7503, https://doi.org/10.5194/acp-10-7489-2010, 2010.

Swap, R., Garstang, M., Greco, S., Talbot, R., and Kallberg, P.: Saharan dust in the Amazon Basin, Tellus B, 44, 133–149, https://doi.org/10.1034/j.1600-0889.1992.t01-1-00005.x, 1992.

Talbot, R. W., Andreae, M. O., Berresheim, H., Artaxo, P., Garstang, M., Harriss, R. C., Beecher, K. M., and Li, S. M.: Aerosol chemsitry during the wet season in central Amazonian – The influence of long-range transport, J. Geophys. Res.-Atmos., 95, 16955–16969, https://doi.org/10.1029/JD095iD10p16955, 1990.

Tao, W. K., Chen, J. P., Li, Z. Q., Wang, C., and Zhang, C. D.: Impact of aerosols on convective clouds and precipitation, Rev. Geophys., 50, RG2001, https://doi.org/10.1029/2011rg000369, 2012.

Thalman, R., de Sá, S. S., Palm, B. B., Barbosa, H. M. J., Pöhlker, M. L., Alexander, M. L., Brito, J., Carbone, S., Castillo, P., Day, D. A., Kuang, C., Manzi, A., Ng, N. L., Sedlacek III, A. J., Souza, R., Springston, S., Watson, T., Pöhlker, C., Pöschl, U., Andreae, M. O., Artaxo, P., Jimenez, J. L., Martin, S. T., and Wang, J.: CCN activity and organic hygroscopicity of aerosols downwind of an urban region in central Amazonia: seasonal and diel variations and impact of anthropogenic emissions, Atmos. Chem. Phys., 17, 11779–11801, https://doi.org/10.5194/acp-17-11779-2017, 2017.

Wang, J., Krejci, R., Giangrande, S., Kuang, C., Barbosa, H. M. J., Brito, J., Carbone, S., Chi, X., Comstock, J., Ditas, F., Lavric, J., Manninen, H. E., Mei, F., Moran-Zuloaga, D., Pöhlker, C., Pöhlker, M. L., Saturno, J., Schmid, B., Souza, R. A. F., Springston, S. R., Tomlinson, J. M., Toto, T., Walter, D., Wimmer, D., Smith, J. N., Kulmala, M., Machado, L. A. T., Artaxo, P., Andreae, M. O., Petäjä, T., and Martin, S. T.: Amazon boundary layer aerosol concentration sustained by vertical transport during rainfall, Nature, 539, 416–419, https://doi.org/10.1038/nature19819, 2016.

Wang, X., Zhang, L., and Moran, M. D.: Uncertainty assessment of current size-resolved parameterizations for below-cloud particle scavenging by rain, Atmos. Chem. Phys., 10, 5685–5705, https://doi.org/10.5194/acp-10-5685-2010, 2010.

Weinzierl, B., Ansmann, A., Prospero, J. M., Althausen, D., Benker, N., Chouza, F., Dollner, M., Farrell, D., Fomba, W. K., Freudenthaler, V., Gasteiger, J., Groß, S., Haarig, M., Heinold, B., Kandler, K., Kristensen, T. B., Mayol-Bracero, O. L., Müller, T., Reitebuch, O., Sauer, D., Schäfler, A., Schepanski, K., Spanu, A., Tegen, I., Toledano, C., and Walser, A.: The Saharan Aerosol Long-Range Transport and Aerosol–Cloud-Interaction Experiment: Overview and Selected Highlights, B. Am. Meteorol. Soc., 98, 1427–1451, https://doi.org/10.1175/bams-d-15-00142.1, 2017.

Wendisch, M., Pöschl, U., Andreae, M. O., Machado, L. A. T., Albrecht, R., Schlager, H., Rosenfeld, D., Martin, S. T., Abdelmonem, A., Afchine, A., Araùjo, A. C., Artaxo, P., Aufmhoff, H., Barbosa, H. M. J., Borrmann, S., Braga, R., Buchholz, B., Cecchini, M. A., Costa, A., Curtius, J., Dollner, M., Dorf, M., Dreiling, V., Ebert, V., Ehrlich, A., Ewald, F., Fisch, G., Fix, A., Frank, F., Fütterer, D., Heckl, C., Heidelberg, F., Hüneke, T., Jäkel, E., Järvinen, E., Jurkat, T., Kanter, S., Kästner, U., Kenntner, M., Kesselmeier, J., Klimach, T., Knecht, M., Kohl, R., Kölling, T., Krämer, M., Krüger, M., Krisna, T. C., Lavric, J. V., Longo,

K., Mahnke, C., Manzi, A. O., Mayer, B., Mertes, S., Minikin, A., Molleker, S., Münch, S., Nillius, B., Pfeilsticker, K., Pöhlker, C., Roiger, A., Rose, D., Rosenow, D., Sauer, D., Schnaiter, M., Schneider, J., Schulz, C., Souza, R. A. F. d., Spanu, A., Stock, P., Vila, D., Voigt, C., Walser, A., Walter, D., Weigel, R., Weinzierl, B., Werner, F., Yamasoe, M. A., Ziereis, H., Zinner, T., and Zöger, M.: ACRIDICON–CHUVA Campaign: Studying Tropical Deep Convective Clouds and Precipitation over Amazonia Using the New German Research Aircraft HALO, B. Am. Meteorol. Soc., 97, 1885–1908, https://doi.org/10.1175/bams-d-14-00255.1, 2016.

Winderlich, J., Chen, H., Gerbig, C., Seifert, T., Kolle, O., Lavric, J. V., Kaiser, C., Höfer, A., and Heimann, M.: Continuous low-maintenance $CO_2/CH_4/H_2O$ measurements at the Zotino Tall Tower Observatory (ZOTTO) in Central Siberia, Atmos. Meas. Tech., 3, 1113–1128, https://doi.org/10.5194/amt-3-1113-2010, 2010.

Wong, B.: POINTS OF VIEW Color blindness, Nat. Methods, 8, 441–441, https://doi.org/10.1038/nmeth.1618, 2011.

Yáñez-Serrano, A. M., Nölscher, A. C., Williams, J., Wolff, S., Alves, E., Martins, G. A., Bourtsoukidis, E., Brito, J., Jardine, K., Artaxo, P., and Kesselmeier, J.: Diel and seasonal changes of biogenic volatile organic compounds within and above an Amazonian rainforest, Atmos. Chem. Phys., 15, 3359–3378, https://doi.org/10.5194/acp-15-3359-2015, 2015.

Yáñez-Serrano, A. M., Nölscher, A. C., Bourtsoukidis, E., Gomes Alves, E., Ganzeveld, L., Bonn, B., Wolff, S., Sa, M., Yamasoe, M., Williams, J., Andreae, M. O., and Kesselmeier, J.: Monoterpene chemical speciation in a tropical rainforest:variation with season, height, and time of dayat the Amazon Tall Tower Observatory (ATTO), Atmos. Chem. Phys., 18, 3403–3418, https://doi.org/10.5194/acp-18-3403-2018, 2018.

Yu, H. B., Chin, M., Yuan, T. L., Bian, H. S., Remer, L. A., Prospero, J. M., Omar, A., Winker, D., Yang, Y. K., Zhang, Y., Zhang, Z. B., and Zhao, C.: The fertilizing role of African dust in the Amazon rainforest: A first multiyear assessment based on data from Cloud-Aerosol Lidar and Infrared Pathfinder Satellite Observations, Geophys. Res. Lett., 42, 1984–1991, https://doi.org/10.1002/2015gl063040, 2015.

Zhou, J., Swietlicki, E., Hansson, H. C., and Artaxo, P.: Submicrometer aerosol particle size distribution and hygroscopic growth measured in the Amazon rain forest during the wet season, J. Geophys. Res., 107, 8055, https://doi.org/10.1029/2000jd000203, 2002.

Zikova, N. and Zdimal, V.: Precipitation scavenging of aerosol particles at a rural site in the Czech Republic, Tellus B, 68, 27343, https://doi.org/10.3402/tellusb.v68.27343, 2016.